UNIVERSITY OF CALIFORNIA,
IRVINE

Chemical and Physical Determinants of Bacterial Biofilm Development

DISSERTATION

submitted in partial satisfaction of the requirements
for the degree of

DOCTOR OF PHILOSOPHY

in Materials Science and Engineering

by

Arunima Bhattacharjee

Dissertation Committee:
Professor Allon I. Hochbaum, Chair
Professor Manuela Raffatellu
Professor Aaron Esser-Kahn

2017

DEDICATION

To

my family

TABLE OF CONTENTS

LIST OF FIGURES

LIST OF TABLES

ACKNOWLEDGMENTS

I would like to express my sincere gratitude to the committee chair and my advisor Professor Allon Hochbaum for his patience, continuous help and support, and his immense knowledge. Professor Hochbaum's enthusiasm and dedication towards science was a great motivation for me and his encouragement and belief in my abilities lead me on to paths I never imagined I could tread. I had the opportunity to learn from his unique problem solving skills, which applies beyond academia. I am truly grateful to be Professor Hochbaum's student.

I would like to extend my acknowledgement to rest of my committee members Dr. Manuela Raffatellu and Dr. Aaron Esser-Kahn for their insightful comments, guidance and support.

I would like to express my deepest appreciation forDr. Tyler Nusca who taught me natural product extraction and purification techniques and offered helpful suggestions and advice regarding many of my projects.

I would like to acknowledge Professor Enrico Gratton for so many beneficial suggestions during the collaboration in the FLIM project. I had the opportunity to collaborate with Dr. Martina Sassone-Corsi and Dr. Rupsa Datta in two very interesting projects which I enjoyed and am thankful for.

I would like to thank my labmates and close friends, Nicole Ing and Torin Dupper for general discussion on my work and being so supportive all throughout.

Last but not the least I would like to thankthe Schlumberger Foundation for supporting my research and professional development activities for the final two years of my doctoral work.

ABSTRACT OF THE DISSERTATION

Chemical and physical determinants of bacterial biofilm development

By

Arunima Bhattacharjee

Doctor of Philosophy in Materials Science and Engineering

University of California, Irvine, 2017

Professor Allon I. Hochbaum, Chair

Bacterial biofilms cause persistent and deadly infections in medical settings, which are resistant to conventional antibiotic doses. Medical biofilms are often multi-species communities of bacteria which are maintained through chemical signaling and metabolite exchange. An improved understanding of the interactions between bacteria governing community behavior will facilitate the discovery of drug targets for biofilm prevention and eradication. In this thesis, I describe coculture interactions between different species of bacteria and a method to track metabolic states of bacteria in different environments.

One example of such coculture interactions is illustrated in the competition for iron in an *in vitro* infection model. *Salmonellaenterica* serovar Typhimurium (STm) causes acute infections in the gut, but STm infections are abolished in coculture with a probiotic bacterium, *Escherichia coli* Nissle (EcN). EcN outcompetes STm in the gut via a class of bactericidal compounds, called microcins, which are conjugated to iron scavenging siderophore molecules. *In vitro* biofilm models show that STm uses EcN siderophores to acquire iron, and that siderophore conjugation is an anti-cheating strategy employed by EcN to outcompete STm for nutrients.

In another example of novel coculture interactions, *E. coli* and *Pseudomonas aeruginosa* have competitive interactions governing biofilm establishment and dispersal. The *E. coli* biofilm dispersal is triggered by *P. aeruginosa* quorum sensing (QS) compounds. However, *E. coli* biofilms grown on periodic microcturctures, resembling the stomach micro-villi, are shown to modulate this pathway by metabolite accumulation in engineered microenvironments. Substrate structures induce changes in *E. coli* biofilm morphology, which in turn increase the concentration of indole, a constitutively produced metabolite within the biofilm. Moreover, the monoculture biofilms grown on microstructured substrates are significantly more susceptible to antibiotics than monocultures on flat substrates. FLIM is a label free, non-invasive technique and has immense potential for use as a means to probe interactions in microbial communities. Fluorescence lifetime imaging microscopy (FLIM), demonstrates that this increased antibiotic susceptibility is due to changes in cellular metabolism induced by an altered microenvironment. The research in this thesis demonstrates more long term and permanent strategies for biofilm infections and will provide guidelines and inspiration for improved diagnostics, and treatments for biofilm infections.

Chapter 1

An introduction to bacterial biofilms

1.1. Overview

Biofilms are surfaced attached communities of bacteria, enclosed within a 3D matrix made of extracellular polymeric substances (EPS), which consists of polysaccharide, extracellular DNA and proteins. Biofilm communities can be beneficial or harmful. In medical settings, biofilm infections are deadly and difficult to treat with antibiotics [1]. The EPS maintains the biofilm morphology and structure, while creating a barrier to the penetration of bactericidal compounds [2,3]. The EPS also retains enzymes, nutrients and lysed cells from the surrounding environment, allowing them to be used as energy sources and reservoirs of extracellular DNA and proteins. The biofilm matrix immobilizes the bacterial cells, keeping them in close proximity and thus allowing for different interactions between cells within the biofilm [4]. The biofilm environment is greatly heterogeneous, with gradients of oxygen, nutrients, metabolites produced by indwelling bacteria. These gradients create a great deal of heterogeneity in cellular physiology and metabolism of bacteria living within the biofilm [5,6].

Infections of wounds and indwelling medical devices are caused by well studied, biofilm-forming bacteria such as *Pseudomonas aeruginosa*, *Staphylococcus aureus*, and pathogenic *Escherichia coli* [1]. Enteric pathogens, like *Salmonella enterica*, are known to cause acute and deadly infections in the gut [7]. During infection, bacterial communities are maintained through interaction between constituent species of bacteria. Biofilms serve as effective model systems for infection-causing communities, and a deeper understanding of interactions between bacteria in biofilms can identify novel therapeutic targets for acute and persistent bacterial infections. This

thesis describes my efforts to characterize and manipulate interactions between species of bacteria within two model coculture biofilms: *Escherichia coli* Nissle 1917 (EcN) and *Salmonella enterica* serovar Typhimurium (STm), and *E. coli* K12 and *Pseudomonas aeruginosa*. In these communities, mechanisms of biofilm inhibition and dispersal, resulting from interspecies competition and cell-cell signaling pathways, are described in Chapters 2 & 3. In Chapter 4, I describe how microstructured growth substrates are used to understand the role of growth environment heterogenaeity on mechanisms of chemical communication between species. These substrates also induce greater antibiotic susceptibility to the biofilms grown on them, due to fundamental changes in metabolic states of the constituent bacteria. A new method for mapping the metabolic states of bacteria in planktonic and biofilm environments *in situ* using a non-invasive and label free imaging spectroscopy technique is described in Chapter 5. Treatment of biofilm related infections is currently a difficult and complicated challenge for researchers and clinicians, and this thesis describes analytical and physical methods that provide insight into relevant processes bacteria use naturally to regulate community development and dispersal. Moreover, this work provides fundamental insights into different ways in which bacterial communities are shaped by cell-cell communication.

1.2. Stages of biofilm development

Biofilm formation involves the transition of bacteria from a free-living, planktonic state to a sessile one, and is regulated by various genetic and chemical signaling pathways (Figure 1). The processes involved in biofilm development are commonly studied using static and microfluidic *in vitro* systems [8–12]. These *in vitro* models have proven to be powerful for elucidating the genes and signaling compounds involved in the stages of biofilm development,

from initial attachment, to surface aggregation, mature structure development, and in some instances biofilm dispersal processes. During initial stages of biofilm development, planktonic bacteria reversibly attach to a surface in a process dependent on attractive and repulsive chemical forces between the bacterial outer membrane components or appendages and the surface. Following initial attachment, bacteria aggregate to from microcolonies on surfaces, driven by cell-cell signaling and surface motility processes. As the aggregates grow, fluid channels for the transport of nutrients and water are formed, and the cells start producing EPS and developing large three-dimensional structures. Each step of biofilm development corresponds to similarly profound physiological and metabolic changes in the constituent bacterial population.

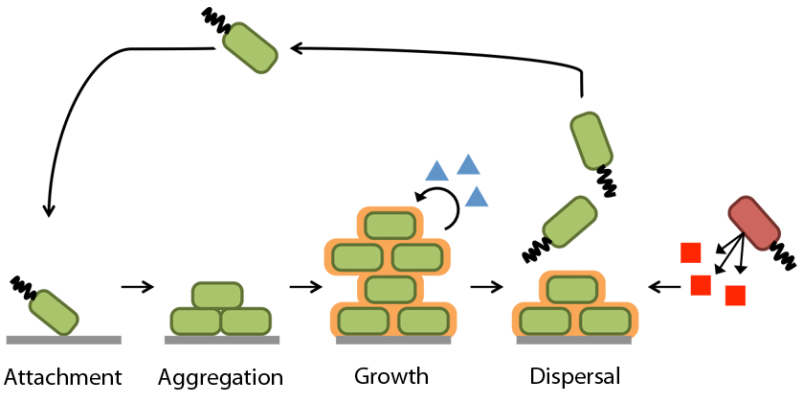

Fig 1. Stages of biofilm development. Biofilms develop through the attachment, aggregation, and subsequent growth of bacterial cells encapsulated in an extracellular polymeric matrix at interfaces. Small and macromolecular compounds triggering biofilm dispersal can be synthesized endogenously (blue triangles) or by other species (red squares) as part of naturally occurring compounds produced by bacteria.

Such variation in physiology and metabolism can be attributed to differences in the local growth environment around each cell, which leads to heterogeneous gene regulation throughout the communities [13,14]. Gradients of nutrients, oxygen, metabolites, antimicrobial and signaling compounds within the biofilm create spatially distinct phenotypic differentiation and affect

biofilm structure and function [15–18]. After the biofilm reaches structural maturity, dispersal becomes an option for the bacteria living within the biofilm. Besides passive dispersal of biofilms, resulting from mechanical shear or abrasion, some biofilm-forming bacteria have evolved genetically regulated pathways that trigger the release of some or all cells from a surface to resume a planktonic lifestyle [19–21]. Biofilm dispersal can be the result of several cues, such as alterations in nutrient availability, oxygen fluctuations, an increase of toxic products, or other environmental stressors [22,23]. For example, an increase in extracellular iron induces biofilm dispersal in uropathogenic *E. coli* [24], whereas *P. aeruginosa* biofilms disperse in response to increased amounts of various carbon and nitrogen sources [25]. Compounds produced by neighboring species can act as dispersal triggers for cells within the biofilm. The stages of biofilm development and dispersal are regulated by signaling compounds and metabolites produced by different species of bacteria living in the community and such compounds are instrumental in mediating interspecies relationship within the biofilm.

1.3. Quorum sensing

Many cooperative behaviors among bacteria, including biofilm formation, are coordinated by the production of signaling compounds specifically targeting the differential regulation of certain genetic pathways. Quorum sensing (QS) is a density dependent trait in aggregated bacteria, where a 'quorum' refers to the minimum number of bacteria within an aggregate that is required to trigger gene expression of specific pathways involved in community behavior. Cells are not physically aware of the density of bacteria in the environment, but, using QS, they can sense surrounding cell density via specific receptors [26,27]. These receptors often signaling molecules or metabolites produced by nearby cells, and this information informs genetically regulated

decision making processes about continuing to populate a certain niche or to move on to a more favorable environment [28,29]. The principle of signal mediated gene expression is common in both Gram-positive and Gram-negative bacteria. In Gram-negative bacteria, acyl homoserine lactones (AHLs) are a common class of signaling molecule. AHLs contain terminal homoserine lactone rings, or closely related derivatives, and a variable length acyl chain of 4–16 carbons, which in most cases are even numbered (C4, C6, C8, etc.) [30–32]. The earliest evidence of QS mediated by small signaling molecules is found in the bacterium *Vibrio fisheri* which produces chemiluminescence in a density dependent manner. This process is regulated by *lux* operon, which produces and responds to AHLs, and homologous QS systems are found in other Gram-negative bacteria [33,34]. In many bacteria, QS regulatory networks are complex and hierarchical. For example, QS in *P. aeruginosa* is composed of two AHL systems controlled by *lasR/lasI* and *rhlR/rhlI* (receptor/AHL biosynthesis genes, respectively), and a quinolone signaling pathway encoded by the *pqs* operon [35–37].

In Gram-positive bacteria, examples of QS compounds include small peptides, 5 to 17 amino acids long. These small peptides bind transmembrane receptors after being actively secreted from the cell. The binding of the small peptides to different receptors results in the regulation of specific pathways in the bacteria [38,39]. Across Gram-negative and –positive species, QS is influenced by different factors such as the microenvironment surrounding the cells, the distance between different bacteria, gradients of metabolites, oxygen and nutrients. By mediating the different signaling processes, these environmental factors also influence the structure and organization of the cells within a biofilm

1.4. Structure and self-organization within bacterial communities.

Biofilm dwelling bacteria influence each other's evolutionary fitness by producing different enzymes, metabolites, signaling compounds, structural polymers, and adhesins for surface attachment. Many of these compounds are shared with neighboring cells and become "public goods", available for even non-producing members of the community to use. Sharing of public goods leads to distinct types of ecological interactions between microbes, such as cooperation, exploitation, or competition. The type and degree of such interactions, in turn, affect the spatial arrangement of bacteria living within the biofilm. Spatial self-organization of bacteria in communities has been shown to play an important role in building community structure and diversity [40,41].

The spatial segregation of cell phenotypes or species within the community becomes significant when it comes to perceiving signaling molecules or metabolites, like AHLs. The distance over which cell-cell communication, and thus behavioral coordination, occurs, known as the calling distance, is up to 100 μm or more – two orders of magnitude greater than the size of the cell [28,42]. Conversely, the spatial arrangement of different species within a biofilm can also determine the types of interactions present between the cells living within the community. There are three main types of spatial organization occur in co-cultures. The first is the formation of segregated, single-species aggregates, where each species forms distinct microcolonies by the side of the other. Coculture biofilms of *Burkholderia spp*. and *Pseudomonas spp.* exhibit such self-organized structures [43,44]. The second is the co-aggregation, where cells of both species are mixed with one another throughout the biofilm, and the third is a layered form of spatial organization [28,42,45]. The first and the second types of organizations exist when a cooperative interaction exists between species. The third, layered type of spatial structure can occur when a

competitive or a cooperative relationship exists between multiple species. Each of these interaction types decides the final structure of the community (Fig. 2).

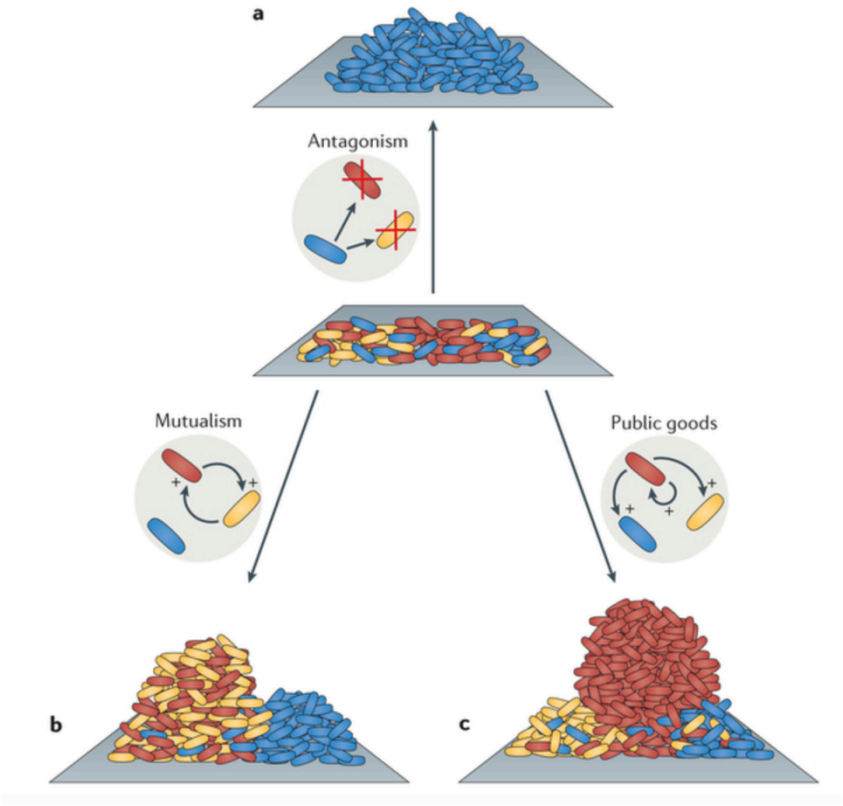

Fig. 2. The influence of social phenotype on the spatial self-organization of biofilm communities [40]. An initially well mixed community can change morphology to (a) the elimination of susceptible cells in case of an antagonistic relationship, (b) the mixing of two mutualistic (red & yellow) lineages and exclusion of the third, non-interacting genotype (blue),, or (c) the layering of mono- and mixed cultures due to the exploitation ("cheating") by two genotypes (blue & yellow) of a public good produced by a third genotype (red).

Several such examples of spatially structured communities exist in nature and, where the precise nature and extent of interactions between cells are well characterized, their heterogeneity of structure and function show that the micro-environment surrounding each cell is significant in determining the stability and function of the community. Based on these ecological principles, synthetic microbial communities with biotechnological applications have been constructed using physical and spatial structures [40,45]. In the case of medically relevant microbes, understanding the

role of signaling compounds and metabolite based interactions on self-organization within a biofilm is crucial to manipulating community function. The ability to engineer microbial interactions through specific signaling or metabolite exchange represents an effective means of manipulating consortia for medical and other technological applications [46]. Such techniques can be used to identify novel and more permanent solutions for biofilm infections.

1.5. Adverse health effects of bacterial biofilms

The presence of bacterial communities in infections has been known for a long time, but the role of biofilms in particular was proposed only in the 1980s [47]. The formation of biofilms by clinically relevant microorganisms is the root cause of several chronic and recurrent infections, and 80% of all microbial infections are estimated to be associated with bacterial biofilms [8,47]. These tend to be chronic infections, which can evade the patient's immune system and persist for years, greatly compromising the patient's quality of life [47].

Biofilm infections can be broadly divided into two types: infections on indwelling medical devices and infections in host tissues. Biofilms formed on the surfaces of indwelling medical devices such as central venous catheters, mechanical heart valves, urinary catheters, joint prostheses, peritoneal dialysis catheters, cardiac pacemakers, cerebrospinal fluid shunts, endotracheal tubes, contact lenses, intrauterine devices and dental unit waterlines, cause persistent inflammation, sepsis, and urinary tract infections [1]. In these cases, pathogens may originate from the epithelial microbiota of patients, healthcare personnel or other sources in the environment [1], to infect the interface between the patient tissue and the medical devices. Through this initial colonization, bacteria gain access to human organs or tissues. Biofilm-associated infections are often chronic, opportunistic infections, such as recurrent urinary tract infection,

chronic wounds, dental caries and periodontitis. These infections are generally also comprised of multiple bacterial species.

Commonly associated bacteria with biofilm infections include *P. aeruginosa, S. aureus* and *E. coli* [1]. Biofilms of these microorganisms cause acute infections in the human host. For example, *P. aeruginosa* is an opportunistic pathogen of immuno-compromised hosts and can cause native acute and chronic lung infections that result in significant morbidity and mortality, especially in cystic fibrosis patients. Some of the pathogens and the type of biofilm-associated infections they cause are listed in the Table 1. These infections are typically tolerant of conventional doses of antibiotics, and antibiotic resistance spreads rapidly in biofilms, causing persistent and deadly infections. One aim of the work described in this dissertation is the identification of new therapeutic targets to reduce the treatment complications posed by biofilm infections.

Table 1. Biofilm associated infectious bacteria

Bacterial species	Type of biofilm infection	Reference
Escherichia coli	Acute and recurrent urinary tract infection, catheter-associated urinary tract infection, biliary tract infection	[48,49]
Pseudomonas aeruginosa	Cystic fibrosis lung infection, chronic wound infection, catheter-associated urinary tract infection, chronic rhinosinusitis, chronic otitis media, contact lens-related keratitis	[49,50]
Staphylococcus aureus	Chronic osteomyelitis, chronic rhinosinusitis, endocarditis, chronic otitis media, orthopaedic implants	[49]
Staphylococcus epidermidis	Central venous catheter, orthopaedic implants, chronic osteomyelitis	[49]
Salmonella enterica serovar Typhimurium	Gasteroenteritis, acute ulcerative colitis	[51]

1.6. Mechanisms of biofilm resistance to antibiotic treatment

One of the characteristic features of bacteria within biofilms is their substantially higher resistance and tolerance to antibiotics relative to their free-living counterparts. The concentration of antibiotics required for effectively killing biofilm associated bacteria, is almost 10- to 1000-fold greater than the effective bactericidal concentration for planktonic bacteria [52], complicating treatment of biofilm infections. Bacteria in biofilms acquire antibiotic resistance by several mechanisms, including the reduced diffusion rates of compounds within the biofilm matrix, altered gene expression, and diminished or dormant metabolic activity [28,29]. In addition, the biofilm content of certain cell phenotypes and EPS matrix protects the cells from dehydration and other environmental stressors [53]. Several of the major contributing mechanisms to enhanced antibiotic resistance in biofilms are discussed below.

1.6.1. Delayed diffusion of compounds within the biofilm

The biofilm matrix can act as a barrier to diffusive penetration of antimicrobial compounds. In some cases, EPS components bind and sequester antibiotic compounds, or they can react chemically with antibiotics to degrade them [4], thus decreasing their concentration. For example, the electrostatic association of cationic aminoglycosides to the anionic polysaccharides of the *P. aeruginosa* biofilm matrix impedes the diffusion of these otherwise effective antibiotics [54]. The biofilm matrix can delay the diffusion of antibiotics and offers short-term protection against bactericidal compounds.

1.6.2. Persister cells

Biofilms contain a population of small cells that adopt a slow- or non-growing lifestyle and are highly tolerant to extracellular stresses. So-called persisters exhibit distinct cell physiology and metabolic activity compared to other biofilm-associated phenotypes. The persister state is a reversible cell phenotype during favorable growth conditions, but they remain dormant under stressful conditions. Persisters cells represent a small subpopulation in the entire colony of bacteria, but they enable the survival of the bacterial species after experiencing harsh conditions, like exposure to antibiotics or dessication. Many antibiotics are far less effective against slow- or non-growing cells compared with fast-growing ones because these antibiotics target growth-specific factors. As a result, the slow growth rates of biofilm cells will render them less susceptible to antibiotics [55]. For example, ß-lactam antibiotics are only effective against rapidly growing and diving cells, whereas fluoroquinones are required for effective treatment of slow growing phenotypes. Persisters survive antibiotic exposure, creating a reservoir of cells that continue to infect the host when the administration of of antibiotics ceases. Consequently, a more nuanced understanding of the effects of antibiotics on bacterial cell metabolism is important for treating biofilm infections.

1.7. Current therapeutic approaches for biofilm infections.

The development of novel strategies for biofilm inhibition and treatment is an active area of research. Anti-adhesive surfaces with altered physical and chemical topographical structure or biofilm matrix degrading enzymes are some of the potential prevention and treatment strategies. QS signal blockers that interferes with different biofilm developments processes have been invented, however as stated above bacteria develop resistance to QS blockers as they do against several antimicrobial agents [56]. Novel cell lysing agents and introduction of dispersal cues are

some of the other biofilm prevention strategies that are being researched. Due to emergence of antibiotic resistance towards most bactericidal drugs, bacteria viruses or bacteriophages are being considered as alternative treatment for biofilm infections, especially for biofilm inhibition or disruption [57,58]. Phages possess many advantages over antibiotics and chemical agents. Phage isolation is fast and simple and production is relatively inexpensive, and no adverse side effects of this treatment has been observed so far [57–59].

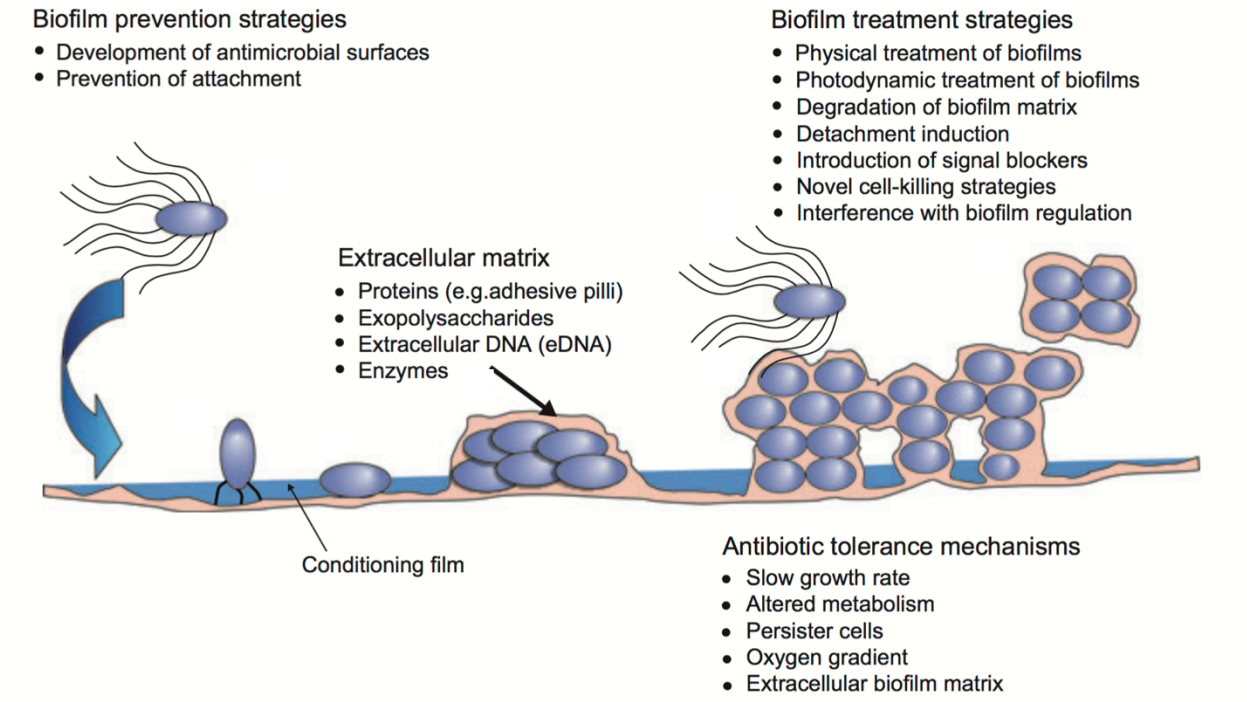

Fig 3. Schematic showing different anti-biofilm strategies targeting at each stage of biofilm development [47].

The figure 3 outlines some of the approaches to biofilm therapeutics that are being developed. Most of the treatment and prevention strategies, such as anti-biofilm surfaces achieved through surface functionalization or leaching of antibiotic compounds, exhibit transient

effects due to their decomposition, cleavage by bacteria derived proteases, over coating with biosurfactants or non-specific biomolecule adsorption or compound depletion in case of leaching strategies [60]. Few biofilm dispersal strategies have been reported in the past [61] and more sustainable solutions to biofilm growth is required.

Due to the central role of QS signaling in biofilm formation, the development of chemical inhibitors of QS signal transduction is a promising target for new therapies. QS inhibitors are compounds that mimic part of the bacteria-derived QS molecule and competitively binds the receptor, down-regulating associated genetic pathways [62]. Several such QS inhibitors targeting QS pathways in different microorganisms have been developed, but bacteria develop resistance to QS inhibitors just like they do to antibiotics [56]. The lack of effective biofilm prevention and treatment strategies encouraged more research about the compounds produced by bacteria living in multispecies biofilms, intra and interspecies interactions in biofilm communities and how these factors influence biofilm structure and function.

1.8. Characterization and analysis of biofilms

As discussed above, biofilm structure and morphology is influenced by the signaling and metabolite interaction that occurs between different species living within a biofilm. As such characterizing these compounds as well as the resulting structure of the community is of great interest. A good understanding of these processes that mediate coculture dynamics will generate insights for developing anti biofilm therapies against infectious biofilms.

Biofilm morphology and spatial localization is often characterized using confocal microscopy. Confocal laser scanning microscopy (CLSM) is a method of choice to study surface attached communities and this technique can be used to acquire time resolved three-dimensional

data of the biofilm structure. Since its first application CLSM has been widely used to understand biofilm architecture, species content and organization within the community. Taking advantage of multi-channel imaging coculture biofilms can be imaged after being labelled with specific markers. Coupled with other characterization techniques this gives us information regarding community structure and properties [16,63–66]. Several image analysis softwares like imageJ, COMSTAT, Volocity and Imaris can extract information regarding total biovolume, surface roughness, thickness [67,68].

Despite the substantial amount of information obtained from CLSM imaging, signaling molecules and metabolites cannot be identified using confocal microscopy and this information is vital in understanding interaction of multiple species mediated by signaling compounds. Imaging mass spectroscopy (IMS) allows the two-dimensional visualization of distribution different metabolites, signaling compounds, and proteins, and this technique is becoming very popular in biofilm research. IMS allows us to obtain a molecular snapshot of the specimen and this can be superimposed into fluorescence or optical images providing spatial distribution of different metabolites at a given time of growth [69–72]. Other mass spectroscopy techniques that are used to purify and analyze compounds in biofilms are liquid chromatography mass spectroscopy (LCMS) and matrix assisted laser desorption ionization (MALDI) [73–76]. Each of these techniques gives information regarding composition of different compounds within a biofilm, however they require substantial amount of purification of the samples prior to analysis. Besides most of these techniques are invasive and cannot get single cell resolution data from live samples.

Novel characterization methods with better resolution and ability to extract data *in situ* are required to understand different processes that govern formation and dispersal of bacterial biofilms. Bactericidal compounds often choose targets that affects the metabolism of cells within

a biofilm. Different metabolites and signaling compounds produced by bacteria also has significant impact on cellular metabolism Understanding the metabolism of bacteria in a sessile state will also provide means to develop anti-biofilm strategies. Current techniques to understand metabolic changes in biofilms are invasive which can skew the results. Less invasive techniques are warranted to study clinical and laboratory grown bacterial biofilms.

Biofilm infections are resistant to conventional bactericidal treatment and antibiotics and require the development of innovative combination therapies for successful eradication and prevention. This work provides a potential for identifying of candidate targets for developing new anti-biofilm therapeutics by demonstrating a better understanding of dispersal and inhibition processes in bacterial biofilms in two different coculture biofilm systems. The following description of my doctoral research shows that *in vitro* biofilm models can be used to study interaction between gut bacteria and provides insight into a dispersal signaling pathway in *E. coli*. Here, I also demonstrate a non-invasive and label-free method for understanding metabolic states of bacteria which is an important goal, to be able to investigate antibiotic resistance mechanisms in biofilm communities.

Chapter 2.

Bacterial microcins mediate iron competition in coculture biofilms

2.1. Introduction

Competition for resources represents a common interaction that can determine biofilm development. In the case of bacterial infections, effective competition can allow commensal or probiotic bacterial populations to inhibit pathogen colonization or eliminate existing infection. Iron is one such nutrient that sustains microbial life and the requirement for iron drives competition between several gut microorganisms. Bacteria require iron for essential processes like respiration, DNA replication, transcription, biofilm formation [77,78]. As a result, bacteria have evolved strategies to recruit and compete for scarce iron from their surrounding environment. Such scarcity occurs during infections, when the host releases iron-scavenging proteins, including transferrin, Lipocalin-2, and ferritin, to limit pathogen growth (fig. 4) [77,79,80]. Microbes respond to iron starvation by releasing small molecules, including siderophores such as enterobactin and salmochelin, which have greater iron binding affinities than several host-secreted proteins (fig. 4) [78,79,81]. Competition for iron between bacterial species in the mammalian gut is critical to determining whether pathogens can establish an infection. For example, the probiotic *Escherichia coli Nissle* 1917 (EcN) strain uses multiple iron uptake pathways to inhibit and abolish established *Salmonella enterica* serovar Typhimurium (STm) infections in murine models [51,82,83]. A better understanding of such evolved strategies used by probiotic bacteria to combat pathogen gut colonization promises to identify new targets for

species-specific antimicrobials and provide insight into population dynamics of the gut microbiota.

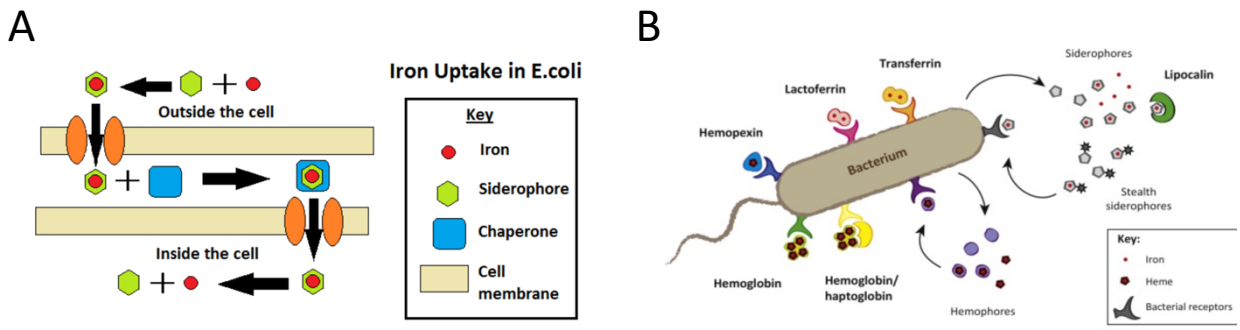

Fig 4. Iron uptake mechanisms in bacteria. A) schematic showing iron uptake by siderophores in *E. coli*. B) Schematic showing different mechanisms in a bacterial cell to sequester iron from host proteins [81].

Once secreted by producing cells, siderophores are public goods that can be used cooperatively by other producers, or they can be exploited by non-producing cells [84–87]. Bacteria have evolved anti-cheating strategies to curb siderophore use by non-producers, such as the development of chemically distinct siderophores [85] and the production of siderophore-conjugated antimicrobial peptides, called microcins. Microcins are small peptides (< 10 kDa) produced in many Enterobacteriaceae, and some are post-translationally conjugated to siderophores [88–90] as a strategy to dominate polymicrobial iron competition in the gut [91–94]. EcN produces two microcins, H47 and M, as part of an iron competition strategy against enteric pathogens [95]. STm is one such pathogen that causes acute gastroenteritis [96–98], and EcN production of microcin M was recently shown to inhibit intestinal colonization of enteropathogens and pathobionts like STm [51]. Microcin production confers a critical competitive advantage to EcN, and they are thought to act by post-translational conjugation to the siderophore salmochelin [99].

Like the process of intestinal colonization and infection *in vivo*, bacterial biofilm formation is dependent on iron recruitment from the environment [100,101], and iron competition plays a critical role in the development and maintenance of polymicrobial biofilms. For instance, biofilm-associated bacteria, use siderophores produced by their counterparts for cross-feeding in mutualistic communities [100,102]. On the other hand, the use of siderophores by cheaters, biofilm constituents that provide no mutual benefit in return, can threaten the fitness of a community by making it more susceptible to bactericidal compounds [100]. Few studies have explored competition mediated by siderophores within multispecies biofilms [103,104], and microcin based anti-cheating strategies in biofilms have not been previously investigated.

In this work, we develop a set of *in vitro* biofilm models for EcN and STm cocultures to provide insights into siderophore and microcins based iron competition and population dynamics. Both EcN and STm produce enterobactin and salmochelin siderophores, which are candidates for cross-feeding or piracy within these coculture biofilms. Moreover, EcN microcins are thought to be conjugated to salmochelin and confer a competitive advantage over enteric pathogens, including STm [99]. EcN wild-type, but not the mutant unable to produce microcins, outcompetes STm in co-inoculated static biofilm models. Moreover, this phenotype was only observed under iron limiting conditions. These biofilm models recapitulate results from murine models indicating that microcin production is key to EcN domination of cocultures with STm, supporting the hypothesis that they inhibit biofilm colonization when STm exploits microcin-conjugated EcN salmochelin [99]. In an instance of siderophore piracy, an EcN *entC* mutant, which lacks the ability to synthesize enterobactin, still out-competes STm in biofilms, possibly via the

utilization of STm siderophores. In static cultures of EcN wild-type supernatant, the growth of STm is unaffected by the presence or absence of microcins. Instead, STm biofilm growth is inhibited only when grown in a microfluidic device, in which the concentration of EcN supernatant components, including microcins, are constant. These results suggest that EcN domination of STm cocultures is independent of contact dependent inhibition mechanisms, but that the constant proximal production of microcin-conjugated siderophores is likely required. Similar growth inhibition of adherent-invasive *E. coli* (AIEC) was observed, indicating that microcin dependent growth inhibition may be a general strategy for EcN abolishment of enteric pathogen infections.

2.2. Materials and methods

2.2.1. Bacterial strains

Strains of the probiotic *Escherichia coli* Nissle 1917 (EcN; Mutaflor, DSM 6601), adherent invasive *E. coli* (AIEC), and the pathogen *Salmonella enterica* serovar Typhimurium (STm, [IR715]) utilized in this study are listed in Table A.1. EcN was kindly provided by Ardeypharm Gmb, Herdecke, Germany. The AIEC strain is a human isolate from a patient with Crohn's disease (isolate NRG857c O83:H1) and was kindly provided by Dr. Alfredo Torres. IR715 is a fully virulent, nalidixic acid-resistant derivative of STm wild-type isolate ATCC 14028. Plasmids used in this study are listed in Table A.2**.** Plasmids expressing GFP (pGFPuv) or mCherry (pFPV-mCherry) were used to distinguish bacterial strains during competition in biofilm growth. The pFPV-mCherry was a gift from Dr. Olivia Steele-Mortimer (Addgene plasmid # 20956).

2.2.2. Generation of bacterial mutants

All the mutants in this chapter were constructed by Dr. Matina Sassone-Corsi. Mutants in EcN were constructed as described previously [99] using the lambda red recombinase system and are listed in Table A.1. In brief, primers (Table A.3**)** homologous to sequences flanking the 5′ and 3′ ends of the target regions were designed (H1 and H2 primers, respectively) and were used to replace the selected genes with kanamycin- (derived from pKD4) (Table A.3**)**. To confirm integration of the resistance cassette and deletion of the target, mutant strains and wild-type controls were each assayed using three PCR amplifications (5′ end, 3′ end, deleted target). Primers (Table A.3**)** that flank the target sequence were used in conjunction with a common test primer (K1, K2) to test for both new-junction fragments.

2.2.3. Static biofilm growth conditions

All bacterial strains were revived from frozen stocks by streaking on LB agar plates. A single colony was inoculated into 2 ml Lysogeny Broth (LB) media (Fisher scientific) and growth shaking at 37 ºC for 6 h. Bacteria from these shaking cultures were diluted in 10 g/l Bacto tryptone media (BD) to an OD of 0.02. 18 X 18 mm glass cover slips in 6 well plates were inoculated with 2 ml of the diluted cultures in TB for static growth biofilm imaging. The plates were left to grow on the bench top for 24 h, unless otherwise noted, at 22 ºC. To grow biofilms in iron limited media, 200 µM 2,2'-bipyridyl (Sigma) was added to tryptone media. At the end of the growth time, biofilms were rinsed with phosphate buffered saline (PBS) and taken for imaging using confocal microscopy.

2.2.4. Supernatant preparation

EcN WT and EcN *mcmA mchB* were revived from frozen stocks by streaking on LB agar plates. Single colonies from the LB plates were inoculated in 2 ml LB media and grown by shaking at 37 ºC for 6 h. 100 µl of the shaking culture was added to 100 ml of TB supplemented with 2,2'-bipyridyl and grown by shaking at 37 ºC for 24 h. The final supernatant samples were obtained after these cultures were centrifuged at 15,000 x *g* and filtered using a 0.2 µm membrane filter.

2.2.5 Planktonic growth assay in the presence of EcN supernatant

EcN WT and EcN *mchDEF* were grown in shaking Nutrient Broth supplemented with 200 µM 2,2'-bipyridyl at 37 ^{o}C overnight. Approximately 5 x 10^3 CFU/ml from an overnight culture were inoculated into 15 ml of tissue culture medium (DMEM/F12 with 10% fetal bovine serum (FBS); Invitrogen), and grown for 12 h. After 12 h EcN WT and EcN *mchDEF* supernatants were filtered with a 0.2 µm membrane filter and concentrated by centrifugation using 3 kDa centrifugal filter (Millipore). Then, 10 or 20 µL of the concentrated superantant were added to DMEM/F12 with 10% fetal bovine serum containing 5 x 10^3 CFU/mL of STm WT and grow aerobically at 37 ^{o}C. OD600 was then read at 10 h post-inoculation.

2.2.6. Microfluidic device construction

Microfluidic flow channel devices incorporating glass coverslip and polydimethylsiloxane (PDMS) (Dow chemicals) were used to image biofilm development in real-time. Microfluidic devices with 4 consecutive channels, each one configured as shown in Fig. 4A, with channel dimensions 10 x 0.5 x 0.25 mm (*l* x *w* x *h*) were fabricated using PDMS. Flow channels were molded by curing PDMS on lithographically defined SU-8 (microchem)

patterns on silicon wafers. A hole punch was used to make holes for the inlet and outlet lines. The PDMS was bonded to 24 x 50 mm glass coverslips by plasma cleaning both the surfaces.

2.2.7. Biofilm growth in microfluidic flow cells

All bacterial strains were revived from frozen stocks by streaking on LB agar plates. A single colony was inoculated into 2 ml LB media and grown by shaking at 37 ºC for 6 h. Ampicillin was added to cultures for STm pEmpty, STm pMchI and STm pMcmI at a concentration of 100 µl/ml to maintain the plasmids. Biofilms of all strains were seeded in the flow cells by flowing the planktonic culture of each strain into separate microfluidic channels and arresting flow for 2 h. Biofilms were grown by switching the feed line to each microfluidic channel to sterile supernatant supplemented with 100 µl/ml ampicillin and 5 µM of the membrane stain SynaptoRed C2 (FM4-64, Biotium) was then flowed through the channels at 2.5 ml/h for 15 h.

2.2.8. Crystal violet (CV) assay for biofilm biomass quantification

Biofilms were rinsed in PBS and then incubated with 1 ml of 0.1 % aqueous CV for 15 min at room temperature. The stained wells were rinsed with PBS and growth substrates were transferred to another clean well to quantify biomass accumulated on the substrates only. 2 ml of ethanol was added to the clean wells and incubated for 5 min at room temperature. The optical density of the dissolved CV in ethanol was obtained at 600 nm (OD600) and measured using a Biowave CO8000 cell density meter. All absorbance values were obtained from triplicate or greater number of samples and normalized to a self-consistent control within each experiment.

2.2.9 Laser scanning confocal microscopy (CLSM) imaging of biofilms

All confocal images were obtained using a Zeiss LSM780 inverted confocal microscope with 63X oil immersion objective. Dichroic beam splitters were used to reflect laser lines 488/561 nm. Green fluorescent protein (GFP) and mCherry expressing biofilms were excited with 488 nm and 561 nm laser lines, respectively. The SynaptoRed C2 membrane stain was excited using 561 nm laser line as well. In the case of coculture biofilms, both color channels were imaged using alternating line averaging to avoid blurring of the image due to sample drift. These adjustments reduced fluorescence cross-talk to undetectable levels in two-color imaging experiments. Confocal images were obtained with a *z* interval of 1 μm and a pinhole size of 1 airy unit.

The 3D coculture and monoculture microfluidic biofilm images were reconstructed using Volocity (Perkin Elmer). The biofilm-associated volume of cells ("biovolume") was quantified using the "select objects" function on the fluorescence intensity images from each channel after deconvoluting the images by applying the point spread function to each channel.

2.3. Results

2.3.1. EcN outcompetes STm in biofilms only during iron starvation

Competition between STm and EcN under iron limiting condition has been demonstrated in mouse models and planktonic cultures [51], but details of their competition in biofilms have not been studied. Using biofilm models, it was found that the competition between EcN and STm is only observed in iron limiting conditions. No significant difference was observed between

population fractions of wild type EcN and STm within 24 h coculture biofilms grown in iron rich, tryptone media. On the other hand, in biofilms grown in tryptone media supplemented with an iron chelator, 2,2'-bipyridyl, EcN WT is able to outcompete STm, comprising a much larger fraction of the biofilm (Fig. 5A). This indicate that iron limitation is a necessary condition to observe competition between STm and EcN during biofilm growth.

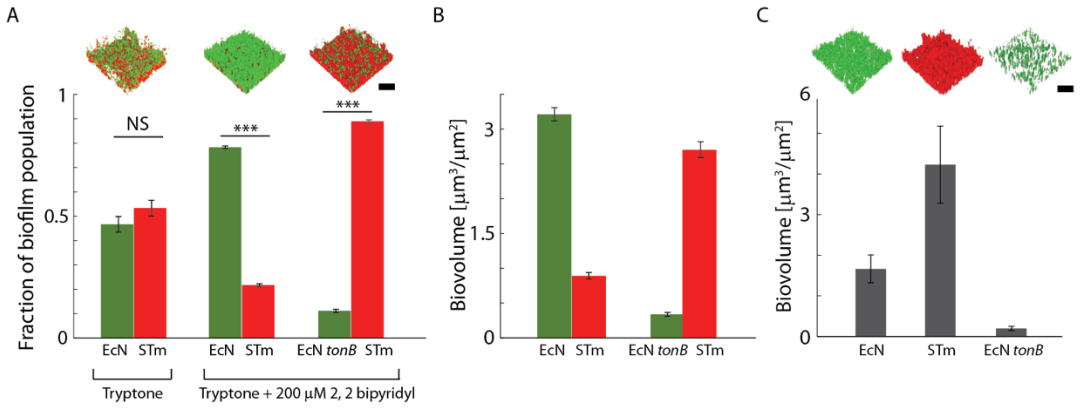

Fig 5. EcN inhibits STm growth in coculture biofilms during iron starvation. A) Population fractions of coculture biofilms of wild type EcN and STm grown in tryptone media, and EcN-STm and EcN *tonB*-STm cocultures grown in tryptone media supplemented with 2,2'-bipyridyl. B) Biofilm volumes (biovolume) of coculture biofilms of wild type EcN-STm and EcN *tonB*-STm grown in tryptone media supplemented with 2,2'-bipyridyl. C) Monoculture biofilms of EcN, STm, and EcN *tonB* grown in tryptone media supplemented with 2,2'-bipyridyl. Scale bars are 20 µm. *** represents p value < 0.001 and NS represents no significant difference.

The EcN *tonB* mutant, incapable of transporting iron-bound siderophores across the cell membrane, grows poorly both in monoculture and in competition with STm (Fig. 5B). EcN grows biofilms with less biovolume than STm WT in monocultures (Fig. 5C), but outcompetes STm by a significant margin in terms of relative biovolume in coculture biofilms (fig. 5B). These results indicate the importance of iron scavenging mechanisms in mediating the outcome of competition between these two species. Apart from producing two additional, chemically distinct siderophores compared to STm, EcN produces two antimicrobial microcins, H47 and M, which

play a significant role during competition in the gut [51,99]. Consequently, these microcins may play an essential role in competition between EcN and STm in this biofilm model.

2.3.2. EcN microcins inhibit STm biofilms

EcN microcins exhibit antibacterial activity against enteric pathogens in iron-limited medium and in the inflamed gut [99]. To determine whether STm inhibition by EcN is microcin-dependent we cocultured STm with EcN *mcmA mchB*, a mutant deficient in microcin production [99]. There was no significant difference between population fractions of EcN *mcmA mchB* and STm WT in biofilms grown in tryptone medium, but in tryptone supplemented with 2,2'-bipyridyl, STm outcompeted EcN *mcmA mchB* (Fig. 6A and B). Monoculture biofilms grown under iron limiting conditions show that both EcN *mcmA mchB* and STm WT have comparable biofilm growth rates when cultured alone (Fig. 6C), suggesting that microcins provide EcN an advantage in iron competition over STm in in biofilms, consistent with results from *in vivo* models [99].

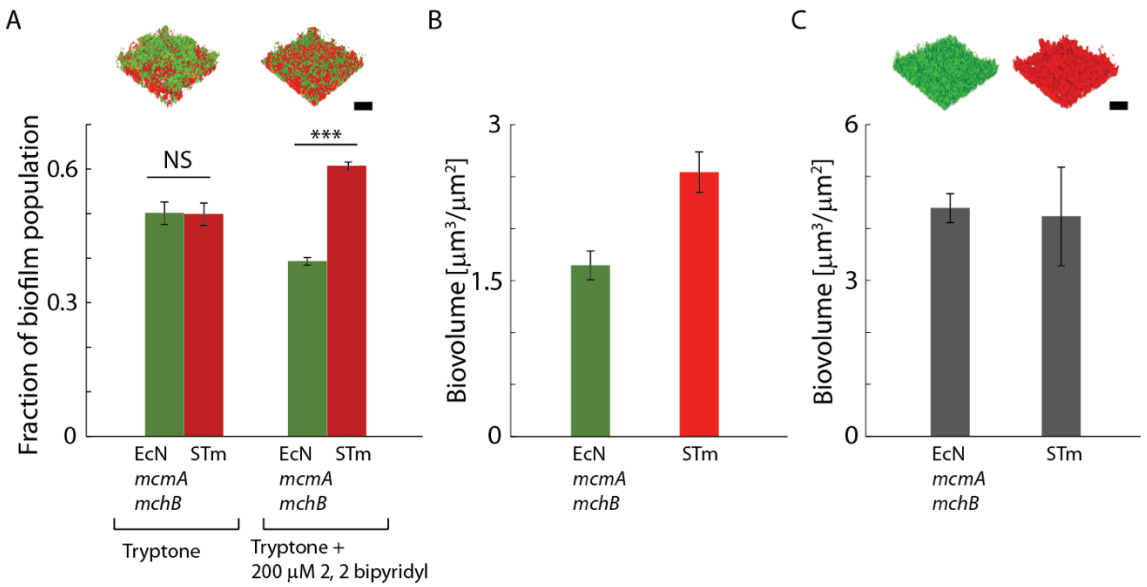

Fig. 6. STm outcompetes EcN *mcmA mchB* in coculture biofilms under iron starvation. A) Population fractions of coculture biofilms of EcN *mcmA mchB* and STm grown with and without 2,2'-bipyridyl in tryptone media. B) Biovolume of coculture biofilms of EcN *mcmA mchB* and STm grown in tryptone media supplemented with 2,2'-bipyridyl. C) Monocultures of EcN *mcmA mchB* grown in tryptone media supplemnted with 2,2'-bipyridyl. Scale bars are 20 µm. *** represents p value < 0.001 and NS represents no significant difference.

2.3.3. EcN uses STm enterobactin to outcompete STm in coculture biofilms.

Class IIb microcins have been characterized as Trojan horse antimicrobial peptides since it was described that microcin MccE492 produced by *Klebsiella Pneumoniae* can be post-translationally conjugated to siderophores [105,106]. It is suspected that also EcN microcins are post translationally modified to bind salmochelin. Data in Figures 5 and 6 are consistent with a mechanism by which EcN outcompetes STm in coculture as a result of STm using microcin-conjugated siderophores produced by EcN. STm produces, and can presumably exploit from the environment, the siderophores enterobactin and salmochelin. Under conditions where EcN is unable to conjugate microcins to siderophores, I expect the competition dominance by EcN to be diminished. To study the competition dynamics under conditions where EcN produces microcins but is unable produce its own enterobactin and salmochelin, we cocultured EcN *entC* and EcN

iroBC with STm (fig. 7A-C). EcN *entC* is an enterobactin biosynthesis mutant, and therefore also cannot make its own salmochelin. EcN *iroBC* can produce enterobactin, but it lacks the biosynthetic and transporter genes for salmochelin. Surprisingly, EcN *entC* outcompetes STm in coculture biofilm experiments (fig. 7A and B), while in monoculture biofilms, it grows significantly less biovolume than STm. Like STm, these results suggest that EcN exploits enterobactin from the environment and grows poorly when it is not present. In the case of EcN *entC*-STm cocultures, only STm produces enterobactin, and EcN *entC* is apparently able to use STm enterobactin to produce microcin-conjugated siderophores with resulting effects on iron competition similar to those of EcN WT. EcN *iroBC*, on the other hand, grows comparable biovolume biofilms as STm in monoculture, and it is outcompeted by STm when grown in coculture biofilms. These results suggest that *iroBC* are involved in salmochelin production and/or conjugation of microcins to siderophores. The consequence of this deletion renders EcN *iroBC* unable to compete with STm, and further establish the role of microcin-conjugated siderophores in EcN-STm iron competition in biofilms.

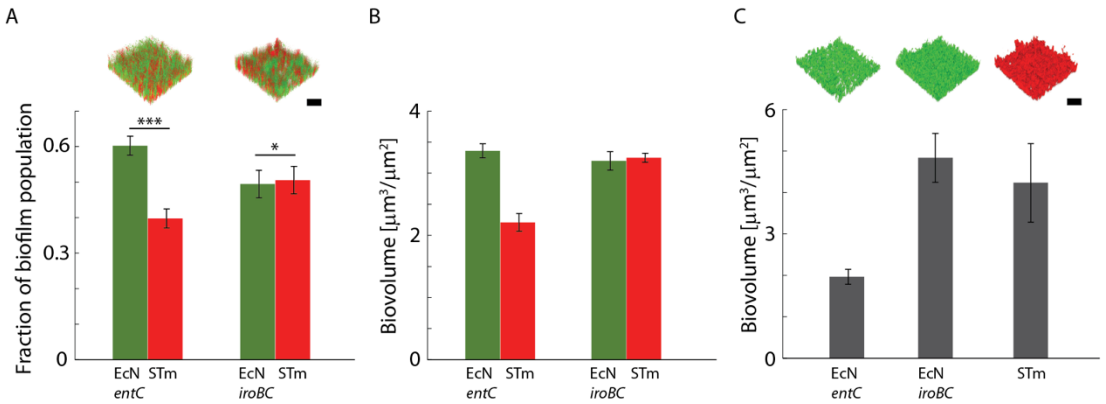

Fig 7. EcN uses STm-derived enterobactin to outcompete STm in coculture biofilms. A) Population fractions of coculture biofilms of EcN *entC* and STm, EcN *iroBC* and STm grown in tryptone media supplemented with 200 µM 2,2'-bipyridyl. B) Biofilm volume per scan area of coculture biofilms of EcN *entC* and STm WT, EcN *iroBC* and STm WT tryptone media supplemented with 2,2'-bipyridyl. C) Monoculture biofilm biovolumes of EcN *entC*, EcN *iroBC* and STm WT grown in tryptone media

supplemented with 200 µM 2,2'-bipyridyl. Scale bars are 20 µm. * and*** represents p value < 0.01 and 0.001 respectively.

2.3.4. EcN supernatant inhibits STm biofilms in microfluidic devices

To isolate the effect of microcins alone, STm shaking cultures and biofilms were exposed to EcN, *mcmA mchB,* and *mchDEF* supernatants. EcN *mchDEF* is a mutant deficient in transporter genes for microcins. Both EcN *mcmA mchB* and EcN *mchDEF* exhibit the same phenotype in cocultures with STm [99]. Figure 8A shows statically grown STm biofilms in EcN WT and EcN *mcmA mchB* supernatant. The biomass was normalized to STm biofilms grown in iron limited media which served as a control. There was no significant difference between the biofilms grown in EcN WT and EcN *mcmA mchB* supernatant. STm shaking cultures grown at 37 °C to a cell density of 5 x 10^3 CFU/mL and exposed to different concentrations of EcN and EcN *mchDEF* supernatant showed no inhibition in growth after 10 h (Fig. 8B and C). These observations indicate that the concentration of microcins was not sufficient to inhibit STm WT growth as seen in the in vitro biofilm cocultures of EcN and STm (Fig. 5 and 6), suggesting an effectively diminished concentration of microcins, possibly due to degradation, consumption, sequestration, or other mechanisms to reduce their overall effectiveness.

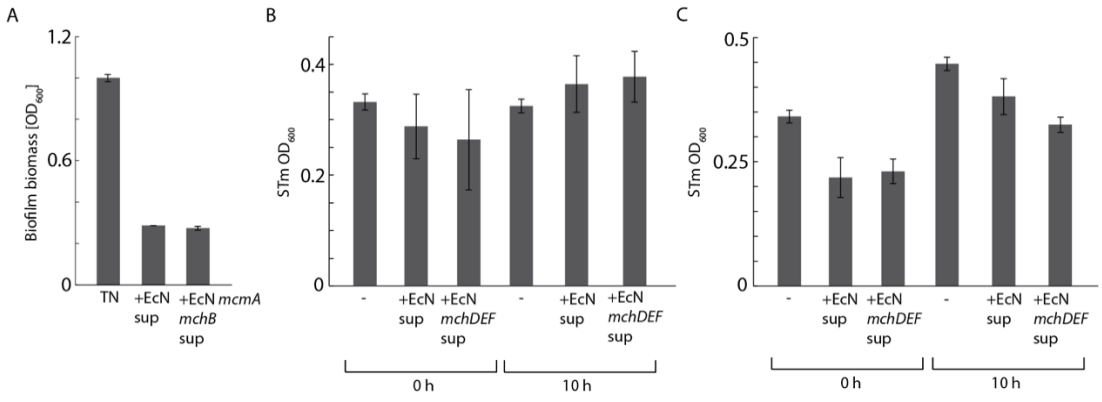

Fig. 8. STm static biofilm and shaking culture growth in EcN WT and microcin mutant supernatant. A) Biofilm biomass of STm grown in tryptone media supplemented with 2,2'-bipyridyl, and in EcN or EcN *mcmA mchB* supernatant (sup). B) Cell density of STm grown in shaking cultures in DMEM+10% FBS media (-), DMEM+10%FBS media + 10 µl EcN supernatant, and DMEM+10% FBS media + 10 µl EcN *mchDEF* supernatant for 0 and 10 h. C) Cell density of STm grown in shaking cultures in DMEM+10% FBS media (-), DMEM+10%FBS media + 20 µl EcN supernatant and DMEM+10% FBS media + 20 µl EcN *mchDEF* supernatant for 0 and 10 h.

In order to mimic the constant production of microcin-conjugated siderophores in EcN-STm cocultures while controlling for contact-dependent inhibition mechanisms, I monitored the growth of STm in a microfluidic flow cell device as a function of exposure to EcN mutant supernatants. EcN WT or EcN *mcmA mchB* cell free supernatant was flowed through the growth channels continuously for the growth period of 15 h, providing a constant concentration of microcin, or lack thereof. STm biofilms grown in the presence of EcN WT supernatant grew significantly less biomass than STm biofilms exposed to EcN *mcmA mcmB* supernatant (fig. 9A). To show that the growth inhibition effect is due to microcin production, the STm WT strain was transformed with plasmids bearing microcin immunity genes [99]. These were pMchI, which provides immunity to microcin H47, to which STm is naturally immune [99]; pMcmI, which provides immunity to microcin M; and pEmpty, the empty plasmid. When these three strains were grown in continuously flowing EcN WT supernatant, I observed biofilm growth inhibition in STm pEmpty and STm pMchI, which both provide no additional immunity to EcN microcins beyond that already present in the STm WT. However, STm pMcmI grown in EcN WT supernatant grew significantly more biofilm in comparison to STm pEmpty and STm pMchI (Fig. 9B). This indicate that growth inhibition in STm WT biofilms is primarily due to microcin M, though a constant concentration of microcins in the growth environment is required observe it. In cocultures of EcN with STm, microcins are maintained at a constant concentration by EcN present in the biofilms, which results in STm biofilm inhibition.

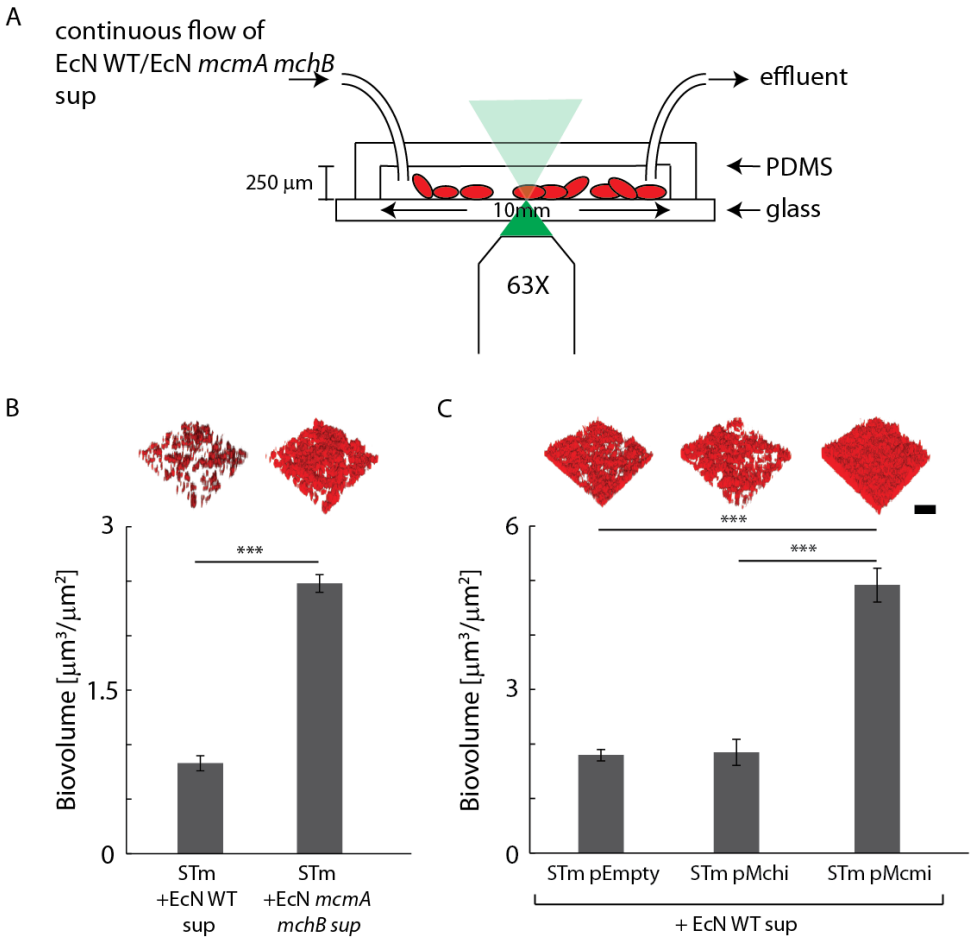

Fig. 9. STm biofilms grown in microfluidic devices. A) Schematic of microfluidic device design used for constant flow growth of STm biofilms. Biofilms were imaged *in situ* through the transparent glass substrate by CLSM. B) Biovolume of STm biofilms grown for 15 h in microfluidic device in EcN and EcN *mcmA mchB* supernatant (sup). C) Biovolume of STm pEmpty, STm pMchI and STm McmI biofilms grown for 15 h in microfluidic device in EcN WT supernatant (sup). Scale bar is 20 µm. *** represents p value < 0.001.

Interestingly EcN WT supernatant prepared from EcN WT cultures grown for 15 h instead of 24 h did not inhibit STm WT biofilms, indicating that sufficient microcin production for STm growth inhibition occurs only at longer growth times (Fig. 10).

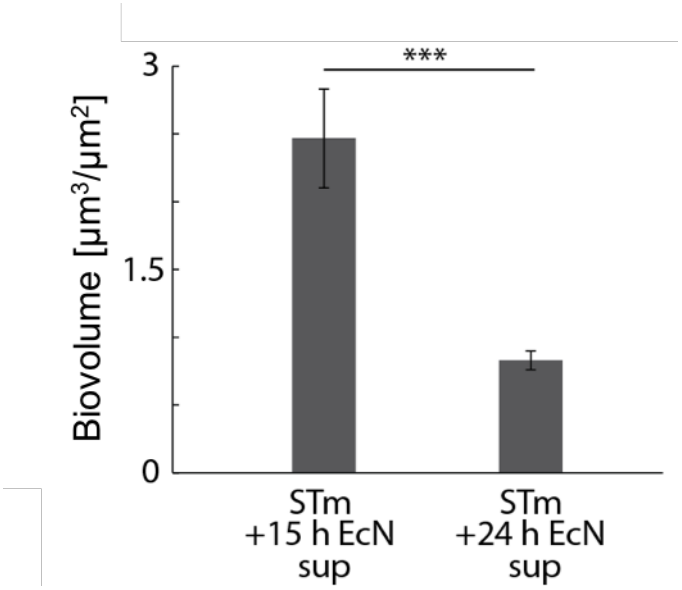

Fig. 10. **Effect of EcN culture time on supernatant inhibition of STm biofilms**. Biovolume of STm biofilms grown for 15 h in microfluidic channels in EcN supernatant (sup) extracted from cultures grown for 15 and 24 h.

2.3.5. EcN microcins inhibit adherent invasive E. coli (AIEC) growth.

In an inflamed gut, EcN outcompetes several pathogens in addition to STm. AIEC is a gut pathogen that exhibit greater capability of adhesion to intestinal epithelial cells than other gut bacteria, and the adhesion process is augmented by secretion of host macrophages and lymphocytes [107]. These *E. coli* strains are extremely invasive and enters intestinal epithelial cells, causing damage by mechanical cell disruption. The increased levels of lipopolysaccharide and flagelin in AIEC strains leads to chronic inflammation in the gut, leading to an altered gut microbiota that is greatly susceptible to other pathogens [107]. To demonstrate the effect of EcN WT microcins in inhibiting growth of other gut pathogens, we exposed an AIEC strain to continuously flowing EcN WT and EcN *mcmA mchB* supernatant in a microfluidic device (fig. 11). We observed significant AIEC biofilm growth inhibition under EcN WT supernatant flow compared to biofilms grown in EcN *mcmA mchB* supernatant. These results demonstrate that

coculture competition dynamics of other gut pathogens can also be studied using the proposed biofilms model.

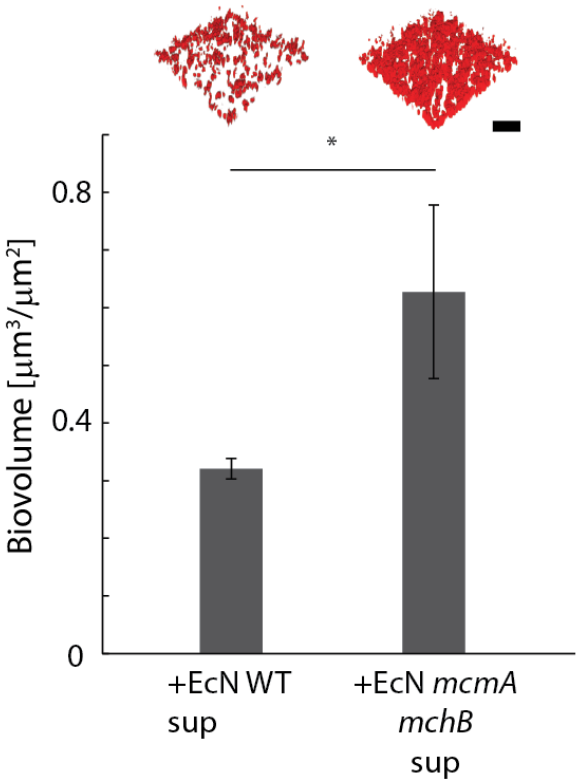

Fig. 11. **AIEC biofilms in microfluidic devices**. AIEC biofilms grown for 15 h in microfluidic device in EcN WT and EcN *mcmA mchB* supernatant. Scale bar is 20 µm. * represent p value < 0.05.

2.4. Discussion

In this paper, I develop an *in vitro* biofilm model that recapitulates the competition dynamics between EcN and STm as shown previously in murine models [51,99]. I demonstrate the essential role of microcins during EcN and STm iron competition in biofilms. The results in this chapter show that microcin mediated inhibition of gut pathogen is not contact dependent, however microcins are required at a constant concentration to inhibit STm biofilm growth, which was achieved using microfluidics devices. Microcins are metabolically costly products and are produced in minimum quantities by the bacteria which makes their extraction and purification

process difficult [108–111]. STm growth inhibition is mediated by microcins with post-translational modification to conjugate siderophores, which requires extractions of modified microcins from the pool for modified and unmodified microcin making the extraction process tedious [105,106]. The static and microfluidic *in vitro* biofilm models, on the other hand, simplify the study of competition mediated by microcins and siderophores, and they provide well resolved temporal and spatial information about community structure that is difficult to acquire through *in vivo* studies. Previous studies provide evidence that microcins M and H47 are post-translationally modified, however there is no information regarding the compound conjugated after the modification [88]. My results indicate that both microcins and *iroBC* genes are required for growth inhibition of STm. In contrast, an EcN *entC* mutant can outcompete STm, suggesting that EcN could be using STm enterobactin and salmochelin for post-translational modification of microcins. Previous work on *Klebsiella pneumonia* shows that the presence of unmodified microcins and salmochelin in supernatant is not enough to produce an antibacterial effect [112]. This has not been proven in the case of microcin M of EcN and the data in this chapter provides indirect evidence that *iroBC* may be required for post-translational modification of microcin in EcN.

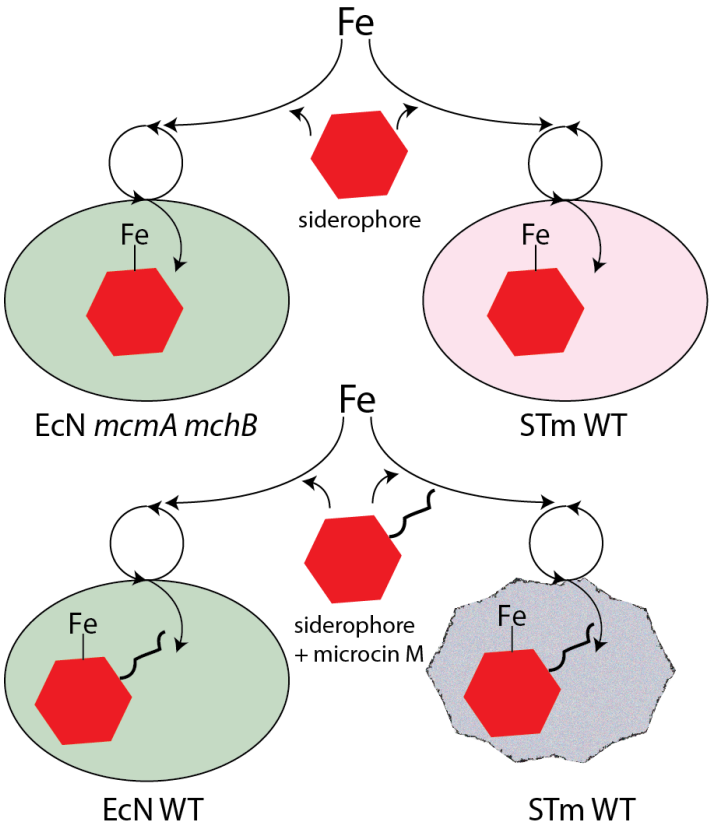

Fig. 12. Schematic showing the proposed anti-cheating mechanism of the siderophore-microcin conjugate.

2.5. Conclusion

In conclusion, these results provide evidence that *in vitro* biofilm models can be used to study competition dynamics of *Enterobacteriaceae*. The data in this chapter agree with previous *in vivo* findings and provide evidence supporting the hypothesis that microcins act as an anti-cheating device of EcN [99] (Fig. 12). Using microfluidic devices, I show that microcins are required at a constant concentration to induce pathogen growth inhibition, while growth assays and static biofilm growth in supernatant could not provide this information. Biofilm competition models in static and microfluidic devices will further our understanding of multispecies interactions of *Enterobacteriaceae* in the gut by providing the ability to separate different

signaling and metabolite based interactions, which *in vivo* models do not. Elucidation of such dynamics will better our understanding of underlying mechanism of the complex relationship between host and microbiota and provide potential target for intervention strategies.

Using similar *in vitro* biofilm models, the next chapter describes an antagonistic interaction between *E. coli* K12 and *P. aeruginosa*. These models prove critical to isolating compounds responsible for an unprecedented mechanism of cell-cell communication in this coculture system.

Chapter 3.

Rhamnolipid mediate an interspecies dispersal signaling pathway

3.1. Introduction

In medical settings, biofilms are detrimental to patient outcomes, and they increase the resistance of constituent cells to conventional treatment with antibiotics and biocides.[113] The development of methods to disperse biofilms, therefore, represents a promising strategy to combat bacterial infections.[19] Many aspects of biofilm development and properties are determined in response to diffusible signals,[114] as is biofilm dispersal. Chemical compounds that induce biofilm dispersal range from specific molecular signals and dispersants[61] (Fig. 13) to nutrients and metabolites with more general activity.[24,115,116]

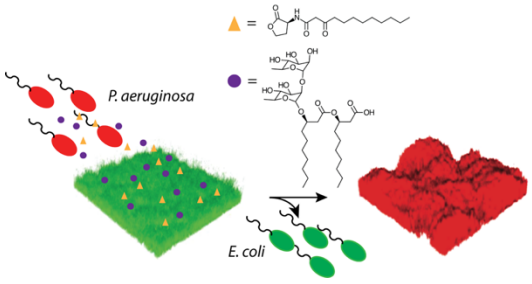

Fig. 13. Dispersal of *E. coli* biofilms by *P. aeruginosa* QS compounds. Figure describes the components involved in the dispersal signaling process of *E. coli* by *P. aeruginosa*

Natural dispersal processes via specific signaling pathways serve as promising inspiration for anti-biofilm strategies. Many species produce autodispersal signaling compounds to escape unfavorable conditions and colonize new niches.[117–120] Similarly, interspecies dispersal signaling mediates many forms of competition.[118,121–123] Various compounds facilitate dispersal processes, such as biofilm matrix degrading enzymes,[117,124,125] specific signaling compounds,[126,127] peptide

or metabolite signals,[117,128] and biosurfactants.[121,122] Many compounds active in dispersal signaling bind specific receptors to differentially regulate expression of genes related to active dispersal.[19,129] Some bacteria-derived dispersants have a general dispersal effect on some species, such as rhamnolipids, a class of biosurfactants secreted by *P. aeruginosa*.[121]

P. aeruginosa produces several di- and mono-rhamnolipid congeners, through expression of enzymes RhlABC,[130–132] depending on growth conditions and strain.[133] Rhamnolipids exhibit a variety of functions, modulating cell-cell contact, attachment to surfaces, maintaining open channels within the biofilm for transport of nutrients, formation of macro-colonies and three-dimensional biofilm architecture development,[134,135] as well as mediating dispersal processes in *P. aeruginosa* biofilms.[136] Rhamnolipids also promote the uptake of hydrophobic substrates,[137] have antimicrobial properties, and act as virulence factors during an infection.[137]

In this study, I show that, in addition to the above functions, rhamnolipids produced by *P. aeruginosa* play a critical role in an interspecies chemical signaling for biofilm dispersal. *E. coli* biofilms disperse when inoculated with planktonic *P. aeruginosa* cultures, and specific compounds in the culture supernatant are responsible for triggering this dispersal response. While alone, rhamnolipids lack any growth inhibition or biofilm dispersal activity towards *E. coli*, but they act cooperatively with a *P. aeruginosa* quorum sensing (QS) compound, N-(3-oxo-dodecanoyl) homoserine lactone (3oxoC12HSL), to disperse *E. coli* biofilms. The results suggest that rhamnolipids selectively alter the permeability of *E. coli* membranes to certain molecules and do so specifically for lipophilic AHLs such as 3oxoC12HSL. Furthermore, I show that the removal of lipopolysaccharide (LPS) from the *E. coli* outer membrane by exposure to rhamnolipids represents a potential, though not exclusive, mechanism for inducing the observed selective permeability.

3.2. Materials and methods.

3.2.1. Bacterial culture and biofilm growth conditions

The bacterial strains used in this study are listed in the table A.1. All culture materials were obtained from Fisher Scientific unless otherwise noted. All bacterial strains were streaked on Lysogeny broth (LB) agar plates from frozen glycerol stocks and grown overnight at 37˚ C. Shaking cultures were inoculated from a single colony from the LB plate into 2 ml of liquid LB and grown at 37˚ C on an orbital shaker at 250 rpm for 6 h.

Static biofilms were grown on submerged 18 x 18 mm coverslips in 6 well plates at 22˚ C. Stationary phase shaking cultures were diluted 1:1000 into 10 g/l bacto tryptone (TB) medium and dispensed into the wells. Flow cell biofilms were grown in the microfluidic device depicted in fig. 25. Shaking cultures were diluted 1:1000 into TB media and pulled through the entire device using a syringe pump. Flow was then stopped for 2 h to seed the biofilm. The inoculum was then replaced by sterile TB and continuously pulled through the channel at a flow rate of 10 µl/h for the duration of the experiment. Unless indicated otherwise, all *E. coli* planktonic cultures and biofilms used in this study were grown from *E. coli* strain MC4100.

3.2.2. *P. aeruginosa* culture supernatant preparation

P. aeruginosa supernatant was prepared by diluting 100 µl of a shaking culture into 100 ml of TB and grown for 15 h at 37˚ C on an orbital shaker at 250 rpm. Cultures were then centrifuged at 15000 x *g* and the resulting supernatant was passed through a 0.2 µm PES vacuum filter. For dispersal experiments, biofilms were exposed to the supernatant for 6 h.

3.2.3. Crystal violet assay of biofilm-associated biomass

Mature *E. coli* biofilms were gently rinsed with phosphate-buffered saline (PBS, pH 7.4), and then incubated in 2 ml of 0.1% crystal violet (CV) for 15 min after which the CV solution was aspirated. Biofilms were rinsed with PBS once again then exposed to 2 ml of ethanol for 15 min. The optical density of the dissolved CV was obtained at 600 nm (OD_{600}) and measured using a Biowave CO8000 cell density meter.

3.2.4. N-acyl homoserine lactone (AHL) biofilm dispersal experiments

AHLs (Sigma-Aldrich) were prepared as 5 mM stock solutions in dimethyl formamide (DMF). 24 h biofilms were exposed to different concentrations of 3oxoC12HSL and N-butyryl-L-homoserine lactone (C4HSL) in PBS for 6 h. The AHL solutions were aspirated and the biofilms were rinsed with PBS and used for CV assays.

3.2.5. Extraction and purification of rhamnolipids

Rhamnolipids were purified directly from *P. aeruginosa* str. PA14. A 200 ml culture of PA14 was grown in TB for 15 h, the supernatant was extracted and rhamnolipids were precipitated as previously described. [134] The supernatant was acidified by the addition of 1 M HCl to achieve a pH ~ 2. The acidified supernatant was left at 4˚ C overnight and then centrifuged at 15000 x *g* for 15 min, discarding the supernatant. The pellet was dispersed in 1 ml methanol and passed through a 24/40 chromatography column loaded with amberlite XAD-7 resin equilibrated in water. Rhamnolipid fractions were eluted using mobile phase steps of 20 ml 20% methanol, 20 ml of 40% methanol, 100 ml of 60% methanol and 20 ml of 80% methanol in water respectively. Each fraction was analyzed using mass spectroscopy and two predominant rhamnolipid peaks were detected at m/z of 503 and 649 for mono and di- rhamnolipids, respectively.

Chromatography fractions were also analyzed for presence of 3oxoC12HSL and any fraction containing 3oxoC12HSL was not used for experiments. All other rhamnolipid-containing fractions were combined, dried under a filtered stream of air, and weighed.

3.2.6. Biofilm cell permeability assays

Biofilms exposed to different concentrations of rhamnolipids were rinsed with PBS and exposed to a mixture of 0.4% trypan blue (TpB) and 2 μM SYTO 9 prepared in PBS for 15 min or a mixture of propidium iodide (PI) (4 μM) and SYTO 9 (2 μM) mixture at 2:1 ratio for 15 min. Biofilms were then rinsed with PBS to remove excess dye and imaged using confocal microscopy. TpB, PI and SYTO 9 were purchased from Life Technologies.

3.2.7. Liquid Chromatography-Mass Spectrometry (LC-MS) detection of AHLs in *E. coli* cells

100 ml of LB media was inoculated with a 1:1000 dilution of 2 ml *E. coli* shaking cultures and grown for 15 h. The cells were centrifuged at 2000 x *g* for 10 min and resuspended in PBS. 1 ml aliquots of cells were exposed to different AHLs, as indicated, at 50 μM concentration. The cells were exposed to AHL solutions for 1 h and washed with PBS in a second centrifugation step to remove any AHL in solution. The cell pellets were then lysed using 300 μl of 2:2:1 acetonitrile:methanol:water and left overnight at -20˚ C. The extraction was then centrifuged at 17000 x *g* and supernatant retained for LC-MS analysis. Extracts were analyzed at the UC Irvine Mass Spectrometry Core using a Waters Micromass Quattro Premier XE LC-MS running a C18 column using a 20 min linear gradient of 5% acetonitrile to 95% acetonitrile (supplemented with 0.1% acetic acid) in positive ion mode.

3.2.8. Cyclic di-GMP quantification:

E. coli cells grown in LB shaking cultures without salt were harvested at late log phase. Cyclic di-GMP (c-di-GMP) was purified after exposure to supernatant, dispersal solution and PBS using a previously established protocol.[138] Cells from 100 ml shaking cultures grown for 15 h were centrifuged at 2000 x *g* and the supernatant was discarded. The cells were then exposed to 5 ml of PBS, PA14 supernatant, or the dispersal solution (50 µM each of 3oxoC12HSL and rhamnolipids) for 1 h. The cells were then centrifuged at 2000 x *g* and washed with PBS. 250 µl of extraction solvent, consisting of 2:2:1 acetonitrile:methanol:water in 0.1N formic acid was added to the pellet and left in -20˚ C for 30 min. Cells debris was centrifuged at 17000 x *g* for 5 min and the supernatant was retained. The pellet was re-extracted with an additional 250 µl of extraction solvent and the resultant supernatant was combined with the supernatant from the first extraction. The aggregated supernatant was neutralized with 15% $(NH_4)_2HCO_3$. LC-MS data were obtained by the same method as for AHLs described above.

3.2.9. Purpald assay for Lipopolyssacharide (LPS) removal

1 ml of 15 h *E. coli* LB shaking culture was pelleted at 2000 x *g* for 5 min. The pellet was resuspended in 1 ml of different concentrations of rhamnolipids dissolved in PBS for one hour. Cells were centrifuged at 17000 x *g* and the supernatant was used to measure the amount of LPS removed from the cell membranes using the purpald assay as detailed previously. [139]

3.2.10. Confocal microscopy imaging:

All confocal images were obtained using a Zeiss LSM780 inverted confocal microscope with 63X water immersion objective. The constitutively expressed yellow- and red-fluorescent proteins (YFP & RFP) were excited with 488 and 555 nm laser lines, respectively. The same laser settings were used for SYTO 9 and PI imaging, respectively. The 405 nm laser line was used for TpB imaging. All channels were imaged using line averaging to avoid blurring of the image due to drifting. These adjustments reduced signal cross-talk to undetectable levels in two-color imaging experiments. The images were obtained with a *z* interval of 1 μm and a pinhole size of 1 airy unit. The amount of biomass of biofilms was quantified using the "select objects" of the intensity images from each channel using Volocity after deconvoluting the images by applying the point spread function to each channel.

3.2.11. Dispersed *E. coli* cell viability by colony forming unit (CFU) assays

E. coli biofilms were grown in 6-well plates for 24 h and exposed to a mixture of 1 ml aqueous solution of 50 μM rhamnolipids and 50 μM 3oxoC12HSL (dispersal solution, DS), 1 ml DI water and 1 ml *P. aeruginosa* cell free supernatant for 12 h. The biofilms exposed to DS and supernatant dispersed over 12 h and the biofilm exposed to water was mechanically disrupted. The dispersed cells from all the biofilms were collected and CFUs were counted by serial dilution on to 1.5% LB agar plates.

3.2.12. Growth curves

Growth curves were obtained by absorbance measurements of shaking cultures. 0.06 ml of an overnight *E. coli* LB culture was diluted into 60 ml of LB, mixed well, and divided into 1 ml

aliquots which were incubated at 37˚ C and 250 rpm. One tube was taken out every hour and OD_{600} was measured using a Biowave CO8000 cell density meter.

3.2.13. Microfluidic device fabrication and dynamic biofilm imaging.

A single channel microfluidic device of channel dimensions 10 x 1 x 0.12 mm was fabricated as shown in fig. 25. The channel was patterned using SU-8 photoresist on a silicon wafer. Polydimethylsiloxane (PDMS, Sylgard 184, Dow Corning) was mixed, degassed, and poured on the SU-8 patterns to mold the channel. Holes for tube connections were cut into the PDMS with a hole punch and the PDMS was bonded to a glass coverslip by plasma cleaning both the surfaces, pressing them together and baking at 150˚ C for 1 h.

For real-time imaging experiments, biofilms were grown using the MC4100 *yfp* constitutively fluorescing strain with the conditions described above. The time series images of biofilms in the microfluidic devices were obtained using a 63X oil immersion objective in the same microscope as above. At least 3 images were obtained along the channel every 30 min. All other settings were kept the same as described in confocal imaging above. Movies were obtained by imaging the same section of the channel during treatment at 30 min intervals.

3.3. Results

3.3.1. *P. aeruginosa* spent medium triggers dispersal of *E. coli* biofilm:

Shaking cultures of *E. coli* K12 MC4100 strain were inoculated from a single colony from the LB plate into 2 ml of liquid LB and grown at 37˚ C on an orbital shaker at 250 rpm for 6 h. Biofilms of MC4100 were grown on submerged coverslips in static growth media by diluting the shaking culture to an OD of 0.02. The biofilms were grown in 6 well plates for 24 h at 22 ˚C.

Upon exposure of mature biofilms of *E. coli* to planktonic *P. aeruginosa* strain PA14 cells, the *E. coli* biofilms were displaced by *P. aeruginosa* biofilms within 24 h, as assessed by confocal microscopy imaging (Fig. 14A).

I hypothesized that *E. coli* biofilms may be displaced in response to compounds in the *P. aeruginosa* spent medium. *P. aeruginosa* supernatant was prepared by diluting 100 µl of a shaking culture into 100 ml of TB and grown for 15 h at 37˚ C on an orbital shaker at 250 rpm. Cultures were then centrifuged at 15000 x *g* and the resulting supernatant was passed through a 0.2 µm PES vacuum filter. For dispersal experiments, biofilms were exposed to the supernatant for 6 h.

Mature *E. coli* biofilms exhibited significantly reduced biomass in a dose-dependent response to the culture supernatant of *P. aeruginosa* (Fig. 14B) as measured by the crystal violet assay. Biofilms of several other *E. coli* K-12 strains, including BW25113, ZK2586, W3110, and MG1655, and a uropathogenic strain, CFT073, exhibited a similar reduction of biomass in response to *P. aeruginosa* culture supernatant (Fig. 14C). *E. coli* biofilms also dispersed in response to the conditioned medium of another common *P. aeruginosa* strain, PA01 (Fig 15).

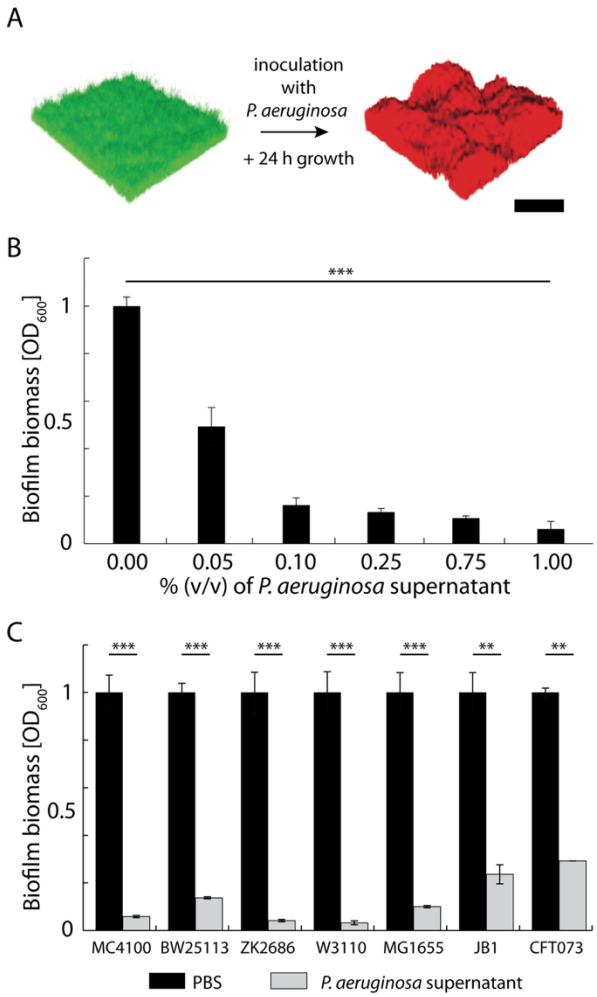

Fig 14. Reduction of *E. coli* biofilms by soluble factors in *P. aeruginosa* supernatant. A) Confocal fluorescence microscopy images of *E. coli* biofilm displacement upon inoculation with *P. aeruginosa*. B) Surface associated biomass of *E. coli* biofilms retained on growth substrates following exposure to different concentrations of *P. aeruginosa* supernatant. C) Surface associated biomass of biofilms of various *E. coli* strains retained on growth substrates following exposure to 100% v/v *P. aeruginosa* supernatant. ** and ***, $p < 0.01$ and 0.001, respectively.

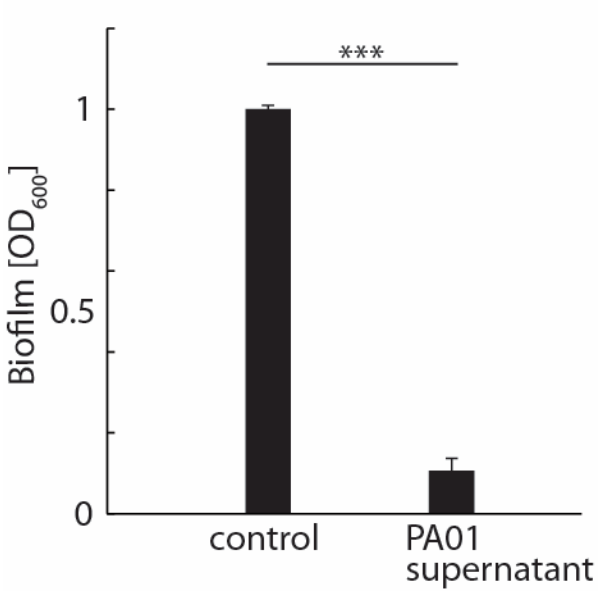

Fig. 15. Biofilm biomass of 24 h *E. coli* biofilms exposed to *P. aeruginosa* PA01 WT supernatant. *** indicates $p < 0.001$.

3.3.2. Components of *P. aeruginosa* culture supernatant trigger *E. coli* biofilm dispersal:

In addition to the observed decrease in biomass of *E. coli* biofilms shown in Figure 14, exposure of these biofilms to *P. aeruginosa* culture supernatant resulted in 2 x 10^7 colony forming units (CFU) per ml in the supernatant of these biofilms, suggesting a dispersal response (Fig. 16). *E. coli* biofilms were grown in 6-well plates for 24 h and exposed to a mixture of 1 ml aqueous solution of 50 µM rhamnolipids and 50 µM 3oxoC12HSL (dispersal solution, DS), 1 ml DI water and 1 ml *P. aeruginosa* cell free supernatant for 12 h. The biofilms exposed to DS and supernatant dispersed over 12 h and the biofilm exposed to water was mechanically disrupted. The dispersed cells from all the biofilms were collected and CFUs were counted by serial dilution on to 1.5% LB agar plates. While high, this concentration was 55-fold lower than that of mechanically disrupted biofilms (1.1 x 10^9 CFU/ml), indicating a cytotoxic effect of the *P. aeruginosa* supernatant as well.

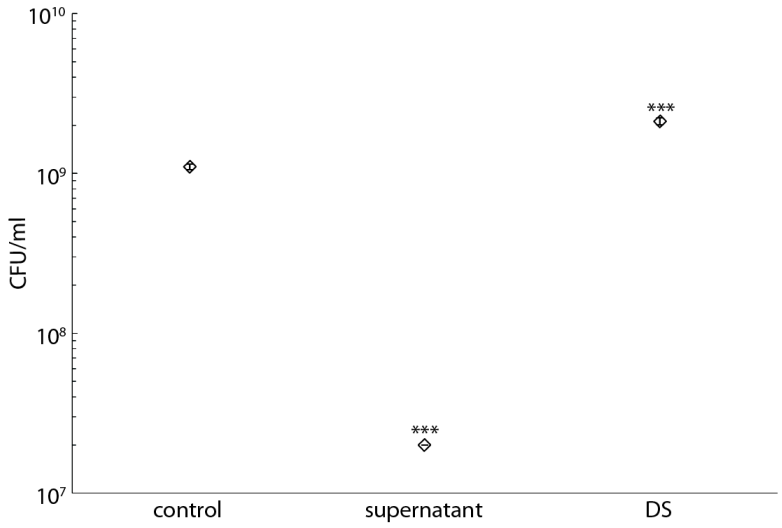

Fig. 16. Colony Forming Units (CFUs) from *E. coli* cells removed from biofilms by chemical (*P. aeruginosa* culture supernatant or 50 µM rhamnolipid - 50 µM 3oxoC12HSL dispersal solution [DS]) or mechanical dispersal into PBS (control). *** indicates $p < 0.001$.

To search for chemical dispersal triggers, *E. coli* biofilms were exposed to the culture supernatants of *P. aeruginosa* deletion mutants deficient in various quorum sensing (QS) system small molecule components (Fig 17A). Supernatants from the Δ*pqsA*, Δ*pqsH*, Δ*phz*1/2, 2x*phz*, and Δ*rhlI* mutants retained WT activity towards *E. coli* biofilms, while Δ*lasI*, Δ*lasI*Δ*rhlI* mutants exhibited no significant effect on biofilm biomass. Neither the Δ*lasI* nor Δ*lasI*Δ*rhlI* mutants produce 3oxoC12HSL, and therefore this QS compound was targeted as a possible dispersal trigger. *E. coli* biofilms exposed to 3oxoC12HSL at various concentrations dispersed to a significant extent, but not to the degree observed for the full *P. aeruginosa* supernatant (Fig. 17B), suggesting that a critical component for *E. coli* biofilm dispersal was missing.

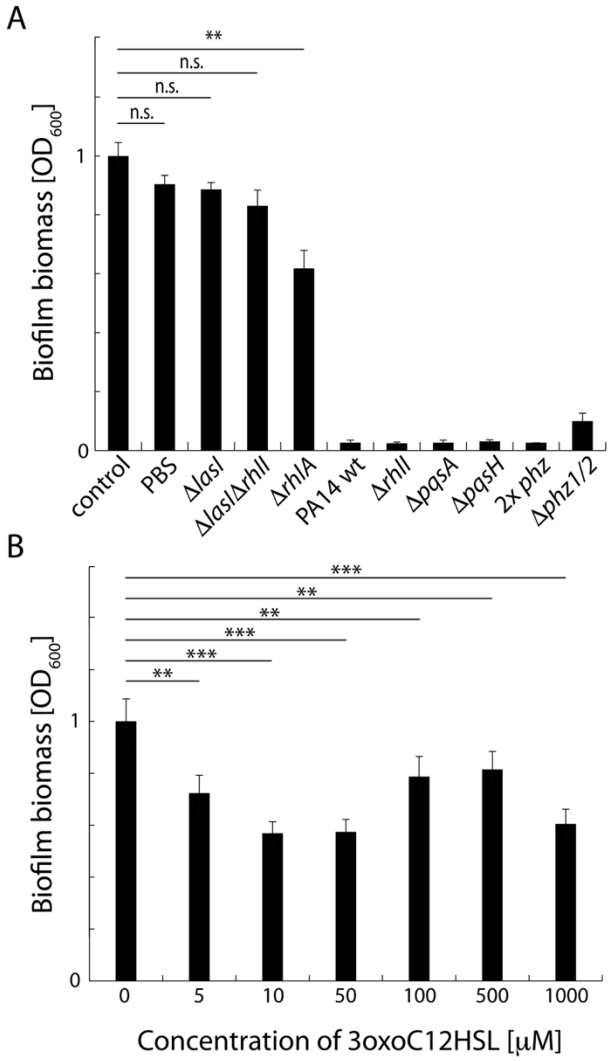

Fig. 17. Components of *P. aeruginosa* QS pathways that trigger *E. coli* biofilm dispersal. A) Biomass of *E. coli* biofilms retained on growth substrates after exposure to the supernatant of *P. aeruginosa* wt and deletion mutants. The control biofilm is exposed to tryptone growth medium. B) Dose-dependent dispersal of *E. coli* biofilms exposed to purified 3oxoC12HSL. ** and ***, $p < 0.01$ and 0.001, respectively; n.s., difference was not significant.

The Δ*rhlI* mutant fully dispersed *E. coli* biofilms, indicating that the compound produced by RhlI, N-butyryl-L-homoserine lactone (C4HSL), is not responsible for the observed reduction in *E. coli* biofilm biomass when exposed to the full *P. aeruginosa* supernatant. This result is further supported by the lack of dispersal activity of solutions of C4HSL (Fig. 18A). The supernatant from *P. aeruginosa* Δ*rhlA*, on the other hand, resulted in significant, but partial,

reduction of biomass of *E. coli* biofilms (Fig. 17A), similar to the effects of 3oxoC12HSL (Fig. 17B).

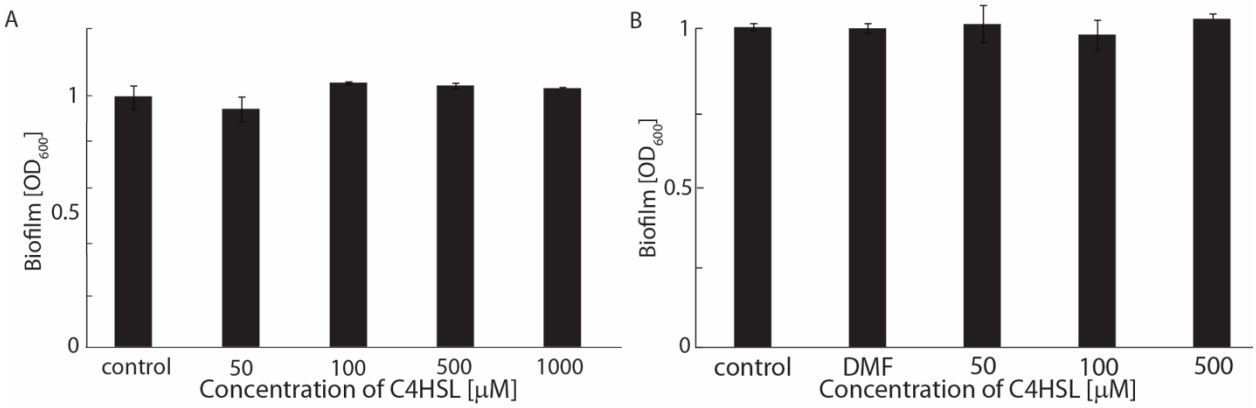

Fig. 18. Crystal violet essay. Amount of biofilm biomass measured by crystal violet assay of 24 h *E. coli* biofilms exposed to different concentrations of C4HSL. (B) Amount of biofilm biomass measured by crystal violet assay of 24 h *E. coli* biofilms exposed to 50μM rhamnolipids and different concentrations of C4HSL.

Treatment of *E. coli* biofilms with varying concentrations of 3oxoC12HSL and purified rhamnolipids enhanced dispersal (Fig. 19A). An aqueous solution of 3oxoC12HSL and rhamnolipids at a concentration of 50 μM each (dispersal solution, DS) was sufficient to completely recapitulate the extent of the dispersal response of *E. coli* biofilms in response to the full *P. aeruginosa* supernatant. The observed dispersal effect is cooperative, exhibiting a non-monotonic dependence on the concentration of both components and reducing biomass of *E. coli* biofilms 92% more than 50 μM 3oxoC12HSL alone. The only other AHL produced by *P. aeruginosa*, C4HSL, did not disperse *E. coli* biofilms even in combination with rhamnolipids (Fig. 18B). Moreover, *E. coli* biofilms exposed to rhamnolipid concentrations up to 2 mM showed no reduction in biomass (Fig. 19A & 20), and rhamnolipids do not affect the growth of planktonic *E. coli* cultures (Fig. 21).

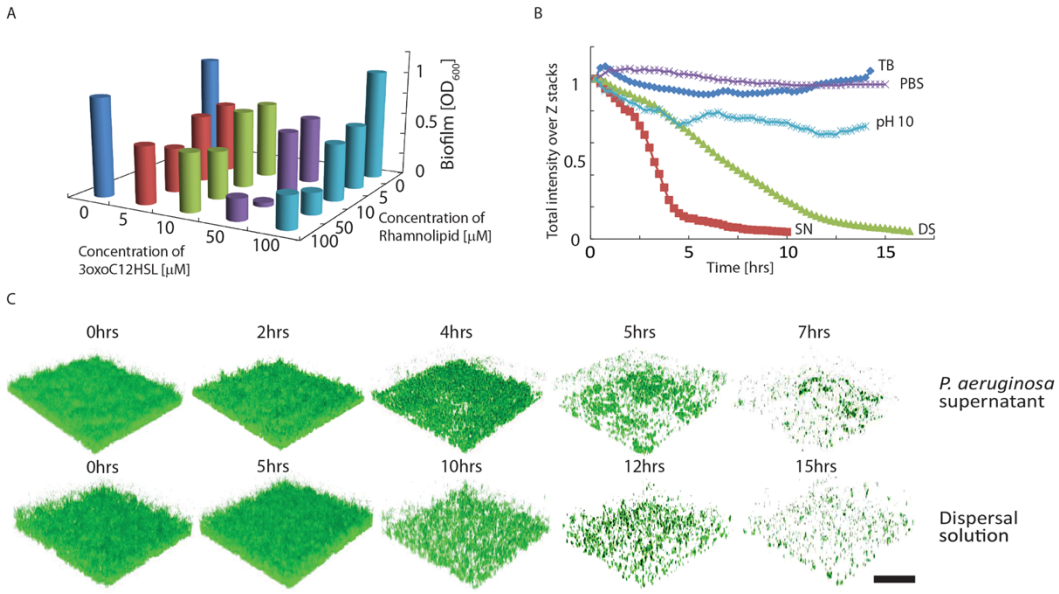

Fig. 19. Cooperative effect of rhamnolipids and 3oxoC12HSL on *E. coli* biofilm dispersal. A) Biomass of *E. coli* biofilms retained after exposuse to binary mixtures of 3oxoC12HSL and rhamnolipids. B) Dipsersal dynamics of *E. coli* biofilms. The adhered biomass was assessed by the integrated fluorescence intensity of *E. coli* biofilms in flow channels exposed to PA14 supernatant (SN), 50μM 3oxoC12HSL and 100μM rhamnolipids (DS), and controls of pH 10 buffer solution, PBS, and TB in a single channel microflidic device. C) Confocal fluorescence microscopy images of *E. coli* biofilms dispersed over time during exposure to PA14 supernatant and DS. Scale bar is 20 μm.

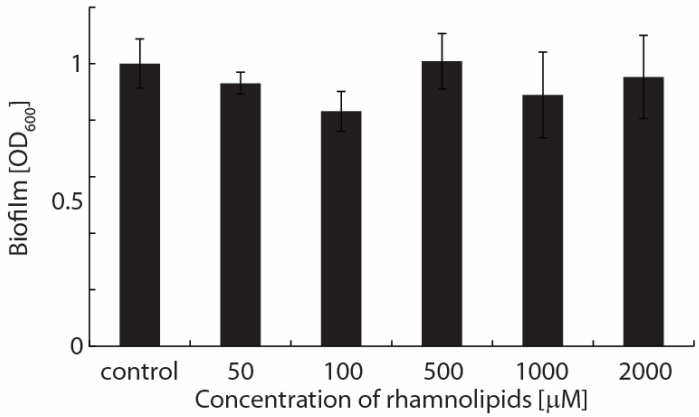

Fig. 20. **Crystal violet assay**. Amount of biofilm biomass measured by crystal violet assay of 24 h *E. coli* biofilms exposed to different concentrations of rhamnolipids.

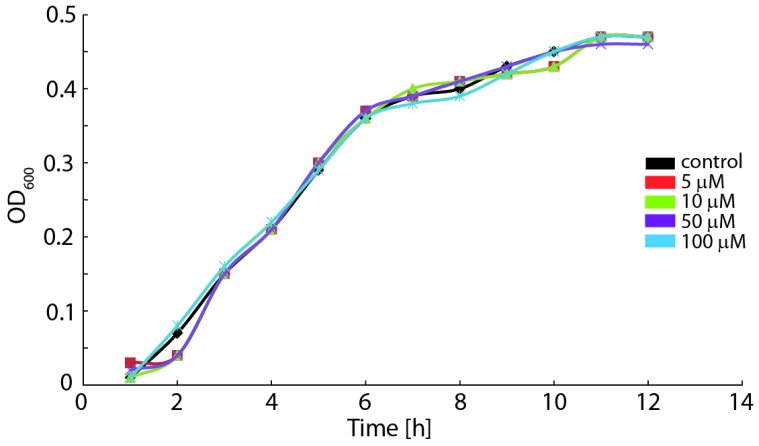

Fig 21. Growth curves of *E. coli* in shaking cultures in the presence of different concentrations of rhamnolipids.

The growth of *E. coli* planktonic cultures was similarly unaffected by expose to the DS of 3oxoC12HSL and rhamnolipids (Fig. 22). The concentration of 3oxoC12HSL and rhamnolipids measured in *P. aeruginosa* conditioned medium are 2.7 ¥ M and 3.0 mM, respectively.

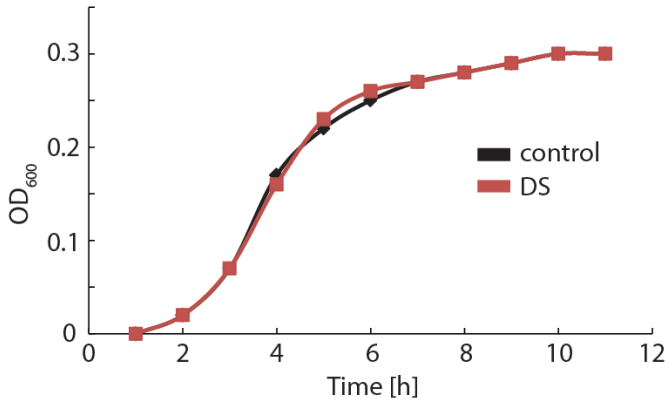

Fig. 22. Cell density of *E. coli* in shaking culture grown in the presence of of 50 µM 3oxoC12HSL and 50 µM rhamnolipids in LB media. Control is *E. coli* shaking culture in LB media.

Exposure of *E. coli* cells to either *P. aeruginosa* supernatant or the DS both resulted in the disappearance of c-di-GMP in the cytosol to undetectable levels (Fig. 23), suggesting an active dispersal mechanism. *E. coli* biofilms exposed to gentamicin, a transcription inhibiting

aminoglycoside antibiotic, along with the DS did not result in biofilm dispersal, providing further evidence that dispersal proceeds through a genetically regulated mechanism. (Fig. 24).

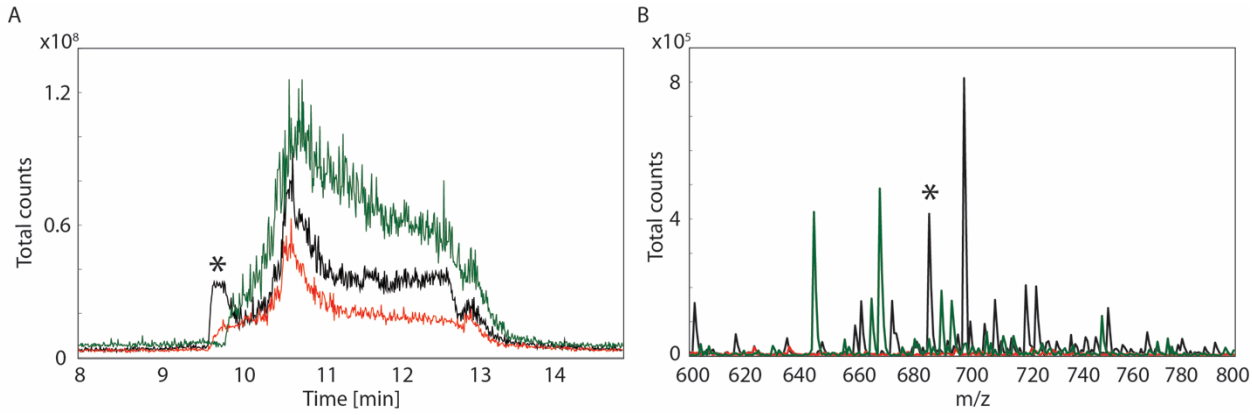

Fig 23. LC-MS detection of cyclic di- GMP (c-di-GMP) in *E. coli* cells exposed to PA14 supernatant and the dispersal solution (DS). The black, red and green traces in (A) and (B) correspond to *E. coli* cell extracts after exposure to PBS, PA14 culture supernatant, and the DS (50 µM 3oxoC12HSL and 50 µM rhamnolipids) respectively. (A) The LC chromatograph of the cell extracts shows the loss of the elution peak containing c-di-GMP in the cultures exposed to the supernatant and DS. (B) Mass spectra of the cell extracts showing the loss of the c-di-GMP peak in fractions from cultures exposed to supernatant and DS. The c-di-GMP peak in (A) and (B) (m/z 691) detected by LC-MS is denoted by *.

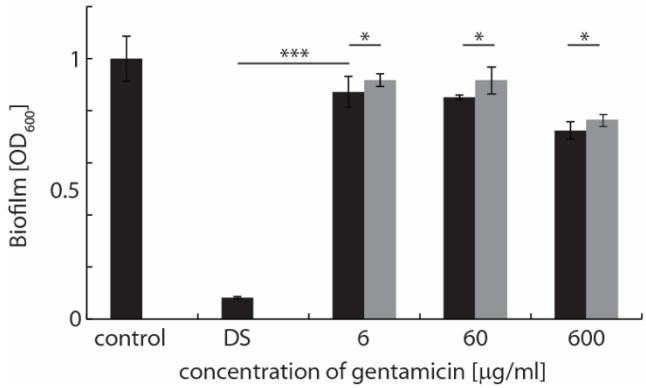

Fig. 24. Amount of biofilm biomass measured by crystal violet assay of 24 h *E. coli* biofilms exposed to DS, solution of DS and different concentration of gentamicin and solutions of different concentration of gentamicin alone for 6 h. Control is exposed to PBS. Black bars are *E. coli* biofilms exposed to solution of DS and different concentration of gentamicin and grey bars are *E. coli* biofilms exposed to different concentration of gentamicin alone. *** indicates $p <$ 0.001 and * indicates not significant difference.

3.3.3. Real-time observation of *E. coli* biofilm dispersal:

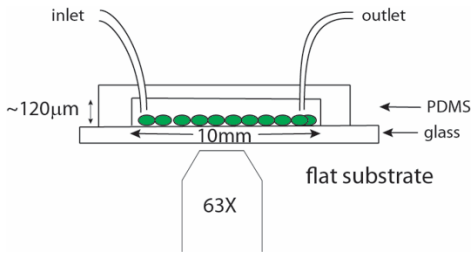

Fig 25. Schematic of single channel microfluidic device for imaging biofilm growth and dispersal.

A microfluidic growth chamber device was constructed to observe *E. coli* biofilm dispersal in real-time as described in chapter 2 (fig 25). Biofilms were grown by flowing medium through the channel for 24 h, followed by exposure to a flow of *P. aeruginosa* supernatant or the DS. Just as in the case of biofilms grown under static conditions, *E. coli* biofilms grown in the microfluidic devices dispersed in response to both the DS and the full *P. aeruginosa* culture supernatant (Fig. 19B & C). Biofilm biomass decreased over time after exposure to either the DS or *P. aeruginosa* culture supernatant. The complete dispersal of *E. coli* biofilms exposed to the DS took about 16 h, compared to about 10 h for dispersal by *P. aeruginosa* supernatant, but the extent of surface associated biomass reduction is similar. The vast majority of cells present in the latest time point panel of the confocal microscopy images in Fig. 19C are unattached and moving with the fluid flow of the device. The DS used in Fig. 19B and C was prepared using 100 µM rhamnolipids and 50 µM 3oxoC12HSL in pH 10 solution. Mass spectrometry analysis (data not shown) indicates that 3oxoC12HSL degrades in aqueous solution at room temperature on a time scale comparable to the flow cell experiment, and it is more stable at higher pH, hence the modified conditions compared to static biofilm dispersal. The *P. aeruginosa* stationary phase supernatant has an elevated pH of 8.0. Both DS of 50-50 and 100-50 µM rhamnolipids-3oxoC12HSL dispersed *E. coli* biofilms similarly, but the former formulation took longer to

reach full dispersal. Neither the TB (tryptone) nor the aqueous pH 10 buffer solution controls induce dispersal of *E. coli* biofilms.

3.3.4. The role of rhamnolipids in the diffusion of small molecules into *E. coli* cells:

While the above data suggested that rhamnolipids are a critical to the interspecies dispersal signaling pathway, the mechanism of activity of rhamnolipids was not yet understood. We hypothesized that rhamnolipids could increase the concentration of 3oxoC12HSL in the *E. coli* cells either by increasing the aqueous solubility of the relatively lipophilic 3oxoC12HSL or by increasing the permeability of 3oxoC12HSL through the *E. coli* cell membrane. The concentration of 3oxoC12HSL in aqueous solution, in which it is minimally soluble, was measured by LC-MS with different concentrations of 3oxoC12HSL mixed with 50 μM rhamnolipids. As shown in Fig. 26A, however, the relative concentrations of soluble 3oxoC12HSL are the same in aqueous solutions with or without rhamnolipids.

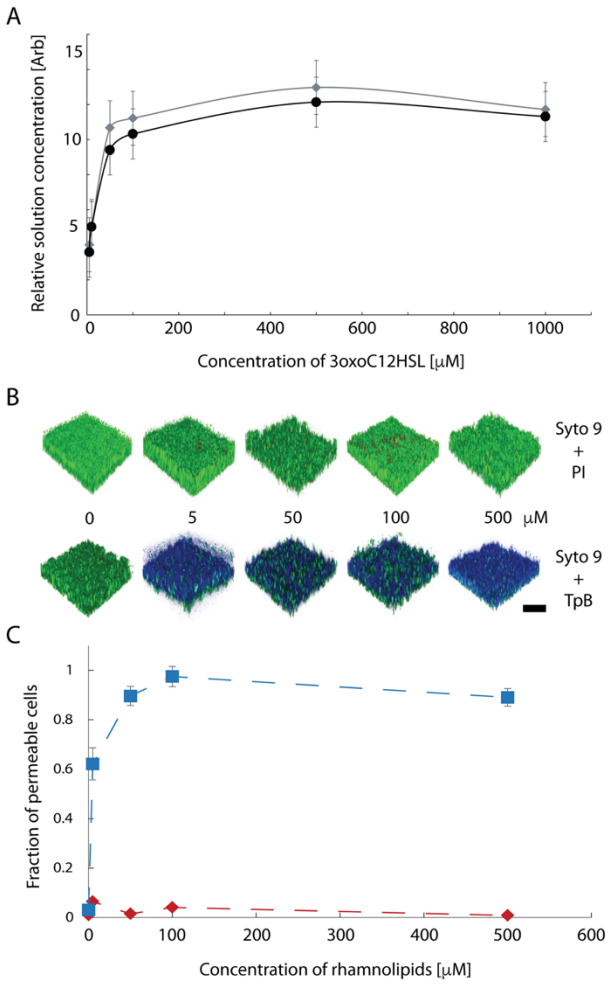

Fig. 26. Rhamnolipids induce selective permeability of *E. coli* membranes. A) Relative aqueous solubility of 3oxoC12HSL, assessed by LC-MS quantification of 3oxoC12HSL in aqueous solution (black circles) and an aqueous solution with 50μM rhamnolipids (grey diamonds). B) Rhamnolipid dose-dependent permeability of propidium iodide (PI) and trypan blue (TpB) in biofilm-associated *E. coli* cells, as shown by representative 3D confocal images. Biofilm cells were counterstained with SYTO 9. Scale bar is 20μm. C) Fraction of *E. coli* biofilm-associated cells permeable to PI and TpB at different concentrations of rhamnolipids quantified from confocal microscopy images.

To test whether rhamnolipids were altering *E. coli* membrane permeability, 24 h *E. coli* biofilms were exposed to different rhamnolipid concentrations and stained with propidium iodide (PI) or trypan blue (TpB) to assess the integrity of their cell membranes (Fig. 26B). While PI did not stain biofilm cells exposed to rhamnolipids, at any of the concentrations used, the permeation of TpB into biofilm cells increased significantly with rhamnolipid concentration (Fig. 26B & C).

Over 90% of cells within the biofilm were stained by TpB at rhamnolipid concentrations above 50 μM, while a negligible fraction of biofilm cells were stained by PI at rhamnolipid concentrations of up to 500 μM. These results suggest that rhamnolipids induce selective permeability of *E. coli* membrane towards certain small molecules, in this case TpB not PI.

LC-MS quantification of 3oxoC12HSL in the *E. coli* cell lysate was used to determine whether rhamnolipids increase the membrane permeability of this specific compound of interest in the dispersal signaling pathway. Cells incubated in aqueous solutions of 3oxoC12HSL with and without rhamnolipids show a monotonic increase in the relative concentration of 3oxoC12HSL in the cell lysate with time of incubation (Fig. 27A). In cells exposed to 3oxoC12HSL and rhamnolipids for 60 min, there was a 2.7-fold increase in the concentration of 3oxoC12HSL in the cell lysate compared to cells exposed to only 3oxoC12HSL.

3.3.5. Rhamnolipids alter the *E. coli* membrane composition and permeability to lipophilic AHLs:

I hypothesized that rhamnolipids alter the membrane permeability of *E. coli* cells by removing outer cell membrane lipopolysaccharide (LPS). The outer membrane LPS content of a cell or a solution can be measured using a previously developed purplad assay,[139] which quantifies the solution concentration of inner core LPS components Kdo/Hep. The increase in the amount of Kdo/Hep in solution over time indicates that LPS is being released into the supernatant.[140] The amount of LPS released from *E. coli* cells in the supernatant extract of *E. coli* cultures when exposed to rhamnolipids increased with the concentration of rhamnolipids to about 14% over background levels at 100 μM rhamnolipids (Fig. 27B). The impact of such changes in LPS content of the membranes on compound permeation was assessed by measuring 3oxoC12HSL

concentrations in *E. coli* WT and outer membrane LPS deletion mutants Δ*waaR* and Δ*waaG*, which produce truncated oligosaccharide components of LPS (Fig. 14C). The relative concentration of 3oxoC12HSL in the cell lysates of these mutants is less sensitive to the presence of rhamnolipids than the WT strain. In the case of the Δ*waaG* mutant, having the greatest LPS truncation, there is no significant difference between the levels of 3oxoC12HSL in cells incubated with or without rhamnolipids.

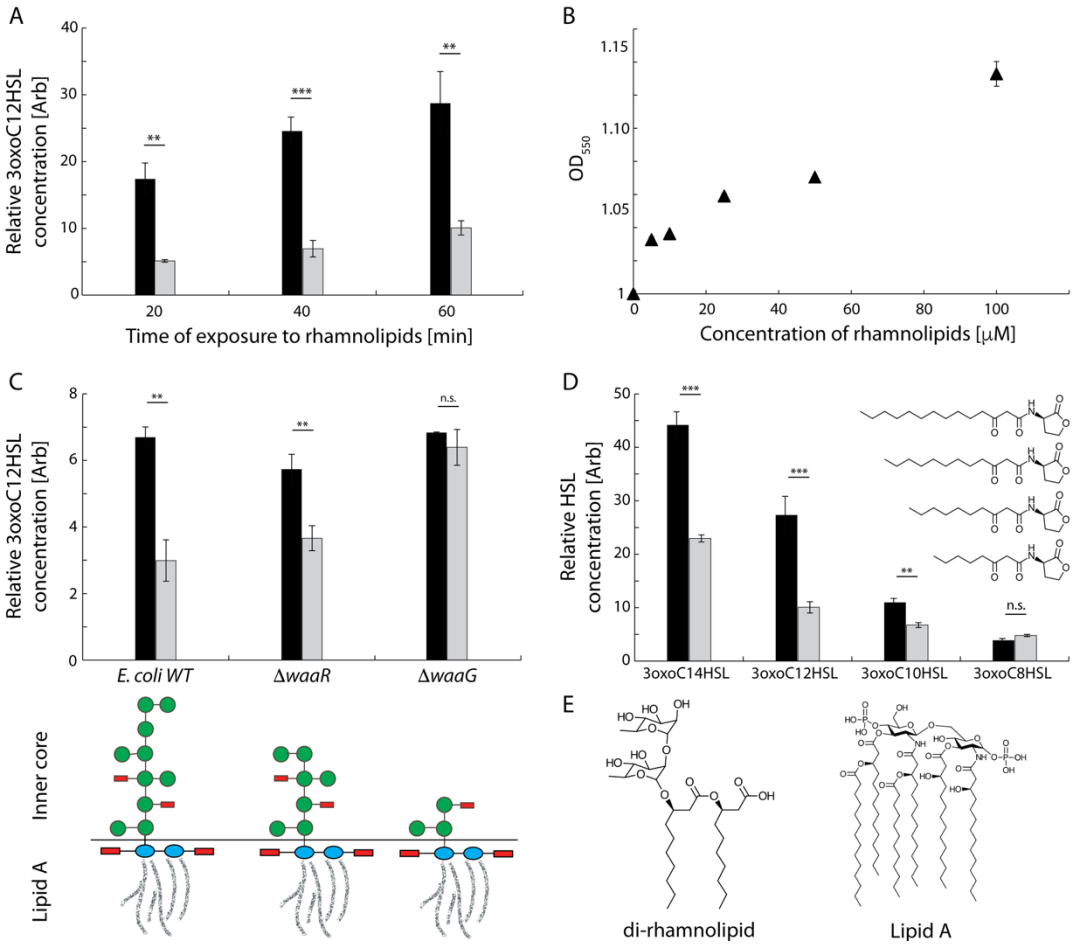

Fig. 27. Rhamnolipids increase the permeability of 3oxoC12HSL and lipophilic AHLs through *E. coli* cell membranes. A) Time-dependent relative concentrations of 3oxoC12HSL in *E. coli* cells exposed to aqueous solutions of 50μM 3oxoC12HSL with (black) and without (grey) 50μM rhamnolipids, quantified by LC-MS. B) Relative amounts of LPS removed from planktonic *E. coli* cells exposed to different concentrations of purified rhamnolipids, determined by the purpald assay. C) Relative concentrations of 3oxoC12HSL in *E. coli WT* and LPS deletion

mutants cells after exposure to solutions of 50 μM 3oxoC12HSL with (black) and without (grey) 50 μM rhamnolipids, quantified by LC-MS. The schematic below the strain labels shows the expected lipid A and inner core oligosaccharide truncations, or lack thereof, due to the corresponding ligase knockouts. Glucosamine in the lipid A domain is show as blue ellipses, attached to the lipid A acyl chains, in grey. Phosphate groups are shown in red and various sugars in the inner core are represented by green circles. D) Acyl chain length dependence of relative AHL concentration in *E. coli* cells exposed to solutions of 50μM AHLs with (black) and without (grey) rhamnolipids. E) The chemical structure of C10-C10 di-rhamnolipid, the dominant congener isolated from *P. aeruginosa* supernatant, and lipid A. ** and *** indicate $p <$ 0.01 and 0.001 respectively; n.s., difference was not significant.

While only 3oxoC12HSL and C4HSL are produced by *P. aeruginosa*, I hypothesized that the selective permeability induced in *E. coli* membranes by rhamnolipids may be general to other lipophilic AHLs. Lipophilic AHLs, like 3oxoC14HSL (N-(3-oxo-tetradecanoyl) homoserine lactone) and 3oxoC12HSL, exhibit pronounced differential membrane permeabilities in cells incubated with and without rhamnolipids. More hydrophilic AHLs, such as 3oxoC10HSL (N-(3-oxo-decanoyl) homoserine lactone) and 3oxoC8HSL (N-(3-oxo-octanoyl) homoserine lactone), on the other hand, exhibit smaller or no significant differences, respectively, in membrane permeability with and without rhamnolipids (Fig. 27D). The difference in relative cytosolic concentrations of these AHLs decreases with acyl chain length.

3.4. Discussion

Small molecule signaling factors that induce auto-dispersal or trigger dispersal by inter-species communication represent a promising strategy for biofilm treatment. Several such compounds have been identified in intra-[118–120,141] and interspecies[123] dispersal signaling. The dispersal of *E. coli* biofilms by *P. aeruginosa* appears to be an interesting addition to the above sets of cell-cell communications that induce biofilm dispersal. As the dispersal data in Fig. 14B & C show, a variety of *E. coli* strains, both commensal and pathogenic, are sensitive to diffusible compounds

in the *P. aeruginosa* supernatant. The reduction in biomass observed for *E. coli* biofilms in response to *P. aeruginosa* spent medium appears to be the result of dispersal and killing of *E. coli* from biofilms (Fig. 14 & 16). Moreover, we have isolated two compounds in the *P. aeruginosa* supernatant that work cooperatively to trigger the dispersal response in *E. coli* biofilms (Fig. 19 & 23). This antagonistic interspecies dispersal signaling pathway may explain why *E. coli* and *P. aeruginosa* are generally not found in coculture biofilms in medical, industrial, or natural environments.

The knockout mutants used to provide clues about the active components of the supernatant suggest compounds resulting from the main *P. aeruginosa* QS systems, Las and Rhl (Fig. 17A) are predominantly responsible for dispersal signaling. 3oxoC12HSL and C4HSL, biosynthetic products of *lasI* and *rhlI*, respectively, inhibit biofilm development in *E. coli*.[142] Upon exposure to 3oxoC12HSL (Fig. 17B) *E. coli* biofilms dispersed to a significant extent but not as completely as those exposed to the full supernatant. The addition of rhamnolipids, a product of *rhlAB* expression, to the 3oxoC12HSL resulted in the full dispersal of *E. coli* biofilms (Fig. 19A). Consistent with this observation, the Δ*rhlA* strain culture supernatant was significantly limited in its ability to reduce the biomass of *E. coli* biofilms compared to the WT supernatant. C4HSL, a product of *rhlI* expression, showed no dispersal activity, even in the presence of rhamnolipids, and the Δ*rhlI* strain culture supernatant dispersed *E. coli* biofilms similarly to that of the WT strain. I propose, therefore, that 3oxoC12HSL and rhamnolipids, produced by the *P. aeruginosa* main QS pathways, act cooperatively to activate a dispersal response in *E. coli*.

Rhamnolipid biosynthesis, mediated by RhlA and RhlB, is under the regulation of RhlI/R,[130,132] but the Δ*rhlI* strain supernatant had the same biomass reduction effect on *E. coli* biofilms as the WT supernatant (Fig. 17A). LC-MS analysis showed that the Δ*rhlI* strain produced rhamnolipids despite the previously reported promoting effect of RhlR- C4HSL suggesting that RhlR alone is a leaky repressor of *rhlAB*. The biosynthesis of rhamnolipids in the Δ*rhlI* strain is consistent with previous findings that *rhlAB* expression is only partially suppressed in the absence of C4HSL[130] and the observed effects of the Δ*rhlI* strain supernatant on *E. coli* biofilm dispersal. Indeed, RhlR, in the absence of C4HSL – as is the case for the *rhlI* knockout – only partially represses *rhlAB* expression, while *rhlAB* expression is promoted by LasR-3oxoC12HSL binding which should still occur in the Δ*rhlI* strain.[130,143] The ability of the *rhlI* mutant to reduce *E. coli* biofilm biomass is consistent, therefore, with our proposed dispersal signaling mechanism.

Rhamnolipids alone do not have any cytotoxic, growth inhibition, or biofilm dispersal activity towards *E. coli* (Fig. 20 & 21), and we are currently unaware of any known specific receptors for rhamnolipids in *E. coli*. It seems likely, therefore, that 3oxoC12HSL is the active compound triggering dispersal signaling, but the identity of the receptor for this compound in *E. coli* is unclear. Nevertheless, the downstream effect of *E. coli* exposure to both the *P. aeruginosa* culture supernatant and the DS is an observed decrease of the c-di-GMP signal in the mass spectrum to undetectable levels (Fig. 23), consistent with signal mediated c-di-GMP hydrolysis shown elsewhere.[144,145] C-di-GMP is a ubiquitous regulator of the sessile-to-planktonic lifestyle change.[146] Consequently, our results suggest that, regardless of the receptor identity, 3oxoC12HSL triggers dispersal in *E. coli* through the differential regulation of a c-di-GMP synthesis or degradation pathway.[147,148] The retention of biofilm biomass when the DS is

administered in the presence of a transcription inhibiting antibiotic (Fig. 24) further supports a genetically regulated process mediating dispersal, rather than a physical dispersal process.

While 3oxoC12HSL appears to have a specific biological effect, the mechanism of activity of rhamnolipids in *E. coli* biofilm dispersal signaling remained a mystery. I hypothesized that rhamnolipids act through a physical mechanism by which they enhance the ability of 3oxoC12HSL to trigger dispersal. Rhamnolipids exhibit a range of physical behavior in other species, from cytotoxicity to aiding twitching motility to dispersing biofilms,[137] but there is no precedent, to our knowledge, of their activity in a specific signaling pathway. In mediating the dispersal of *E. coli* biofilms in response to 3oxoC12HSL, rhamnolipids may have two mechanisms by which to increase the effective concentration of the signaling compound in the target cells: first, by increasing the aqueous solubility of 3oxoC12HSL, which is relatively lipophilic, and second, by increasing the permeability of the target cell membrane to 3oxoC12HSL. The solubility data in Fig. 26A suggest the former mechanism is not the functional one. The sensitivity of TpB permeability through *E. coli* membranes into the cytoplasm of the cell to rhamnolipid concentration, and the striking contrast of these data with the insensitivity of PI permeability to rhamnolipid exposure (Fig. 27B & C), indicate that rhamnolipids significantly and selectively alter the permeability of *E. coli* membranes to some molecules but not others.

Rhamnolipids induce selective permeability of *E. coli* membranes towards AHLs as well. *E. coli* cells were differentially permeable to 3oxoC12HSL when incubated with or without rhamnolipids (Fig. 27A). One plausible mechanism by which rhamnolipids might exhibit such activity is by the removal of LPS from the outer membrane of the target cells. Rhamnolipids remove LPS from the outer membrane *P. aeruginosa* cells, rendering the cell surface more

hydrophobic and facilitating the uptake of lipophilic carbon substrates.[140] I hypothesized that the removal of LPS from *E. coli* outer membranes by rhamnolipids might have similar effects on the permeability of lipophilic compounds, like 3oxoC12HSL. Our data show that rhamnolipids indeed remove LPS from *E. coli* membranes (Fig. 27B), even at concentrations below their critical micelle concentration.[141] *E. coli* knockout mutants lacking ligases for full LPS outer core biosynthesis exhibited a diminished effect of rhamnolipids on 3oxoC12HSL permeability that was consistent with greater polysaccharide truncation (Fig. 27C). The removal of LPS from the *E. coli* outer membrane by rhamnolipids may increase the permeability of 3oxoC12HSL by decreasing the density of hydrophilic sugars in the cell membrane. This mechanism is further supported by the fact that more lipophilic AHLs have greater membrane permeability in the presence of rhamnolipids than solutions with only the AHL, as compared to shorter acyl chain, more hydrophilic AHLs (Fig. 27D). The membrane permeability of the 3oxoC10HSL and 3oxoC8HSL show little to no sensitivity to the presence of rhamnolipids. The mechanism of removal of LPS by rhamnolipids has not been studied. The similar arrangement of di-pyranose sugars and associated 3-oxo-alkanoate chains (Fig. 27E) may form the basis for the stabilization of lipid A, the membrane-bound base of LPS, by rhamnolipids in solution. Alternatively, interactions between the 3-oxo-alkanoates of rhamnolipids and AHLs (Fig. 27D) could serve as the chemical basis for increased concurrent diffusion through the LPS layer on the *E. coli* outer membrane. Either of the above interaction is consistent with the effect of rhamnolipids increasing the selective membrane permeability of *E. coli* membranes to lipophilic AHLs, but this mechanism is not mutually exclusive with other mechanisms of surface activity, such as rhamnolipid insertion into the outer membrane. Ongoing studies are investigating other plausible

biophysical mechanisms by which rhamnolipids might be involved in this interspecies signaling pathway.

3.5. Conclusion

In this work, I demonstrate a new dispersal signaling pathway between *E. coli* and *P. aeruginosa* mediated by *P. aeruginosa*-derived 3oxoC12HSL and rhamnolipids. Rhamnolipids play a cooperative role in the signaling mechanism by enhancing the permeability of *E. coli* cell membranes to 3oxoC12HSL. More generally, I also demonstrate that rhamnolipids induce selective membrane permeability in *E. coli* and do so, particularly for long acyl chain AHLs. The mechanism by which rhamnolipids modify the target cell membrane is not determined conclusively but is consistent with the removal of outer membrane LPS. My results establish the role of rhamnolipids as a cooperative, biophysically active component of an interspecies signaling pathway. Many microorganisms rely on signaling via diffusible AHL compounds, and rhamnolipids may serve to generally modulate the sensitivity of cells to these and other chemical signals. By altering membrane permeability, rhamnolipids can potentially enhance the uptake of lipophilic bactericidal compounds as well, increasing the susceptibility of biofilms towards them. Further studies of the general membrane activity of rhamnolipids could lead to development of novel therapies to combat biofilm infections. Elucidating new mechanisms of small molecule interactions within and between microbial communities is instrumental to understanding their behavior and may lead to new strategies for anti-biofilm treatments.

Chapter 4.

Effects of Growth Surface Topography on Bacterial Signaling in Coculture Biofilms

4.1. Introduction

In the previous chapter, I described a dispersal signaling pathway in *Escherichia coli* triggered by *Pseudomonas aeruginosa* quorum sensing (QS) compounds. The study in the current chapter will demonstrate switching of this dispersal signaling pathway, by changing the structure and morphology of the *E. coli* biofilms using physical cues. Biofilms represent an ideal system in which to study structure-function relationships in bacterial communities. Gradients of oxygen, nutrients, and signaling molecules, among many other compounds, determine structure and function in biofilms.[114] In multi-species biofilms, morphology, species segregation, and organization affect these gradients and thus community function. These architectural features modulate global fluxes of compounds in and out of the biofilm as well as the exchange rates of signaling factors and metabolites between species.

The ability to engineer the structure and function of bacterial biofilms represents an important scientific and technological goal. In medical settings, opportunistic pathogens are responsible for persistent biofilm infections, which resist conventional antibiotic treatment.[149,150] These infections are widespread, expensive to treat, and deadly.[1,151,152] Preventing the formation of such biofilms, or increasing biofilm susceptibility to antibiotics, would reduce healthcare costs, and morbidity and mortality. On the other hand, biofilms with specific metabolic function play critical roles in a variety of helpful contexts, such as communities in the human gut,[153] environmental remediation,[154] and bioenergy applications.[154–156] Therefore, understanding the

interactions between species that determine structure-function relationships has become a topic of intense interest for both detrimental and beneficial bacterial communities.[157–160]

Environmental factors, including signaling and metabolic interactions, determine the structure and composition of multispecies communities [157,161] as well as the evolution of social interactions.[45,157,162] Consequently, controlling spatial organization of species within bacterial communities represents a useful tool to elucidate chemical interactions within [163–167] or between species [168–170] and to deterministically alter their function.[170–172] In this chapter, I demonstrate that growth surface topographical features can play a significant role in determining interspecies interactions in a growing coculture of commensal *Escherichia coli* and opportunistically pathogenic *Pseudomonas aeruginosa*. These two species exhibit a competitive relationship in the context of biofilm growth, whereby *P. aeruginosa* produces chemical signaling compounds that disperse *E. coli* biofilms.[173] Changes in the dimensions of micro-scale post features on biofilm growth surfaces deterministically controlled biofilm species composition, structure, and properties. I further identified a molecular mechanism determining coculture biofilm architecture and demonstrated surfaces that can select for desirable community behavior exemplified by antibiotic susceptibility and persistent resistance to pathogen colonization. These results show that physical features on growth substrate surfaces can be used to engineer biofilm formation to exclude detrimental bacteria and promote beneficial bacterial function.

4.2. Materials and methods

4.2.1 Bacterial strains and planktonic culture conditions:

The bacterial strains used in this study are listed in the table A.1. The isogenic mutant in *E. coli* strain MC4100 carrying a deletion in *tnaA* was constructed using the lambda red recombinase

system,[174] with the help of Dr. Martina Sassone-Corsi. All cell culture materials were obtained from Fisher Scientific unless otherwise noted. All bacterial strains were streaked on Lysogeny broth (LB) 1.5% agar plates from frozen glycerol stocks and grown overnight at 37˚ C. Shaking cultures were inoculated from isolated plate colonies into 2 ml of liquid LB and grown at 37˚ C on an orbital shaker at 250 rpm for 6 h.

4.2.2. Microfabrication of Si wafer masters:

Details of microfabrication methods and subsequent processes used have been described previously [175]. Si wafers were vapor primed with hexamethyldisilazane (HMDS) to improve photo resist adhesion. SPR700 was used as an i-line resist and a Nikon 5x stepper was used to expose the coated wafers followed by post exposure bake and resist development using Microposit MF CD26. Descumming was performed prior to Bosch advanced silicon etch [176] in an STS deep reactive ion-etching (DRIE) tool. C_4F_8 and SF_6 chemistry was used for Si etching. A Veeco profilometer and cross sectional (Zeiss) SEM were used to characterize and optimize exposure conditions, etch rates and etch profiles. The Si wafers were given a final overcoat of C_4F_8 to aid in any subsequent replication process.

4.2.3. Patterned growth surface fabrication:

Biofilm growth surfaces for this study were polymer replicas of microfabricated <100> Si wafer masters with posts of 800 nm diameter in a hexagonal array and heights varied from 1.1 to 11 μm. Polymer surfaces for biofilm growth were fabricated using UV curable Norland Optical Adhesive (NOA 61) polyurethane-based resin, as described previously.[177] Polydimethylsiloxane (PDMS) prepolymer and a crosslinking agent (Dow Corning Sylgard 184) were cured on the Si masters. The resulting PDMS mold was peeled off the silicon master, and NOA 61 was poured into the mold, backed with a fluorosilane-functionalized glass slide, and cured under UV flood

illumination (mercury vapor bulb, 100W, Sylvania) for 60 min. The resulting polymer replicas of the Si masters were peeled out of the PDMS and used as growth surfaces in biofilm experiments. The molds were reused for further replica fabrication. The images of the patterned polymer surfaces were acquired using an FEI quanta 3D scanning electron microscope (SEM). Surfaces were freeze fractured and sputtered with iridium to reduce charging during SEM imaging.

4.2.4. Biofilm growth conditions:

All biofilms were cultured in tryptone medium consisting of 10 g/l bacto tryptone in 6 well plates or microfluidic devices at 22˚ C. Shaking cultures were grown in LB and diluted 1000x in tryptone from 6 h log phase cultures before surface inoculation. Biofilms in 6 well plates were grown on 18 x 18 mm glass cover slips or polymer surfaces and imaged using confocal microscopy. Biofilms for antibiotic susceptibility tests were grown in tryptone medium supplemented with 3 g/l NaCl to avoid media induced stress on cells for live-dead staining.[178]

For all experiments, *E. coli* MC4100 and *P. aeruginosa* PA14 strain backgrounds were used. *E. coli yfp* (MC4100 *yfp*) and *P. aeruginosa* PA14 *rfp* constitutively fluorescing strains were used for the coculture experiments in Fig. 28, 34, 38, and 39. For 6-well plate static coculture growth experiments, biofilm growth was separated into two stages, unless noted otherwise: one species was inoculated first and allowed to grow for 24 h. The spent medium and planktonic cells were then aspirated and the mature biofilms were rinsed with PBS and inoculated with the second species in tryptone medium and allowed to grow for 24 h more. Cocultures of *E. coli* and *P. aeruginosa* for Fig. 28c were inoculated at the same time and grown for 24 h.

4.2.5. Measurement of biofilm dispersal:

E. coli biofilms grown on submerged surfaces in tryptone medium for 24 h in 6 well plates were exposed to *P. aeruginosa* (PA14 WT) supernatant. The supernatant was prepared by diluting *P. aeruginosa* shaking cultures 1000x in tryptone medium and growing for 15 h at 37 ˚C on an orbital shaker at 250 rpm. Cultures were then centrifuged at 15000 x *g* and the resulting supernatant was passed through a 0.2 μm PES vacuum filter. For dispersal experiments on 6 well plates, biofilms were exposed to the supernatant for 6 h. The amount of biofilm-associated biomass was quantified by a crystal violet (CV) assay. Biofilms were rinsed in PBS and then incubated for 15 min at room temperature in 2 ml of 0.1% aqueous CV. The stained wells were rinsed with PBS and growth surfaces were transferred to another clean well to quantify biomass accumulated on the surfaces only. 2 ml of ethanol was added to the clean wells and incubated for 5 min at room temperature. The optical density of the dissolved CV in ethanol was obtained at 600 nm (OD_{600}) and measured using a Biowave CO8000 cell density meter. All absorbance values were obtained from triplicate or greater number of samples and normalized to a self-consistent control within each experiment.

4.2.6. Growth of biofilms in microfluidic devices:

For growth in microfluidic devices with flat and post surfaces, *E. coli yfp* or *P. aeruginosa rfp* shaking cultures were diluted 1000x in tryptone medium and seeded for 4 h in the channel with no flow. Sterile tryptone medium was then exchanged for the inoculum and flowed at a rate of 10 ❢ l/h through the channel for 24 h to grow mature biofilms. To introduce *P. aeruginosa* cells into

the microfluidic device with *E. coli* biofilms, the sterile tryptone medium supply was inoculated with *P. aeruginosa* PA14 *rfp* cells at an optical density (OD) of 0.02. To maintain a consistent concentration of *P. aeruginosa* in the channel, the inoculum was periodically re-diluted with sterile tryptone medium to OD 0.02 when the cell density of the inoculum reached OD 0.36. Time series images of biofilms in the microfluidic devices were obtained with a 20X air objective. At least three images were acquired along the channel every hour. The images were obtained with a z interval of 9 μm. All other settings were kept the same as described below.

4.2.7. Finite element analysis:

COMSOL Multiphysics software was used to analyze indole diffusion in *E. coli* biofilms. The *E. coli* 24 h biofilms on plain and polymer surfaces were imaged using 2 photon microscopy and the 2D images were imported to SCAN IP module of the Simpleware software. After 3D reconstruction of the 2D images, they were meshed and exported as COMSOL files and analyzed for indole diffusion using CFD module (The transport of diluted species) of the COMSOL Multiphysics 4.3b software. Indole was assumed to be stable and not degrading in this model and the out-diffusion of indole was only through the surface of the biofilm. The sides and the bottom of the biofilm were set as non-diffusing boundaries. The diffusion coefficient of indole in water and biofilm was assumed to be 8e-10 m^2s^{-1} and 4e-10 m^2s^{-1}, respectively, based on the measured diffusion coefficient of indole in water (7.8e-10 m^2s^{-1}) [179] and the measured diffusion coefficient of phenol in biofilms (4e-10 m^2s^{-1}).[180] Phenol has a molar mass and aqueous solubility similar to indole, as well as a similar aqueous diffusion constant. The indole generation rate was 0.01 $mol \cdot m^{-3}s^{-1}$, which was determined by trial and error to match previous accumulated indole concentration measurements,[181–183] though the relevance to this study is captured in the relative

concentrations across different biofilm morphologies rather than the absolute concentration. The steady flux and concentration values were obtained by COMSOL finite element analysis.

4.2.8. *tnaA* deletion mutatnt construction:

Primers (TTTGCGGTGAAGTGACGCAATACTTTCGGTTCGTACGTAAGT-GTAGGCTGGAGCTGCTTC and TGGAAAACTTTAAACATCTCCCTGAACCGTTCCGCA-TTCGCATATGAATATCCTCCTTA) homologous to sequences within the 5′ and 3′ ends of the target regions were designed and were used to replace the C-terminal region with a nonpolar kanamycin resistance cassette derived from plasmid pKD4, respectively [174]. Kanamycin was used for selection of the deletion construct. The resulting strain was termed MC4100 Δ*tnaA*. To verify whether the kanamycin resistance cassette recombined within the target gene site, primers that flank target sequence were designed (GTTGCCGCCTGAGGAGAT and CCATCACCAGAGCCAAACC). Both wild-type and mutant gene sequences were amplified with genomic confirmation primers by PCR using Phusion High Fidelity DNA polymerase (New England Biolabs). Triplicate PCR runs were used to confirm the gene deletion.

4.2.9. Confocal microscopy biofilm sample preparation:

Static biofilms of constitutively fluorescing strains in 6 well plates were prepared for imaging by washing in PBS and air-drying for approximately 8 min until only a thin film of water was left on the surface. All other static biofilms in 6 well plates were washed in PBS and incubated in 5% formaldehyde for at least 1 h and air-dried as above. Substrates prepared by either method were

then immersed in 0.1% agarose solution in water and set on the benchtop until the agarose solidified. Embedded biofilms were stored in PBS until imaging.

4.2.10. Confocal scanning laser microscopy (CLSM) imaging:

All confocal images of statically grown biofilms were obtained using a Zeiss LSM780 inverted confocal microscope with 63X water immersion objective. Dichroic beam splitters were used to filter laser lines at 488 and 561 nm. YFP and RFP expressing biofilms were excited with 488 nm and 561 nm laser lines, respectively. Emission intensity was collected from YFP and RFP at 493-596 and 596-718 nm, respectively. The same laser settings were used for SYTO 9 and propidium iodide (PI) imaging. In case of the live-dead assay images, the blue and yellow colors were assigned to the channels using ImageJ software after image acquisition to avoid confusion with the YFP and RFP colors in the coculture images. Both color channels were imaged using alternating line averaging to avoid blurring of the image due to drifting. These adjustments reduced fluorescence cross-talk to undetectable level in two-color imaging experiments. Confocal images were obtained with a z interval of 1 μm and a pinhole size of 1 airy unit.

Two-photon images of biofilms were similarly acquired. The main dichroic beam splitter was used to reflect laser lines beyond 760 nm. YFP was excited using a titanium-sapphire laser at 800 nm wavelength of light. The z intervals were adjusted to 2 μm and the pinhole was set to the maximum.

4.2.11. Antibiotic resistance assays:

Biofilms were grown in tryptone medium supplemented with NaCl to reduce membrane stress [178]. Biofilms were grown for 24 h and washed with PBS, then incubated in either PBS or 1 mM rifampicin in PBS for 3 h. The biofilms were then washed again with PBS and stained with 5 μM SYTO 9 and 5 μM propidium iodide (PI, Life Technologies) in PBS for 20 min. Biofilms were then washed with PBS and embedded in agarose for imaging by confocal microscopy.

4.2.12. Dynamic biofilm imaging:

Microfluidic flow channel devices incorporating glass or patterned polymer substrates were used to image biofilm development in real-time. Microfluidic devices with channel dimensions 10 x 1 x 0.12 mm were fabricated using PDMS channels and glass or polymer growth surfaces, as shown in Fig. S7. Flow channels were molded by curing PDMS on lithographically defined SU-8 patterns. For glass growth surfaces the PDMS was bonded to glass by plasma cleaning both the surfaces. For structured polymer growth surfaces a thin channel was cut into a ~120 μm PDMS film mold of the SU-8 mold and bonded to a coverglass by plasma cleaning. Holes for fluid access were cut in the polyurethane substrate using a laser cutter. The polyurethane substrate was functionalized with APTMS [184] and bonded to the PDMS gasket to seal the channel. Small PDMS blocks were similarly bonded to the flat back of the polymer substrates to seal the fluid inlet and outlet.

4.2.13. Image analysis:

The 3D coculture and live-dead assay images were reconstructed using Volocity and ImageJ plugin "3D viewer". The amount of biomass was quantified using the "select objects" of the

intensity images from each channel using Volocity after deconvoluting the images by applying the point spread function to each channel. 2D surface maps were created using the ImageJ plugin "extended depth of field". Surface roughness of the biofilm was measured using 'SurfCharJ' pluggin in Image J [185]. The images for roughness analysis used were obtained from *E. coli yfp* biofilms using two-photon imaging.

4.3. Results.

4.3.1. Growth of coculture biofilms on microstructured surfaces

To study their interactions in various microenvironments, coculture biofilms of *E. coli* and *P. aeruginosa* were grown on submerged surfaces. Growth surfaces were flat or structured with a hexagonal array of mesoscale posts (Fig. 28a) fabricated by a fast polymer replication method. Three types of biofilms were grown: (*i*) inoculation and growth of mature *P. aeruginosa* biofilms followed by inoculation with planktonic *E. coli*, (*ii*) inoculation and growth of mature *E. coli* biofilms followed by inoculation with planktonic *P. aeruginosa*, and (*iii*) concurrent inoculation and growth of both species on the same substrate surface. *E. coli* and *P. aeruginosa* strains constitutively expressing yellow (*yfp*, shown as green) and red (*rfp*) fluorescent proteins, respectively, were used unless otherwise noted to facilitate static and dynamic imaging of species content and segregation within coculture biofilms. Inoculation of flat surfaces resulted in surface colonization by *P. aeruginosa* biofilms in all cases, as did inoculation of structured surfaces when either *P. aeruginosa* biofilms were grown first (Fig. 28b) or when both species were inoculated at the same time (Fig. 28c). But when *E. coli* biofilms were grown first, followed by inoculation with *P. aeruginosa*, the resulting coculture biofilms exhibited surface topography-dependent morphology and species content (Fig. 28d). As surface topography varied from flat to

short posts to tall posts, the biofilms featured increasing volume fractions of *E. coli* cells (Fig. 28e). In biofilms grown on 11 μm tall posts, the resulting community was composed almost exclusively of *E. coli* cells. To understand the mechanism by which surface features modified these interactions, I investigated the role of interspecies chemical communication in this system.

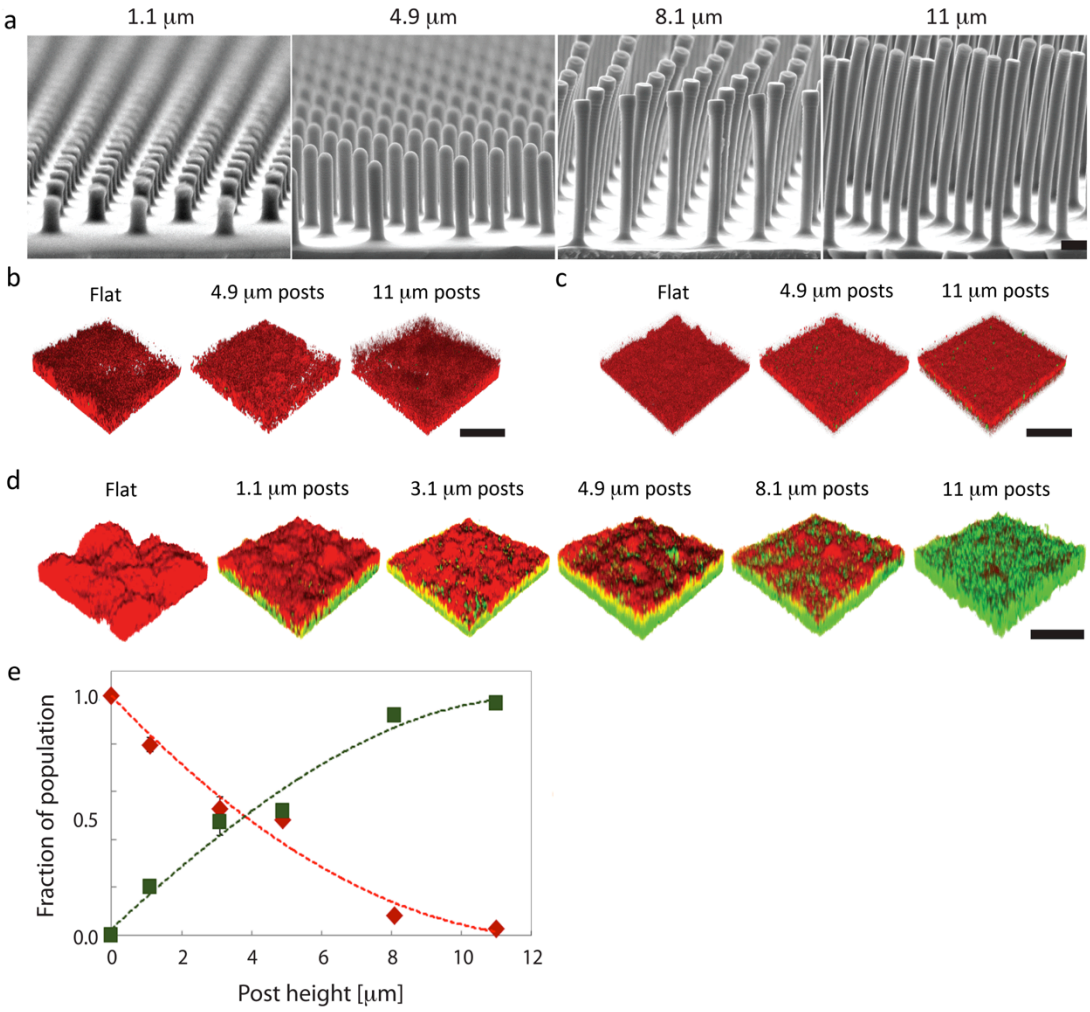

Figure 28. Control of multispecies biofilm morphology and species content using surface topography. (a) SEM images of mesoscale patterned polymer surfaces of various post heights. 3D confocal images of coculture biofilms were obtained of *E. coli yfp* and *P. aeruginosa rfp* constitutively fluorescing strains (green and red colors indicate *E. coli* and *P. aeruginosa*, respectively) for: (b) 24 h *P. aeruginosa* biofilms grown on various post heights then inoculated with *E. coli* for an additional 24 h; (c) 24 h *E. coli* and *P. aeruginosa* co-inoculated biofilms on various post heights; (d) 24 h *E. coli* biofilms grown on various post heights then inoculated with *P. aeruginosa* for an additional 24 h. (e) Fraction of *E. coli* and *P. aeruginosa* cells of the total biofilm cell content as a function of post height from inoculation conditions in (d). Green squares

and red diamonds indicate fraction of *E. coli* and *P. aeruginosa* cells, respectively. Scale bars are 1 μm in (a) and 20 μm in (b)-(d).

4.3.2. Effect of substrate surface microenvironment on the resistance of *E. coli* biofilms to *P. aeruginosa* induced dispersal

P. aeruginosa produces compounds that disperse *E. coli* biofilms via and active, biologically-regulated response.[173] To test whether *P. aeruginosa* was dispersing *E. coli* biofilms in this system, *E. coli* biofilms were exposed to the cell-free supernatant of planktonic *P. aeruginosa* cultures. Exposed *E. coli* biofilms were completely disrupted when grown on flat surfaces (Fig. 29a). When grown on post surfaces, they were resistant to dispersal, as indicated by significant increases in biofilm biomass on post surfaces (Fig. 29b). The resistance to dispersal increased with growth surface post height.

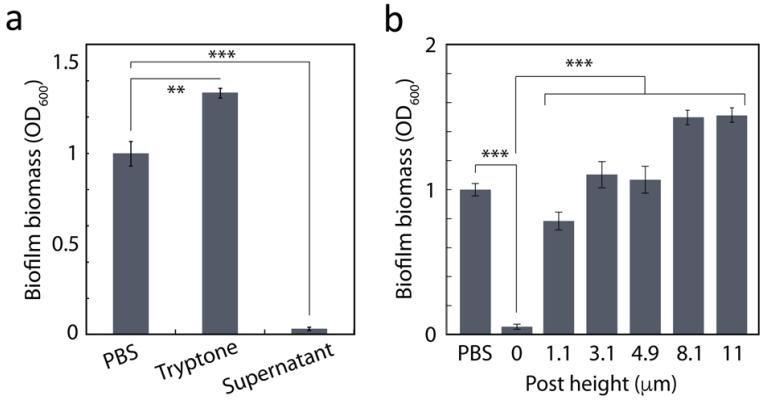

Figure 29. Growth surface topography inhibits the dispersal of *E. coli* biofilms in response to *P. aeruginosa* culture supernatant. (a) Crystal violet assay of 24 hour grown *E. coli* biofilms exposed to PBS, tryptone medium, or *P. aeruginosa* supernatant. (b) Biofilm biomass of 24 h *E. coli* biofilms exposed to *P. aeruginosa* culture supernatant for 6 h. The control data ('PBS') are from *E. coli* biofilms grown on flat surfaces and exposed to PBS for 6 h.

4.3.3. Growth substrate surface topography controls biofilm surface morphology

Biofilm morphology has important implications for penetration of small molecules, such as antibiotics or interspecies signaling molecules. To investigate the reason why *E. coli* biofilms grown on different growth surfaces exhibiting striking differences in their response to *P. aeruginosa* dispersal signaling and colonization, I characterized the effects of growth surface topography on the morphology of *E. coli* biofilms. Confocal laser scanning microscopy was used to quantify the surface roughness of *E. coli* biofilms, and this analysis revealed that the roughness of the surface of *E. coli* biofilms decreased with increasing post height (Fig. 30a & b). This decrease in specific surface area of biofilms grown on higher aspect ratio posts suggests a mechanism for limiting diffusion of compounds into or out of the biofilm: I hypothesized that differences in specific surface area would result in the differential accumulation of certain compounds or metabolites in *E. coli* biofilms, and that the higher concentrations of these compounds in biofilms may be responsible for the observed suppression of the dispersal response to *P. aeruginosa* culture supernatant.

One candidate compound is indole, a metabolite *E. coli* produces constitutively as part of tryptophan biosynthesis,[186,187] and which has been implicated in moderating *E. coli* biofilm formation [142] and interactions in *P. aeruginosa* cocultures[142,188,189] . To investigate the role of indole in *E. coli* biofilm development, I tested biofilm formation and dispersal in a strain of *E. coli* unable to produce indole (Δ*tnaA*). Biofilms of this indole-defective strain readily dispersed on all flat and structured surfaces, independent of post height (Fig. 31), in contrast to biofilms of the wild-type, indole producing strain, which resisted dispersal on post surfaces (Fig. 28d, 29b). Adding exogenous indole to biofilms of the indole-deficient Δ*tnaA* strain successfully inhibited their dispersal response to *P. aeruginosa* supernatant in a dose-dependent manner (Fig. 32),

suggesting that higher concentrations of accumulated indole in biofilms are indeed responsible for inhibiting *E. coli* dispersal response.

To investigate how biofilm morphology influences indole accumulation, I used finite element modeling (FEM) to measure indole production and diffusion in *E. coli* biofilms grown on flat and patterned surfaces. 3D confocal images of *E. coli* biofilms grown on different surfaces were used to construct FEM meshes. At constant generation rates, as would be expected for a constitutively expressed pathway, modeling results showed that indole concentrations were greater within the biofilms grown on taller post surfaces as compared to those grown on flat surfaces (Fig. 30c)**.** The modeling data showed that the concentration of indole in *E. coli* biofilms increased with increasing post height and correspondingly smoother biofilm-medium interfaces (Fig. 30d). The model indicated that biofilms grown on 11 μm post surfaces resulted in a nearly 10-fold increase in steady state indole concentrations (345 μM) compared to those grown on flat surfaces (35 μM). The densities of cells within the biofilms on flat and post surfaces followed similar trends as a function of height above the substrate surface (Fig. 33 and 34), though biofilms grown on taller post surfaces accumulated more biomass in total (Fig. 35). Such thicker biofilms might be expected to accumulate more indole by simple bulk diffusion considerations. To isolate the contribution of biofilm smoothing on tall post surfaces to the accumulation of indole, I truncated the biofilm mesh in the FEM above the base of the structured growth surface to normalize the total biomass of biofilms grown on 11 μm post surfaces to those of biofilms grown on flat surfaces ("11 ¦ m cropped" in Fig 3d & e). Simulations of indole diffusion in these cropped biofilms still showed a three-fold greater steady state concentration of indole within the biofilm as compared to that within biofilms grown on flat surfaces (Fig. 30d, Fig. 36). These results suggest a mechanism by which the physical topography of the growth surface is able to

tune and ultimately switch the dispersal signaling pathway in *E. coli* by differential accumulation of indole. The higher indole concentrations in the biofilms on post surfaces can account for silencing of the dispersal response to *P. aeruginosa* signaling compounds and are consistent with results from previous studies.[190]

In addition to the increased indole concentration inside the biofilms, FEM data also showed that the total flux of indole out of the biofilms increases with increasing post height due to the steeper concentration gradient across the biofilm-medium interface (Fig. 30e). Indole affects *P. aeruginosa* virulence and quorum sensing pathways, and it mediates *E. coli-P. aeruginosa* coculture development in other systems.[189,190] To test the effects of indole on biofilm development, *P. aeruginosa* and *E. coli* cultures were grown in microfluidic flow cells (Fig. 37) to keep the medium concentrations of indole constant, especially in *P. aeruginosa* cultures which actively degrade it.[190] *P. aeruginosa* cultures grown in presence of indole did not develop into biofilms (Fig. 38). On the other hand, cultures grown for 24 h without indole followed by 24 h growth in medium supplemented with indole exhibited similar biofilm development to 48 h cultures grown without indole at all, suggesting an effect on early stages of *P. aeruginosa* biofilm formation. In contrast, *E. coli* biofilms grown in flow cells with supplemented indole showed only marginally decreased biomasses compared to those grown without indole (Fig. 39). Similarly, the biomass of static 24 h *E. coli* biofilms were minimally affected by indole supplemented during growth (Fig. 40a) or exposed to indole for 6 h after growth (Fig 40b). Therefore, the accumulated biomass and surface roughness changes induced by growth on structured surfaces suggest a molecular mechanism, via indole accumulation, for both retention of *E. coli* biofilms challenged by *P. aeruginosa* culture supernatant on the growth surface and

their resistance to *P. aeruginosa* colonization. Moreover, the height of the post arrays upon which the *E. coli* biofilms were grown determines the magnitude of these effects.

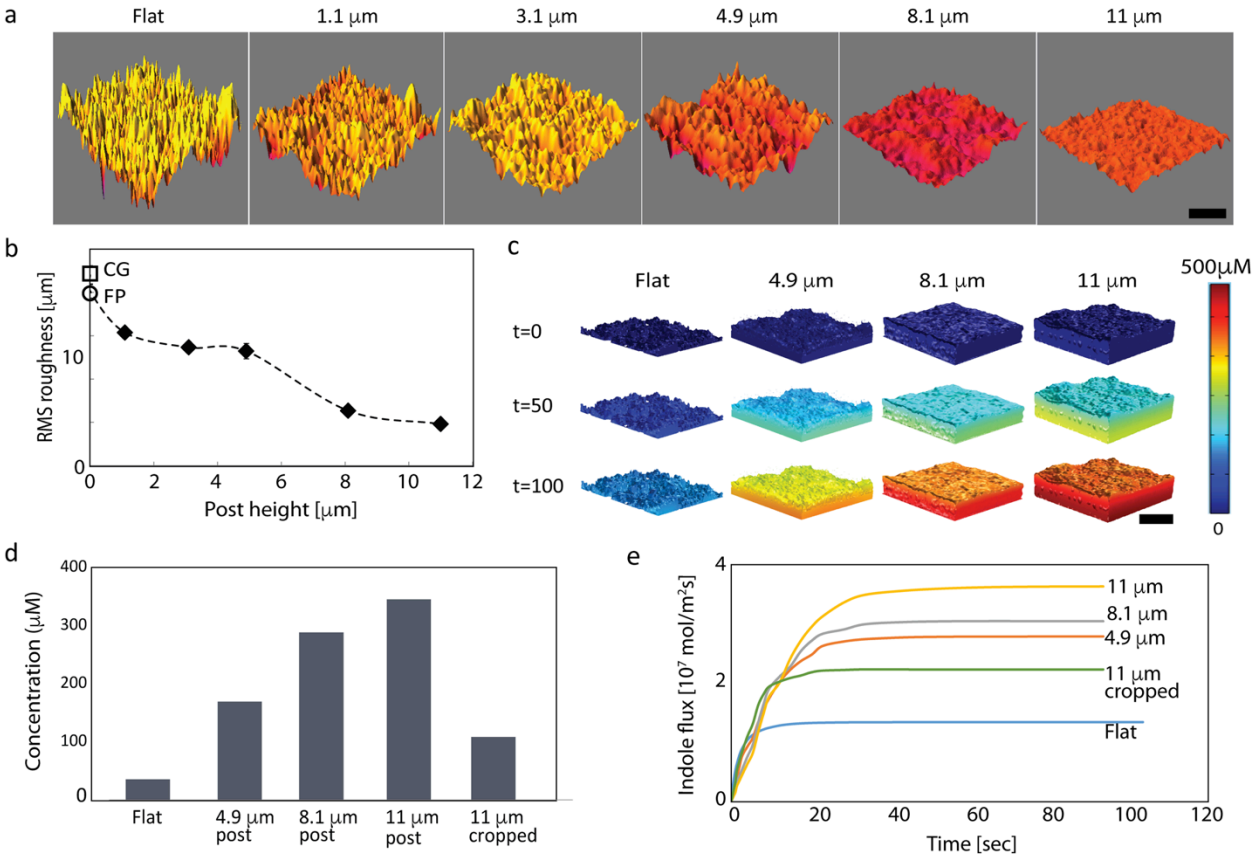

Figure 30. Surface topography modulates biofilm morphology and accumulation of indole. (a) 2D surface maps of the biofilm-media interface of cultures grown on patterned surfaces of different post heights and imaged with two-photon 3D confocal microscopy. (b) Root mean square roughness of *E. coli* biofilm-liquid interfaces grown on flat coverglass (CG, open square), flat polymer (FP, open circle) and polymer post surfaces (black diamonds). (c) Finite element (FE) analysis of indole diffusion in *E. coli* biofilms grown on post and flat surfaces. Colors correspond to the concentration of indole in FE cells at different time points from initiation (t=0) of indole generation and accumulation within the biofilm. (d) Steady state concentrations of indole within biofilms grown on different post and flat surfaces calculated using FE modeling of 3D biofilm images shown in (c). The "11 ¦ m cropped" biofilm is the 11 ¦ m post surface biofilm with the bottom truncated to normalize its biomass to that of the flat biofilm. (e) Total diffusive flux through the biofilm-liquid interface as a function of time, measured using FEM of 3D biofilm images shown in (c). Scale bars are 20 μm.

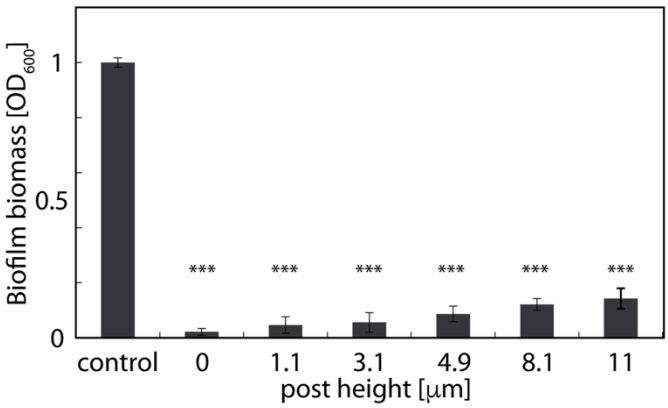

Fig. 31. **Dispersal of *E. coli ΔtnaA* on flat and structured growth surfaces**. Biofilm biomass of the *E. coli ΔtnaA* knockout mutant, which is deficient in indole production, exposed to *P. aeruginosa* PA14 WT culture supernatant and quantified by a crystal violet (CV) assay. Biofilms of the *ΔtnaA* mutant were grown on flat ("0") and patterned substrates of different post heights, as indicated in the plot, for 24 h and exposed to *P. aeruginosa* culture supernatant for 6 h. The control is a *ΔtnaA* biofilm grown on a flat substrate and exposed to PBS instead of the supernatant. *** indicates $p < 0.001$.

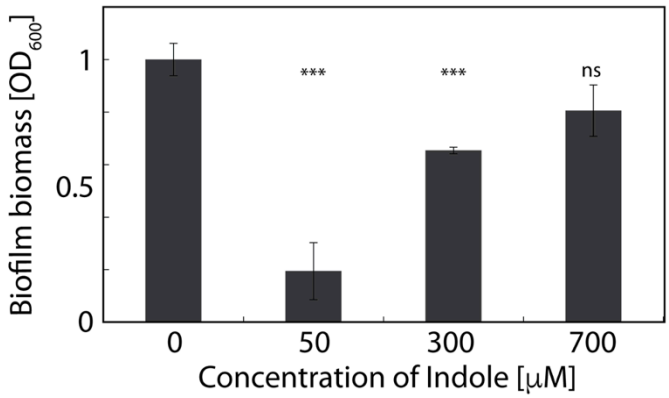

Fig. 32. Crystal violet assay of *E. coli ΔtnaA* mutant grown in presence of indole. Biofilm biomass, quantified by a CV assay, of mature *E. coli ΔtnaA* biofilms, grown with the indicated concentrations of indole supplemented to the growth medium, after exposure to *P. aeruginosa* culture supernatant for 6 h. The culture grown without supplemented indole ("0") was not exposed to *P. aeruginosa* culture supernatant and represents the control biofilm biomass relative to which the other data points are compared. *** indicates *p* values < 0.001 and ns indicates no statistically significant difference compared to the 0 μM indole sample.

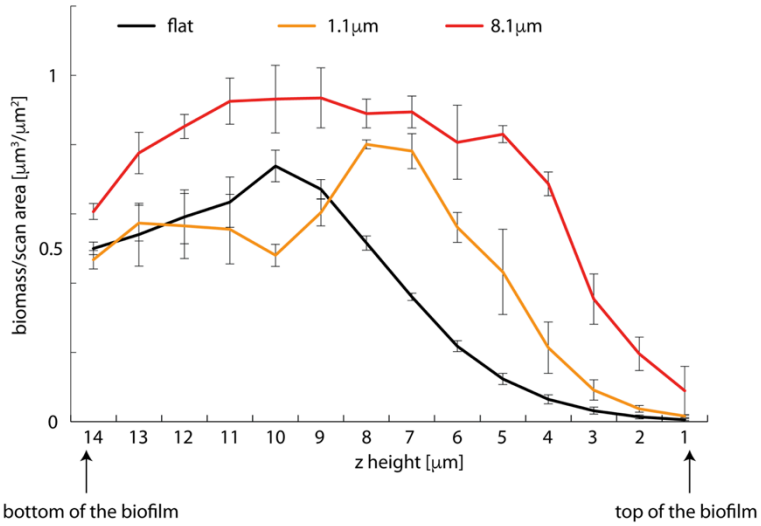

Fig. 33. Biofilm cell density of 24 h *E. coli* biofilms grown on flat, 1.1 and 8.1 μm tall post patterned substrates plotted as a function of z height within the biofilm.

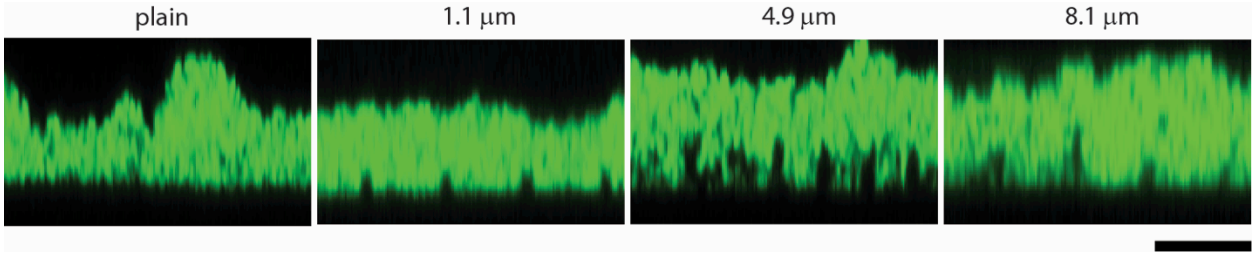

Fig. 34. Cross sectional view of a 3D CLSM image of a 24 h *E. coli* biofilms grown on flat ("plain") and patterned substrates of different post heights. Scale bar is 10 μm

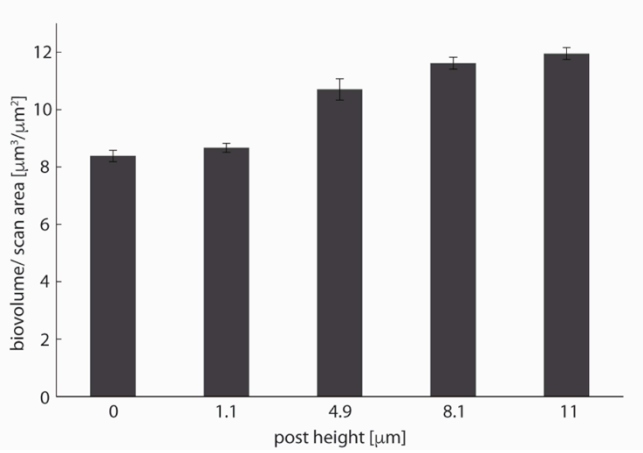

Fig. 35. The total biofilm biomass of 24 h *E. coli* biofilms grown on flat ("0") and patterned substrates of different post heights normalized to scan area calculated from integrated fluorescence intensity.

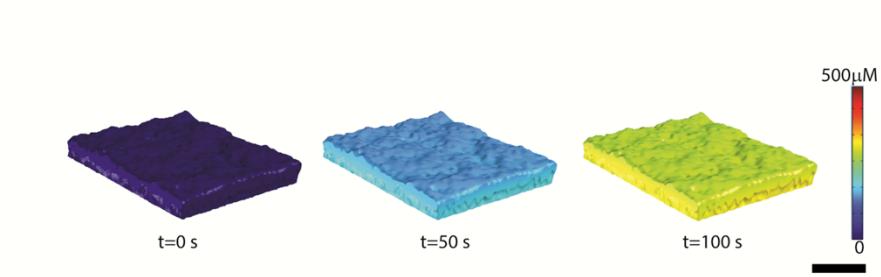

Fig. 36. FEM of indole accumulation over time in a biofilm grown on an 11 μm post substrate. The biofilm mesh was cropped above the biofilm-substrate interface to normalize it to the biomass of a biofilm grown on a flat substrate for FEM using COMSOL MULTIPHYSICS software. 3D heat map color indicates the concentration of indole concentration according to the scale on the right. Scale bar is 20 μm.

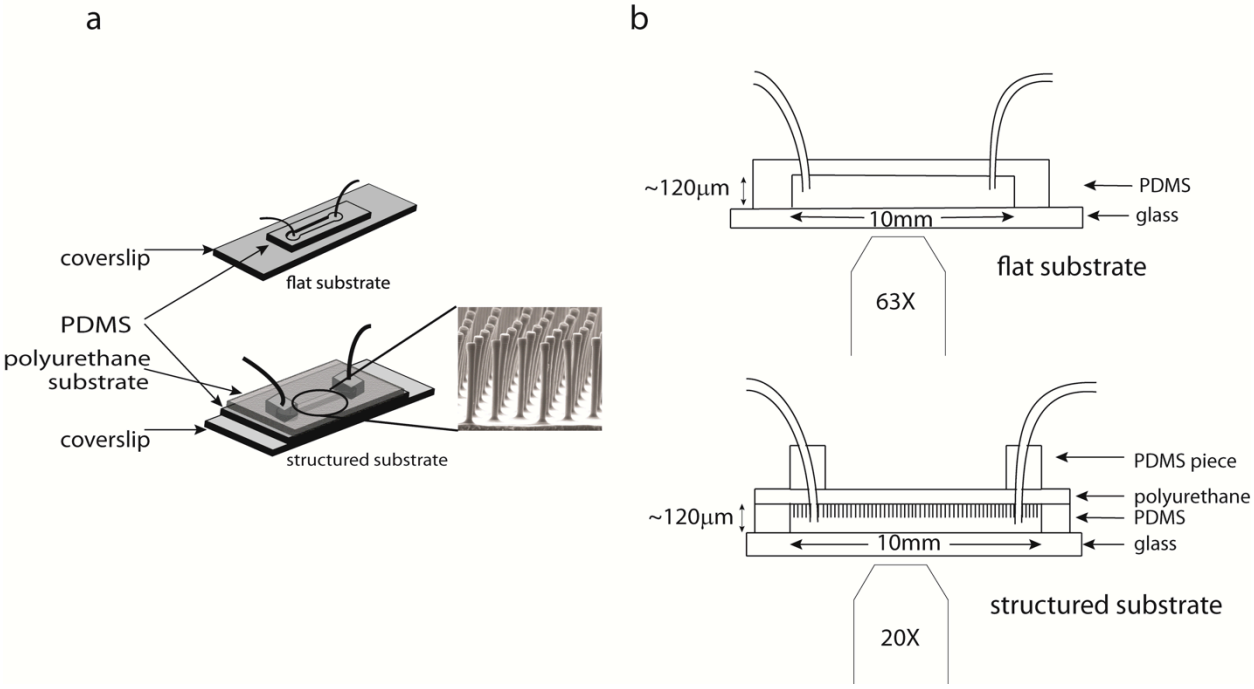

Fig. 37. Microfluidic devices for time series experiments. (a) Schematic of the microfluidic devices on flat (top) and post (bottom) substrates. (b) Cross-section view of the schematic of microfluidic devices on flat (top) and post (bottom) substrates. Biofilm development was dynamically imaged on the coverglass (channel bottom) for growth on flat surfaces and the polyurethane structured surface (channel top) for growth on patterned substrates.

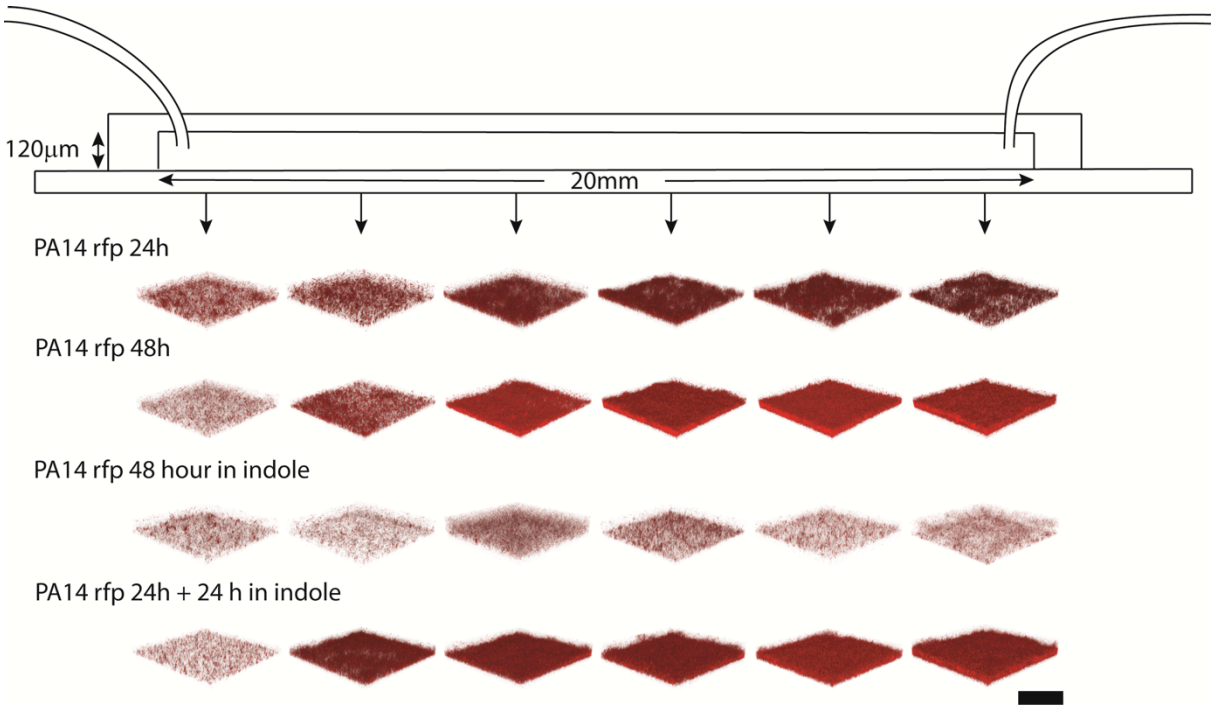

Fig. 38. **Effect of indole on *P. aeruginosa* biofilm growth.** *P. aeruginosa* PA14 *rfp* biofilms were grown on glass coverslips in a single channel microfluidic device. 3D confocal images at different positions along the channel, indicated by arrows, show (top to bottom) a 24 h PA14 *rfp* biofilm, a 48 h PA14 *rfp* biofilm, a PA14 *rfp* biofilm grown for 48 h in media supplemented with 1 mM indole, and a PA14 *rfp* biofilm grown for 24 h in neat media and grown for another 24 h in media supplemented with 1 mM indole. All biofilms in this image were grown in TB media with or without supplemented indole, as indicate. Scale bar is 20 ¦ m.

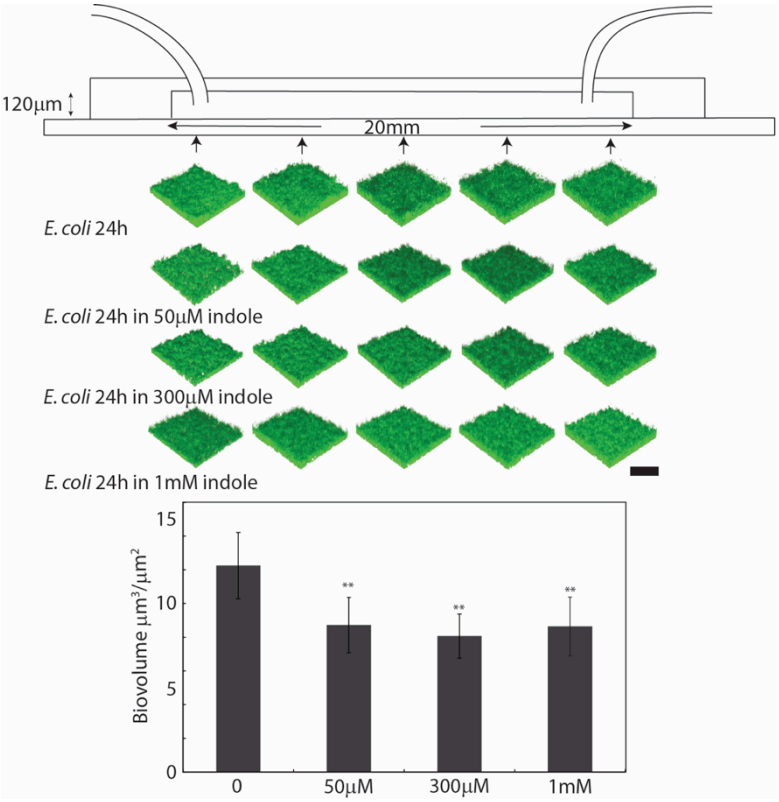

Fig. 39. Effect of indole on *E. coli* biofilm growth. *E. coli yfp* biofilms were grown on glass coverslip in a single channel microfluidic device. 3D confocal images at different positions along the channel, as indicated by arrows, show 24 h *E. coli yfp* biofilm grown in tryptone medium without indole and 24 h *E. coli yfp* biofilms grown in tryptone medium supplemented with different concentrations of indole. The bar graph shows the average of total biofilm biomasses under different indole conditions along the channel. Scale bar is 20 μm. ** indicates p values < 0.05

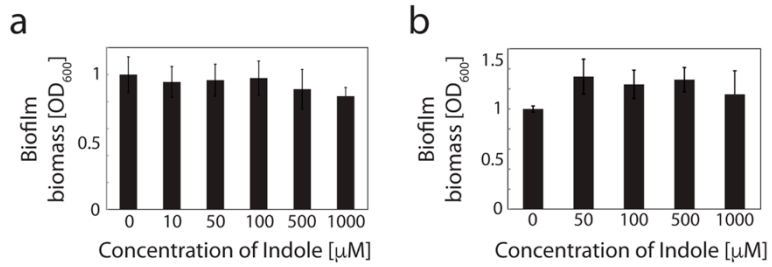

Fig. 40. Effect of indole on *E. coli* biofilm growth and dispersal. (a) Biomass of 24 h *E. coli* biofilms grown in tryptone medium supplemented with different concentrations of indole in well plate growth experiments. (b) Biomass of *E. coli* biofilms grown for 24 h then exposed to different concentrations of indole for 6 h in well plate growth experiments. The control biofilm ("0") was left in PBS and all biofilms were rinsed with PBS after 6 h of indole exposure

4.3.4. Surface topography-programmable probiotic surfaces

To further investigate the response of *E. coli* biofilms grown on different surface topography when exposed to planktonic *P. aeruginosa* cells, *E. coli* biofilms on flat and structured surfaces in microfluidic flow cells were visualized by dynamic 3D imaging (Fig. 37). Whereas mature *E. coli* biofilms grown on flat surfaces persisted less than 3 days before being supplanted by *P. aeruginosa* biofilms, those grown on 8.1 μm post surfaces resisted *P. aeruginosa* colonization for over 19 days (Fig. 41a). This result suggests that the biofilm growth surface could be manipulated to impart a probiotic character to associated biofilms.

Because surface topography influenced the diffusion of indole, we hypothesized that it would also determine the penetration of antibiotics into the biofilm. Coculture biofilms were grown on flat and post surfaces and subsequently treated with 1 mM rifampicin in PBS. As shown in Figure 41b & 41c the fraction of dead cells in the surface-associated population increased with increasing post height. Because *P. aeruginosa* is naturally resistant to rifampicin, this result is consistent with the increase in population fraction of rifampicin-susceptible *E. coli* in the population on the tall post surface (Fig. 28d). While both the flat surface coculture and PBS treatment controls show no cytotoxic effect of the rifampicin, over 97% of the cells are killed by the same treatment of the 11 μm post cocultures. Thus, *E. coli* biofilms grown on the 11 μm post surfaces are both more resistant to *P. aeruginosa* colonization and more susceptible to antibiotics.

P. aeruginosa that has colonized a surface and formed chronic biofilm infections becomes increasingly resistant to antibiotic treatment.[149,191–193] Therefore, I also tested whether these micropatterned growth surfaces would modify the susceptibility of monoculture biofilms to antibiotic treatment. Biofilms of *E. coli* and *P. aeruginosa* monocultures grown separately on

post surfaces were found, by live/dead staining, to be increasingly susceptible to antibiotic treatment with increasing post height as compared to the same biofilms grown on flat surfaces (Fig. 41d). Growth on post surfaces increased the susceptibility of *E. coli* and *P. aeruginosa* in biofilms to 500 μM carbenicillin, a concentration 6 and 95x greater than its reported minimum inhibitory concentrations (MICs) against *P. aeruginosa* and *E. coli*, respectively.[194] The cause of the increased susceptibility of the monocultures is a matter of further study, but these results suggest that the growth surface microenvironment induces significant physiological changes in associated biofilms.

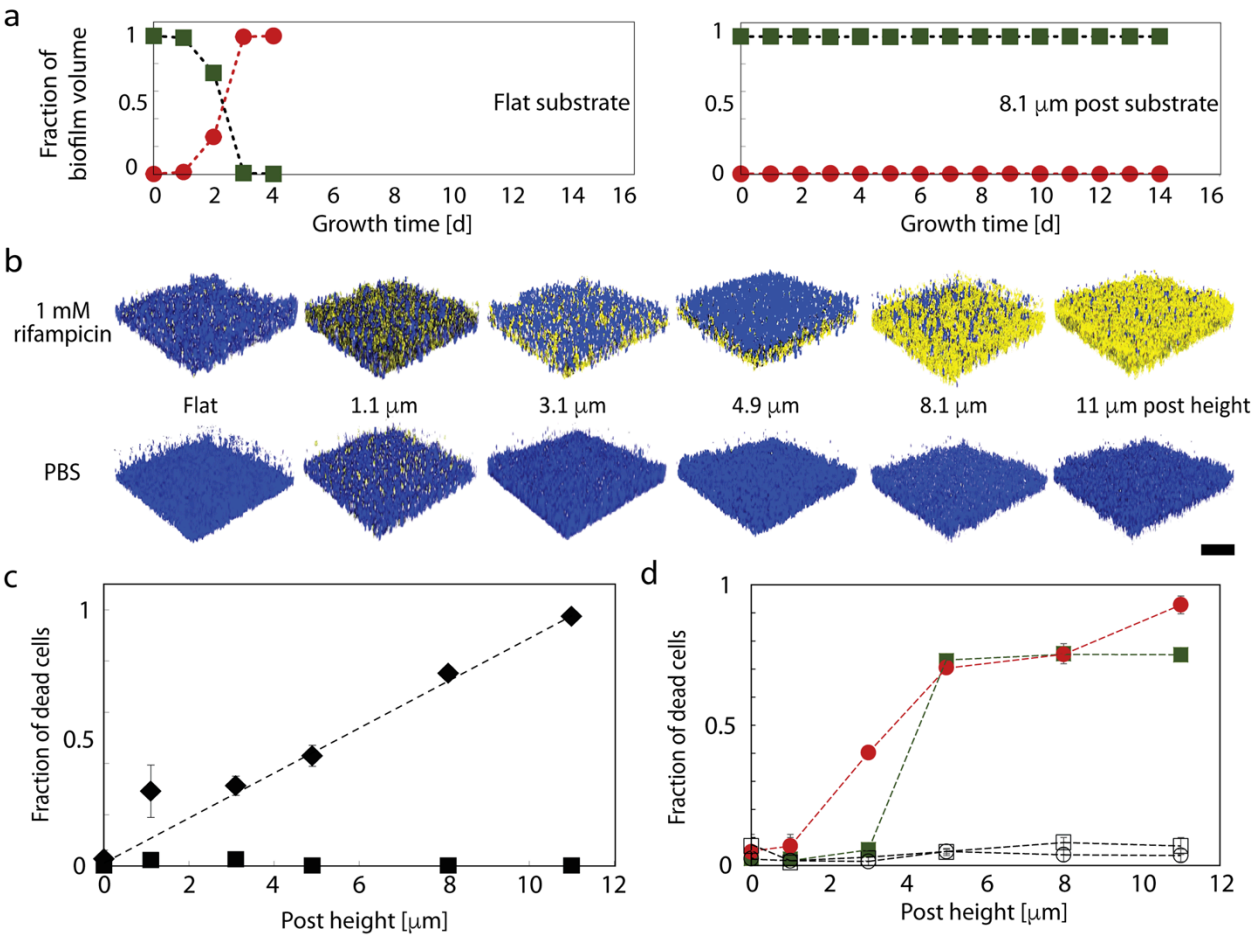

Figure 41. Growth surface topography determines structure-property relationships in the form of persistent, pathogen-resistant surfaces and increased antibiotic susceptibility. (a) *E. coli* and *P. aeruginosa* cells as fractions of total biofilm volume in a microfluidic device over time. *E. coli* biofilms

were grown on flat and 8.1 μm post surfaces within the imaging channel and exposed to a *P. aeruginosa* inoculated media (green squares and red circles indicate biofilm fractions of *E. coli* and *P. aeruginosa*, respectively). (b) Coculture biofilms of *E. coli* and *P. aeruginosa* on flat and post surfaces treated with 1 mM rifampicin or PBS. Treated biofilms were stained with SYTO 9 (blue, stains live cells) and propidium iodide (yellow, stains dead cells). (c) Fraction of dead cells in biofilms grown on flat and post surfaces (filled diamonds and squares indicate rifampicin and PBS treated biofilms, respectively). (d) Fraction of dead cells in the monoculture biofilms of *E. coli* (green squares) and *P. aeruginosa* (red circles) grown on flat and post surfaces and treated with 500 μM carbenicillin respectively. Open squares and circles correspond to the fractions of dead cells in *E. coli* and *P. aeruginosa* biofilms grown on the different surfaces and exposed to PBS only. Scale bar in (b) is 20 μm.

Similar chemical interactions have been reported in various cocultures but have not exhibited such distinct phenotypes or provided evidence for coupled physical and molecular mechanisms defining these coculture biofilm dynamics. The smoothing of *E. coli* biofilm surfaces on increasingly tall posts is the critical morphological change responsible for enhancing the accumulation of indole within the biofilm, constituting the basis for the community structure-function relationships studied here. Indole was previously found to improve competition of *E. coli* with *P. aeruginosa* in cocultures.[189] These results extend these findings to biofilms and demonstrate a dual effect of indole on both *E. coli* and *P. aeruginosa*. FEM suggests that indole accumulates to a greater extent in *E. coli* biofilms grown on post surfaces as compared to those grown on flat surfaces. The observation that the Δ*tnaA E. coli* mutant, deficient in indole production, retains its dispersal response on all structured and flat surfaces (Fig. 31), establishes the role of indole in silencing the dispersal signaling pathway in *E. coli*.

Previous studies have reported that indole decreases biofilm growth in *E. coli,*[142,195] but my experiments show that indole has no effect on growth of static biofilms of *E. coli* (Figs. 41) and very little effect on *E. coli* biofilms grown in microfluidic devices (Fig. 39). The effect of indole signaling varies with temperature[195] and in different species of bacteria,[189,190,196,197] and seemingly cooperative effects have been observed in some *E. coli-P. aeruginosa* cocultures.[198]

The differences between growth conditions and strains used in this study and those of the previous studies might account for the differences in observations. The effects of indole signaling on *E. coli* at different temperatures merit further study. Based on my data, however, I expect that these discrepancies may depend on the amount of indole produced by a given strain under specific conditions, such as the availability of tryptophan in the growth medium. Indole accumulation or depletion, such as by the production of indole within biofilms as opposed to by planktonic cells, or the presence of an indole degrading bacterium, such as *P. aeruginosa*, are also critical factors determining the effective concentration. These findings suggesting that indole inhibits *P. aeruginosa* colonization of surfaces has precedent in previous genetic expression and culture growth studies: indole generally inhibits acyl homoserine lactones (AHL) quorum sensing in many gram-negative bacteria and has been shown to reduce *P. aeruginosa* virulence.[189,190,199] Interfering with *P. aeruginosa* sensing of endogenous AHLs is a plausible mechanism by which increased indole concentrations in *E. coli* biofilms may inhibit surface colonization by the pathogen.

The surface structures used in this study modify the morphology of *E. coli* biofilms such that the accumulation of indole within the biofilms switches the dispersal pathway through the linked effects described above. The transduction of physical signals by the *E. coli* biofilm to alter a biological signaling pathway demonstrates the potential of growth surface microenvironments for engineering microbial communities. My results show examples of biofilm properties that can be tuned in the *E. coli*-*P. aeruginosa* system in the form of surface-programmable antibiotic susceptibility and persistent (> 2 weeks) pathogen resistance (Fig. 41a). Pathogen resistance on this timescale is relevant for preventing infections in indwelling medical devices.[1,200] The *E. coli* used in these experiments is a derivative of the K-12 strain, which is defective in at least three

cell wall characteristics rendering it benign and incapable of colonizing the human intestinal tract.[201,202] Consequently, my results show that growth surface topography can confer probiotic properties to an otherwise commensal strain, with potential applications in preventing infections in medical settings. Further these surfaces render the biofilms grown on it susceptible to relatively low doses of antibiotics (Fig. 41d). Living in the biofilm state generally increases antibiotic resistance of constituent cells,[52,149,203–205] so it is not surprising that treatment of biofilms with antibiotics well above the MICs results in minimal cytotoxicity. That the susceptibility of biofilm cells dramatically increases as a function of the post height of the micropatterned growth surface, on the other hand, is an unexpected result (Fig. 41d). While the underlying mechanisms of topography-induced changes in biofilm morphology and differential susceptibility are under further investigation, these results suggest that surface microenvironments can have substantial physiological on their supported biofilms.

4.5. Conclusion

In conclusion, growth substrate surface topography produces physical cues capable of mediating competition in coculture biofilms and deterministically controlling biofilm properties. Growth on micropatterned surfaces modulates biofilm-growth medium interfacial roughness and the accumulation of metabolites within the biofilm. The differential accumulation of indole in *E. coli* biofilms is consistent with silencing of a dispersal signaling pathway in response to chemical cues from *P. aeruginosa*, as well as the increased resistance of said biofilms to *P. aeruginosa* colonization. These effects represent design principles for controlling the competition dynamics, structure, and properties of *E. coli*-*P. aeruginosa* coculture biofilms. Surface features are a permanent means of controlling biofilm development, as opposed to transient chemical cues such

as leaching of antibiotic compounds or surface functionalization by adhesion resistant or bactericidal moieties, which are fouled or cleaved by microbial activity. The results in this chapter further the development of design principles for engineering bacterial community structure-function relationships and are potentially useful for creating synthetic microbial consortia for applications in biomedical, bioenergy, and environmental technologies.

The ability of growth substrate patterns to determine antibiotic susceptibility is a potentially powerful method to treat biofilm infections, though it is unclear why the surface topography affects the response of associated biofilms to antibiotic treatment. It is possible that physiological changes in biofilms grown on patterned surfaces compared to those grown on flat surfaces could account for this difference. As a result, I hypothesized that changes in metabolic activity of cells within biofilms grown on different surfaces could serve as an indicator of changes in biofilm physiology. The next chapter describes my efforts to map the metabolic states of bacteria within biofilms. To do so, my collaborators and I developed a non-invasive and label free microscopy technique to quantify, with single-cell resolution, the relative metabolic state of bacteria in planktonic and biofilm cultures.

Chapter 5.

Metabolic fingerprinting of bacteria by fluorescence lifetime imaging microscopy

5.1. Introduction

Results from the previous chapter suggest that biofilms grown on microstructured surfaces were significantly more susceptible to antibiotics compared to biofilms on flat substrates. Bacteria within biofilms are often several orders of magnitude more resistant to antibiotics than free-living, planktonic bacteria, so this result is surprising and may represent a promising direction of study for biofilm treatment strategies. One general mechanisms of antibiotic resistance in biofilms is the relatively low metabolic activity or dormancy of constituent cells compared to planktonic cells. In this chapter, I demonstrate the potential of fluorescence lifetime imaging microscopy of a metabolic coenzyme to differentiate metabolic states in live bacterial populations with single-cell resolution. Results from this study show that the metabolism of bacteria on post substrates are like planktonic bacteria. This study was conducted in collaboration with Dr. Rupsa Datta in the Gratton lab at UCI.

Bacteria are found in diverse environments and their ability to modulate metabolic processes in response to adverse conditions gives them unique survival advantages. In the natural environment, multiple species interact in complex niches and exhibit a range of community behavior[76,206–208]. In the medical environment, these metabolic changes make bacterial infections difficult to eliminate. Treatment of bacterial infections are often hindered by emergence of multi-drug resistant phenotypes[209,210]. A major source of antibiotic resistance and tolerance are slow growing ‘persister’ phenotypes, which are often associated with biofilm formation and chronic

infections[211–213]. Mapping the metabolic activity of bacteria within natural communities and medical infections, therefore, can provide insights into the role of metabolism in determining bacterial community behavior.

Fluorescence spectroscopy is a non-invasive technique which has been extensively used for metabolic imaging in mammalian cells. Fluorescence lifetime imaging microscopy (FLIM), in particular, is a powerful label-free method to probe the local environment and molecular conformation of endogenous fluorophores[214]. The FLIM signature of an autofluorescent metabolic coenzyme, reduced nicotinamide adenine dinucleotide (phosphate) (NAD(P)H), has been employed as an endogenous biomarker for metabolic activity of mammalian cells in cancer biology and the detection of stem cell differentiation[215–221]. NAD(P)H in its free state has a significantly shorter fluorescence lifetime (0.4 ns), due to self-quenching, than its protein bound state and thus easily discernable by FLIM.[222] FLIM measurements allow mapping of NAD(P)H lifetimes with sub-cellular resolution. The relationship between the NAD(P)H fluorescence lifetime and metabolic activity, however, has not been established in bacteria.

As in the case of mammalian cells, bacteria produce many endogenous fluorescent molecules with distinct spectral characteristics[223,224], some unique to specific bacteria[225,226], rendering them as promising probes for identification and characterization. Fluorescence spectroscopy of some intrinsic fluorophores has been previously explored in bacteria for the detection, differentiation, and characterization of various species[227–231]. The relationship between cytosolic concentrations of NAD(P)H in bacteria and their metabolic activity has been previously investigated[232–236], and differences in the ratio of NAD^+ and NADH are correlated with different metabolic states under aerobic and anaerobic conditions, dissolved oxygen tension, and growth phase[237–239]. Some fluorescence lifetime measurement on bacteria have been previously reported

in attempts to detect and differentiate bacterial species[238,240,241]. More recently, NAD(P)H fluorescence lifetime measurements were obtained from bacteria infecting mammalian cells, though no quantitative relationship to metabolic activity was determined[242].

A previously established phasor approach to FLIM is a fit-free technique which does not require *a priori* knowledge of the fluorescent species in the sample[243,244]. In brief, lifetime decay information from each pixel of the image is analyzed via Fourier transform to obtain the corresponding phasor position and the resulting 2-D histogram is plotted as a distribution on the phasor plot. The *g* coordinate of the phasor plot extend between 0 and 1 while *s* coordinate has values between 0 and 0.5. All single exponential lifetime decays fall on the 'universal circle' defined as a semi-circle of radius 0.5 between points (0,0) and (1,0) on the phasor plot. Phasors corresponding to a fluorescence lifetime value of 0 will fall on point (1,0) while longer lifetime signals will shift towards point (0,0) with increasing lifetime. The phasor of a mixture of two molecular species (each with single exponential lifetimes) will lie inside the universal circle on the line joining the phasor position of the two pure species, depending on the fractional contribution of each component. Hence, the position of the FLIM-phasor is directly related to the ratio of free to enzyme-bound NAD(P)H[245,246]. A 'right shift' of the phasor indicates a larger free to bound ratio while a decrease in the ratio is indicated by a 'left shift' to coordinates corresponding to longer lifetimes. Lifetimes within the phasor distribution from a sample can be mapped back onto the acquired image to form the corresponding FLIM map. NAD(P)H FLIM-phasor has been successfully applied to study metabolism and oxidative stress in tumors[220,221,247], cardiomyocytes[220], metabolic fingerprinting of macrophages[248], stem cell differentiation[219], and in *Lactobacillus acidophilus* cultures[249].

Phasor fingerprints were generated for immobilized planktonic cell populations of *Escherichia coli*, *Salmonella enterica* serovar Typhimurium*, Pseudomonas aeruginosa, Bacillus subtilis,* and *Staphylococcus epidermidis*. The phasor positions of the cells, corresponding to the free to bound NAD(P)H ratio, was found to depend on species, growth phase, and history of exposure to antibiotics and nutrient media. The phasor distribution shifted to shorter (free) NAD(P)H fluorescence lifetimes with exposure to antibiotics, and recovered to longer (bound) lifetimes when bacteriostatic antibiotics were administered and washed away. Moreover, the diffraction-limited FLIM maps achieved here displays differences in the spread of phasor positions of individual cells within the same population under different environmental treatments. As a function of growth phase, the NAD(P)H lifetime phasor distribution changed non-monotonically. This suggests that the FLIM-phasor position captures information about metabolic activity not simply inferred by cell density measurements. These results demonstrate that FLIM of NAD(P)H in live bacterial cultures can be directly related to changes in metabolic activity, and that this method can provide distinct and nuanced information about metabolic states of bacteria *in situ* as compared to existing fluorescence spectroscopy and metabolomic techniques.

5.2. Material and methods

5.2.1 Bacterial strains and growth conditions

The bacterial strains used in this study are listed in table A.1. All strains were revived from frozen stocks by streaking on lysogeny broth (LB) agar (Fisher Scientific) (1.5%) plates. Shaking cultures of bacterial strains were grown in 2 ml LB at 37 °C for 5 h unless stated otherwise. For imaging, the samples were prepared by mixing LB shaking cultures with 1% agarose (Fisher

Scientific) in a 3:7 ratio. 100 µl of the resulting solution was cast on a glass coverslip by spin coating at 500 rpm for 10 seconds.

5.2.2. Exposure of agarose-embedded bacteria to antibiotics and antibiotic recovery

Solutions of nalidixic acid or ampicillin (Sigma-Aldrich) were prepared at the indicated concentrations in sterile ultrapure water, well above the minimum inhibitory concentration in *E. coli*. The agarose-embedded bacterial samples were incubated with a 200 µl of each concentration for 30 min, then washed with sterile ultrapure water and imaged.

For antibiotic recovery experiments, agarose-embedded bacterial samples on glass coverslip were incubated in 0.464 mg/ml nalidixic acid or 0.4 mg/ml ampicillin for 30 min. The samples were washed twice with ultrapure water, then incubated in LB media for 30 min and imaged.

5.2.4. Measurement of cellular respiration

E. coli cells were grown shaking in LB media at 37 ˚C for 5 h. 300 µl of *E. coli* cells in LB media was diluted in 700 µl of PBS with different final concentrations of nalidixic acid and ampicillin. Each of these solutions were done in triplicates. The *E. coli* cells were incubated at 22 °C for 30 min. 20 µl of 0.15 mg/ml resazurin was injected into 100 µl of each of these solutions, and sterile control solutions, in a 96 well plate and the plates were incubated at 37 ˚C for 1 h. Fluorescence intensity from the wells was recorded using a plate reader (BioTek Synergy H1) with a 560 nm excitation / 590 nm emission filter set.

5.2.5. FLIM of planktonic growth curves and growth curve recovery

For each growth curve, 20 ml LB media was inoculated with bacteria to an OD of 0.02 and aliquoted into 1 ml cultures in 20 ml glass culture tubes with loose-fitting metal caps, which were kept shaking at 200 rpm and 37 °C. One culture aliquot was taken out for each bacterium every 2 h, and samples for FLIM measurements were prepared as described above. The optical density (OD) of 1 ml bacterial shaking was measured every 2 h to generate a growth curve. The OD was measure at 600 nm using a Biowave CO8000 cell density meter (Biochrom, Holliston, MA).

For growth curve recovery 1 ml cultures were grown for 15 h, 24 h, 48 h and 13 d in duplicates. 100 µl from one of the duplicate samples was diluted into 900 µl of fresh LB media and shaken for 2 h at 200 rpm and 37 °C. The other set of cultures from each time point was allowed to grow in the same spent culture media for 2 more hours. After 2 h both cultures were taken out of the incubator and samples were prepared for FLIM imaging as described above.

5.2.7. FLIM data acquisition

Dr. Rupsa Datta from the Gratton lab acquired most of the FLIM data shown in this study. She also analyzed this data using the SimFCS software. FLIM was performed on a Zeiss LSM 710 microscope (Carl Zeiss, Jena, Germany) coupled to an 80 MHz multiphoton excitation laser source, Titanium:Sapphire MaiTai laser (Spectra-Physics, Mountain View, CA) with excitation at 740 nm using a 60X, 1.2 N.A. oil immersion objective, (Carl Zeiss, Oberkochen, Germany). The image scan speed was 25.21 µs/pixel with an image size of 256 × 256 pixels. Excitation from emission signal were separated at 690 nm followed by bandpass emission filter 460/80 nm (Semrock, Rochester, NY). Photomultiplier tube (H7422P-40, Hamamatsu, Japan) was used as

the microscope external detector port photo-sensor unit. A320 FastFLIM FLIMbox (ISS, Champaign, IL) was employed to acquire frequency domain FLIM data. SimFCS software (LFD, Irvine) was used for FLIM data acquisition. For calibrating the FLIM system, Rhodamine 110 with known lifetime of 4ns was measured for every experiment. All the (*g*, *s*) coordinate system used to mention phasor cursor coordinates in this article used the first harmonic phasor plots at 80 MHz (repetition rate of the laser).

5.2.8. Spectral data acquisition

NAD(P)H in the bacterial samples was excited with two-photon excitation at 740nm. Fluorescence spectra were collected on a Zeiss LSM 710 microscope spectral detector consisting of 32 channels, between 416-728 nm, each with 9.7 nm bandwidth. For image acquisition, the pixel frame size was set to 256 x 256 and the pixel dwell time was 177 μs/pixel. Spectral data were acquired from the same sample on which FLIM was performed.

5.2.9. Data analysis

FLIM data was analyzed using the SimFCS software developed at the Laboratory of Fluorescence Dynamics (LFD, UC Irvine). To create the bacterial phasors, the average *g* and *s* value of phasor distribution from individual bacterial cell were calculated and plotted as a scatter plot. Thus, each point of the bacterial phasor scatter plot represents a single bacterium. Image segmentation, scatter plot and box plots calculations were performed on MATLAB.

5.2.10. Live/dead assay

Agarose-embedded samples were exposed to different antibiotic concentrations for 30 min and stained with syto 9 and propidium iodide for 20 min. The samples were then washed with ultrapure water and imaged using a Zeiss LSM780 confocal microscope. The live/dead images of agarose-embedded *E. coli* cells were obtained using a Zeiss LSM780 inverted confocal microscope (Carl Zeiss, Jena, Germany) with 63X, NA 1.2 water immersion objective. Dichroic beam splitters were used to reflect laser lines 488/561/633 and 690. Both color channels were imaged using alternating line averaging to avoid blurring of the image due to drifting. These adjustments reduced fluorescence cross-talk to undetectable level in two-color imaging experiments. Confocal images were obtained with a pinhole size of 1 airy unit.
The fraction of dead cells was quantified using the "select objects" from the intensity images from each channel using the Volocity software after deconvoluting the images by applying the point spread function to each channel.

5.2.11. Colony forming unit (CFU) analysis

1 ml shaking cultures of E. coli was grown for 5 h and exposed to 0.464 mg/ml nalidixic acid or 0.4 mg/ml ampicillin for 30 min. The cells were centrifuged at 2000 x *g* and resuspended in LB media and incubated at 37 ˚C and shaking at 250 rpm for 30 min. The control was not exposed to antibiotics and each condition was done in triplicate. Serial dilutions of the shaking cultures were plated to count CFUs to measure recovery from antibiotic exposure.

5.3. Results.

5.3.1. Fluorescence lifetime phasor fingerprint of different bacterial species

Two-photon FLIM of five clinically relevant species of bacteria, *E. coli, S.* Typhimurium*, P. aeruginosa, B. subtilis and S. epidermidis* was performed on planktonic cells immobilized in agarose. Each species was imaged at a mid-exponential phase of growth to generate a phasor fingerprint (Fig. 42a and Fig. 43). A comparative analysis of all the phasor coordinates of each bacterial cell, represented by a single data point, within each species population (*n = 10*), shows variations along both *g* and *s* axes of the phasor plot (Fig. 42b). The bacterial phasor distribution displays greater variation along the *g* axis (between 0.3 to 0.45) than the *s* axis on the phasor plot (Fig. 42c).

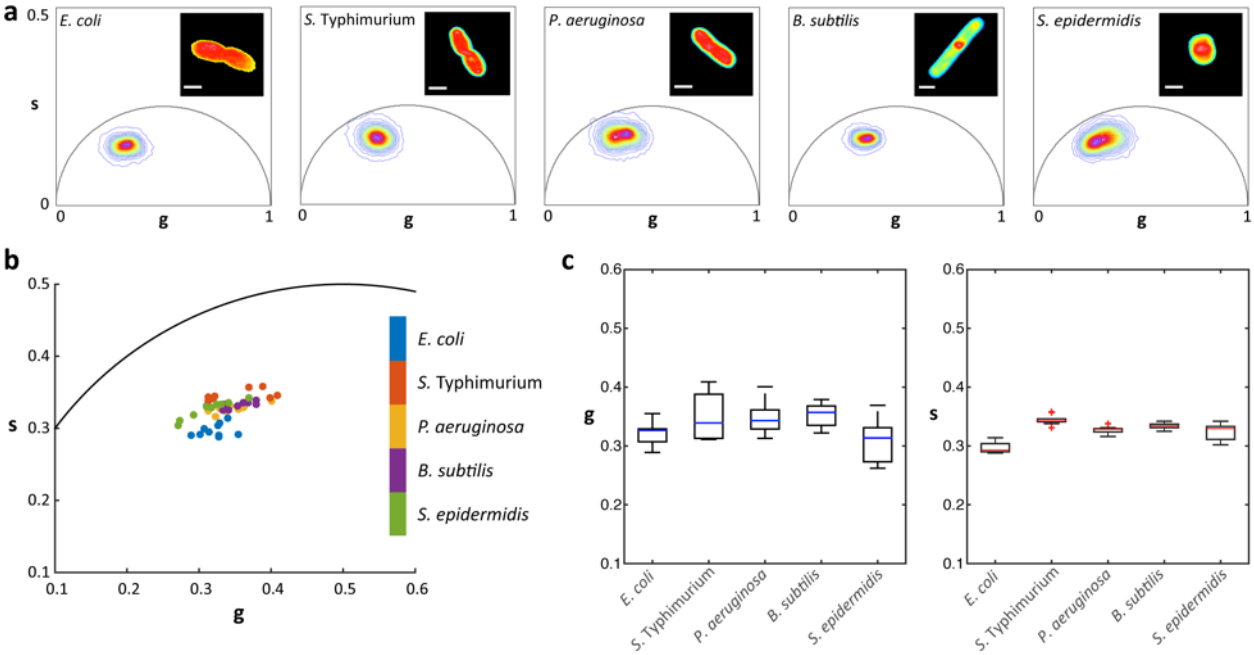

Fig. 42. Bacterial phasor fingerprints. (a) Phasor distribution of *E. coli, S.* Typhimurium*, P. aeruginosa*, *B. subtilis* and *S. epidermidis*. Inset panels are representative fluorescence intensity images of each bacterium. (b) Bacterial phasor fingerprints of individual cells within each bacterial population. (c) Distribution of *g* and *s* within each bacterial population. Scale bars are 1 µm.

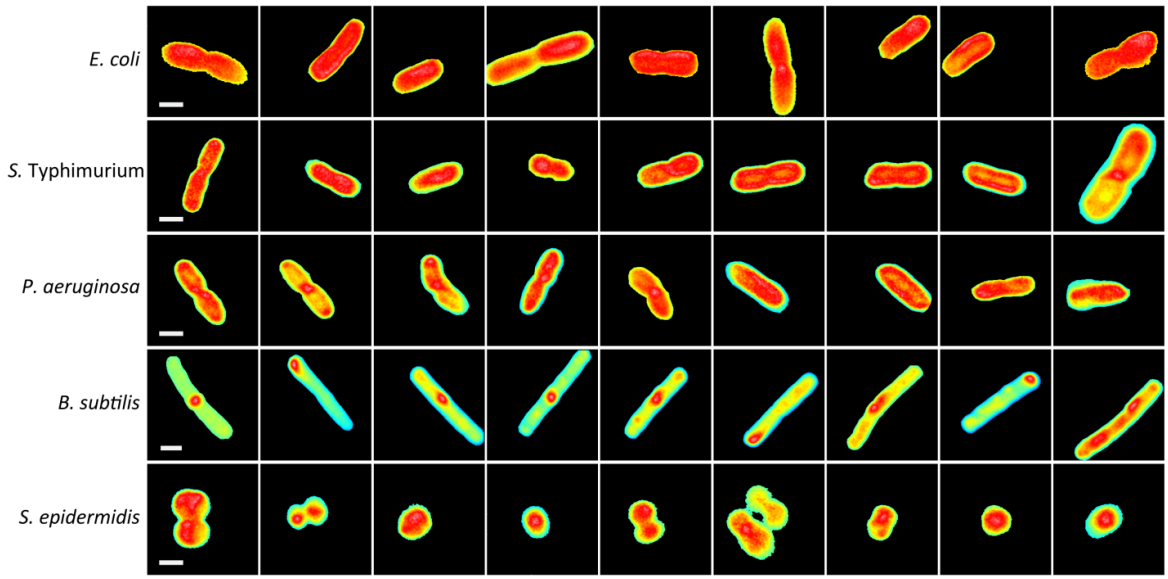

Fig. 43. Representative fluorescent intensity images of individual *E. coli, S.* Typhimurium*, P. aeruginosa*, *B. subtilis,* and *S. epidermidis* cells, excited with two-photon excitation at 740 nm. Scale bars are 1 μm.

5.3.2. Response of *E. coli* phasor to antibiotic exposure

Bacteria encounter various stresses in their natural environments and they elicit specific and highly regulated responses via changes in their metabolism[211,213,250,251]. To determine the relationship between the FLIM phasor and metabolic activity, I probed the phasor response of *E. coli* to antibiotic treatment. Agarose embedded cells were treated with nalidixic acid or ampicillin, a bacteriostatic antibiotic and bactericidal antibiotic, respectively, then NAD(P)H FLIM was performed. The phasor position of *E. coli* cells treated with nalidixic acid shifted towards longer fluorescence lifetimes with increasing concentration (light to darker shades of brown dots), as compared to the untreated control population (cyan dots) (Fig. 44a). The *g* distribution exhibited a sharply increasing mean value at the lowest nalidixic acid concentration, while the mean *s* values were weakly sensitive to nalidixic acid concentration (Fig. 44b). *E. coli* cells similarly exposed to increasing concentrations of a bactericidal antibiotic, ampicillin, also

exhibited corresponding phasor position shifts to larger *g* values, while *s* values remained relatively constant with ampicillin concentration (Fig. 44c and Fig. 44d) when compared with cells in control conditions. These shifts of the phasor position of cells treated with antibiotics corresponds to a concentration-dependent increase in the fraction of dead cells when stained in a live/dead assay (Fig. 45 and 46). Exposure of *E. coli* cells to the same volume of water for the same amount of time did not cause a shift and the position of the phasor was maintained at the same position as the control population (Fig. 47).

To benchmark the FLIM phasor data with an independent metabolic activity measure, I used a resazurin assay to quantify aerobic respiration in planktonic cultures. Resazurin is a redox indicator, sensitive to the presence of oxygen and reducing equivalents, such as NADH. Under reducing conditions, resazurin is reduced to the fluorescent compound, resorufin, and the fluorescence intensity has been linked to bacterial respiration rates [252,253]. Exposure of *E. coli* to the bacteriostatic nalidixic acid resulted in a significant drop in culture respiration, even at the lowest concentration tested in our study (Fig 48). Exposure of *E. coli* to bactericidal ampicillin, however, resulted in a slight increase in metabolic activity for cells exposed to 0.04 mg/mL ampicillin, which decreased with further increasing ampicillin concentration. The resazurin data are consistent with results and trends in the FLIM phasor data, which show a large shift to higher free to bound NAD(P)H ratios with exposure to 0.116 mg/mL nalidixic acid, and little to no concentration dependence thereafter (Fig. 44b). The FLIM data do not show a shift to lower free to bound NAD(P)H at 0.04 mg/mL ampicillin, but the data is within error of the starting culture and the change indicated by the resazurin assay is small relative to that observed for nalidixic acid exposure (Fig. 44d). The resazurin assay and FLIM data, however, show a trend to lower metabolic activity and higher free to bound NAD(P)H, respectively, with increasing ampicillin

concentration, which is distinct from the cell response to nalidixic acid as assessed by both methods.

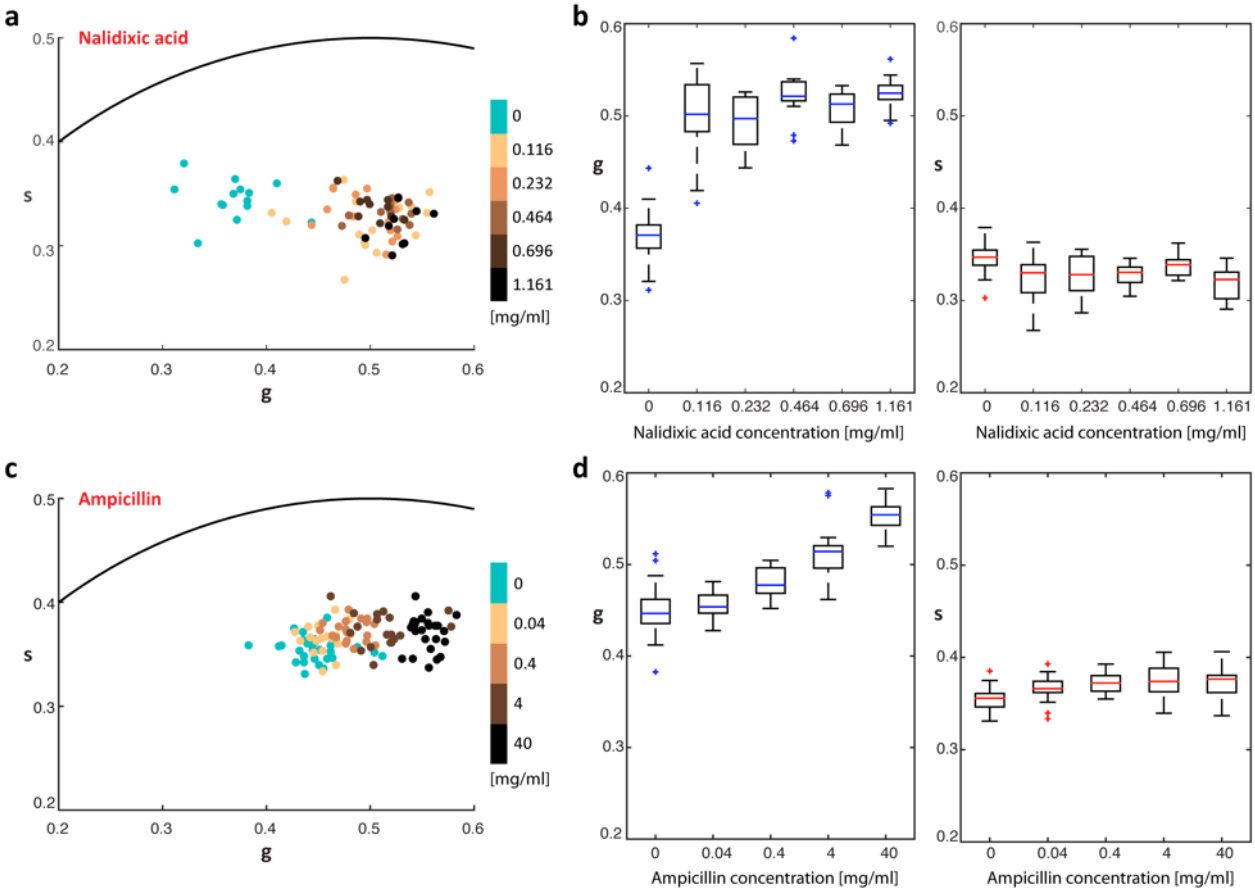

Fig. 44. Bacterial phasor response to bacteriostatic and bactericidal antibiotic treatment. (a) Bacterial phasor of *E. coli* control culture (cyan) and culture treated with increasing concentrations of a bacteriostatic antibiotic, nalidixic acid (light to dark brown). (b) Distribution of *g* and *s* within populations of cells at each concentration of nalidixic acid. (c) Bacterial phasor of *E. coli* control culture (cyan) and culture treated with increasing concentrations of bactericidal antibiotic, ampicillin (light to dark brown). (d) Distribution of *g* and *s* within populations of cells at each concentration of ampicillin.

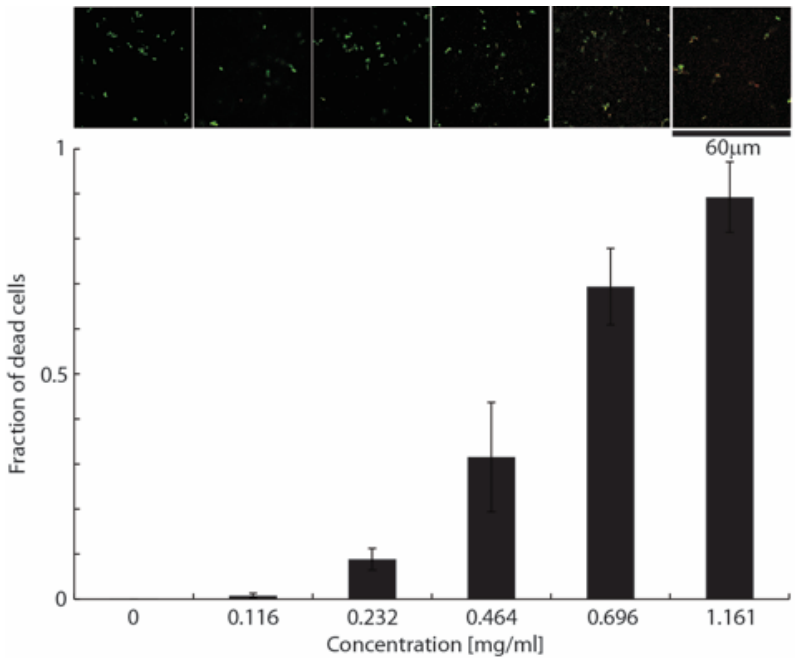

Fig. 45. Live/dead assay of cells exposed to nalidixic acid. Top panel shows representative images of *E. coli* cells stained with propidium iodide and Syto 9 after being embedded in agarose and treated with different concentrations of nalidixic acid. Red and green color represent dead and live cells respectively. Lower panel shows the fraction of dead cells in each sample from image analysis of live/dead staining.

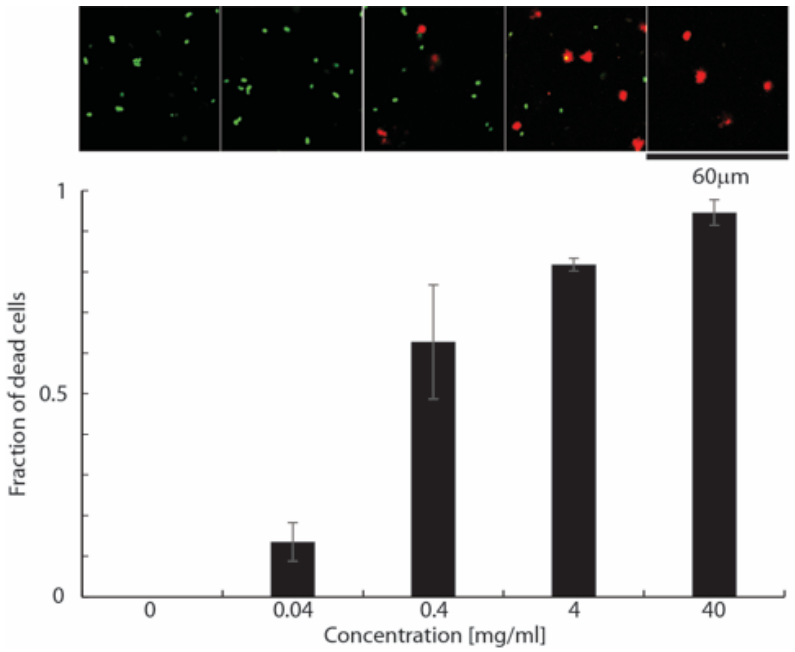

Fig. 46. Live/dead assay of cells exposed to ampicillin. Top panel shows representative images of *E. coli* cells stained with propidium iodide and Syto 9 after being embedded in agarose and treated with different concentrations of ampicillin. Red and green color represent dead and live

cells respectively. Lower panel shows the fraction of dead cells in each sample from image analysis of live/dead staining.

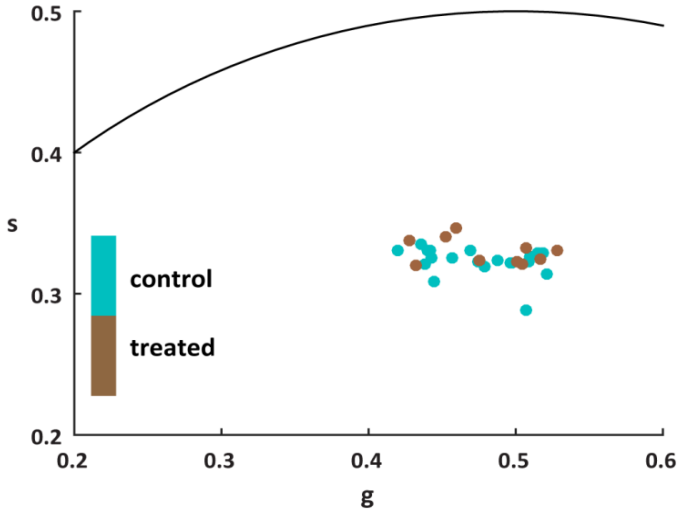

Fig. 47. Bacterial phasor of 5 h *E. coli* (control) culture and 5 h *E. coli* culture washed and incubated in water for 30 mins (treated).

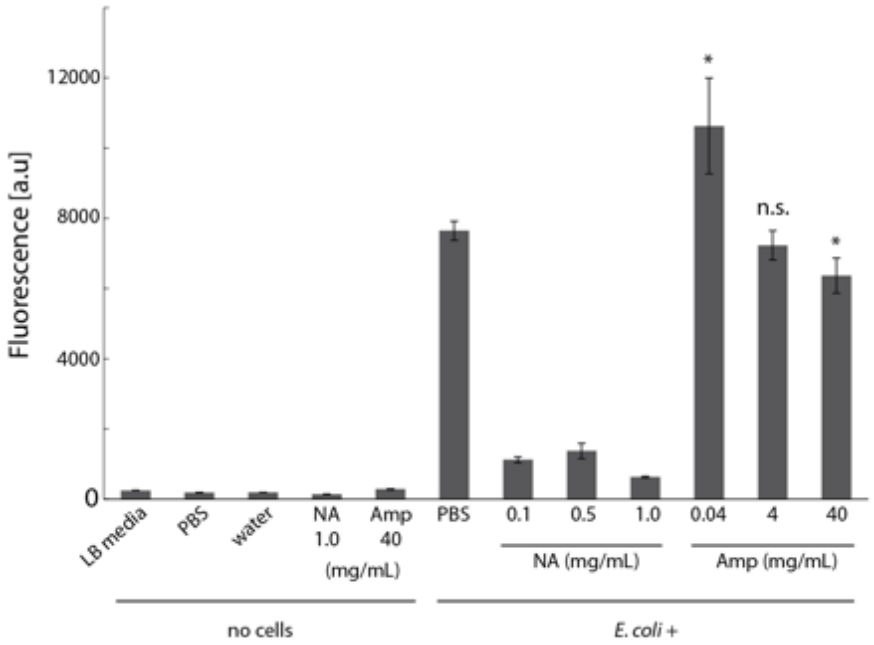

Fig. 48. Resazurin assay for measuring respiration in *E. coli* cells exposed to antibiotics. *E. coli* cells were exposed to different concentration of nalidixic acid (NA) and ampicillin (Amp) and for 30 min before injecting with resazurin to measure respiration. The fluorescence of resazurin control solutions without *E. coli* cells show low fluorescence, indicative of non-existent metabolic activity, while the control sample, *E. coli* cells exposed to PBS, shows increased fluorescence. * indicates $p < 0.05$ for comparisons of Amp treated cells to the *E. coli* + PBS control.

5.3.3. Recovery of *E. coli* cells after exposure to antibiotics

To verify whether the bacterial phasor position correlates with global metabolic activity, *E. coli* cells were allowed to recover after exposure to both antibiotics. Cells were subjected to 0.464 mg/ml nalidixic acid for 30 min and FLIM data was acquired. The cells were then washed and incubated in growth media for 30 min and imaged again. As observed in the previous section, exposure to nalidixic acid shifted the phasor to the right, indicating a higher free to bound NAD(P)H ratio (Fig. 49a and Fig. 49b). When the cells recovered in media, the phasor distribution of bacteria shifted back towards the left, indicating a lower free to bound NAD(P)H ratio. The phasor of the recovered cells shifted to significantly longer lifetimes than the initial population before exposure to nalidixic acid. Further, the phasor distribution of individual cells within the population along the *g* axis was much narrower than both the initial control and antibiotic-exposed populations (Fig. 49a and Fig. 49c).

Ampicillin treated *E. coli* displayed similar shifts in cell phasors towards shorter lifetimes (Fig. 49d and Fig. 49e). However, recovery of these cells in fresh media showed a limited shift back to smaller *g* values compared to cells recovered from nalidixic acid exposure (Fig. 49c and Fig. 49f). The number of viable cells in the ampicillin treated samples was also lower by 1.8-times compared to the initial and nalidixic acid treated cells (Fig. 50). The phasor distribution of cells in the recovered population was similar to the phasor of the cells in the initial population (Fig. 49f). In both cases, cells exposed to either antibiotic had phasors shifted more significantly along the *g* axis than along the *s* axis of the phasor plot in response to treatment (Fig. 49c and Fig. 49f). By comparing these phasor positions, changes in the ratio of free to bound NAD(P)H

within *E. coli* cells were differentiated between initial and antibiotic-exposed cells. Further, the phasor positions and distribution of the recovered populations upon recovery from bacteriostatic and bactericidal antibiotics represent distinguishing metrics captured by FLIM.

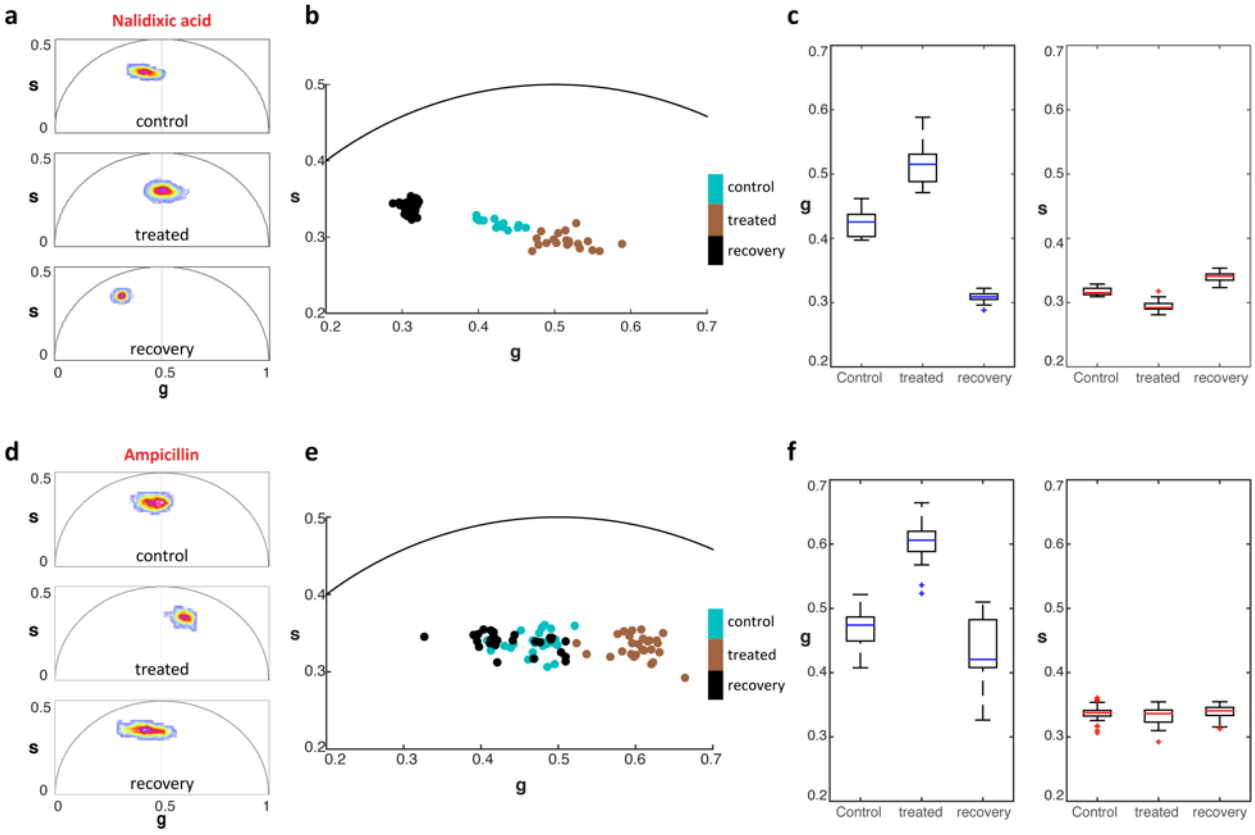

Fig. 49. Bacterial phasor response to antibiotic treatment and recovery. (a) Phasor distributions of *E. coli* (control), *E. coli* treated with 0.464 mg/ml nalidixic acid for 30 min (treated) and treated *E. coli* recovered in fresh growth medium for 30 min (recovery). (b) Bacterial phasor of control, treated and recovery groups exposed to nalidixic acid and their corresponding *g* and *s* distributions (c). (d) Phasor distributions of *E. coli* (control), *E. coli* treated with 0.4 mg/ml ampicillin for 30 min (treated) and treated *E. coli* recovered in fresh growth medium for 30 min (recovery). (e) Bacterial phasor of control, treated and recovery groups exposed to ampicillin and their corresponding *g* and *s* distributions (f).

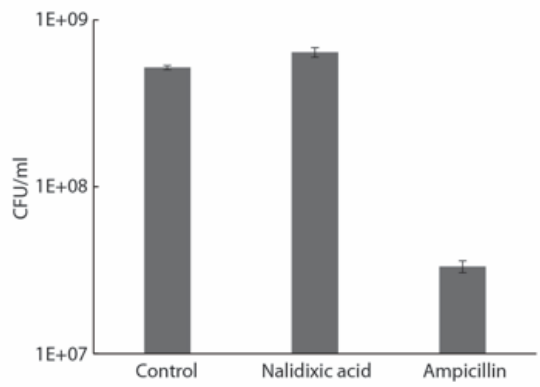

Fig. 50. Viability (CFU/ml) of *E. coli* cells plated on LB agar plated after exposure to antibiotics, nalidixic acid and ampicillin, and recovered in LB media. The control is not exposed to antibiotics.

5.3.4. Bacterial phasors as a function of culturing time

To track the change in bacterial phasor position at different growth phases, I imaged *E. coli*, *S.* Typhimurium, *P. aeruginosa* and *B. subtilis* cells from shaking cultures at varied growth times (Fig. 51a). The cell density of these bacterial cultures was tracked in parallel using optical density (OD) measurements (Fig. 51c). FLIM data was collected from shaking culture aliquots at regular intervals, starting at 2 h growth time (Fig. 52). No cells were found in the agarose-embedded samples at shorter times to acquire FLIM data. Comparing exponential phase cells, at 4 and 6 h, to the 2 h time point, all cultures except *P. aeruginosa* exhibited a shift in their mean phasor position to the right, i.e. a larger free to bound NAD(P)H ratio (Fig 51a and b). At 8 h and beyond, the mean phasor position of *E. coli*, *S.* Typhimurium, and *B. subtilis* cells shifted back to smaller values of *g* and began to oscillate, to differing degrees, along the *g* axis as cultures reached the stationary phase (Fig. 51b). In *E. coli* and *B. subtilis*, these oscillations brought the mean phasor positions to even smaller *g* values than the cultures sampled at 2 h growth. *s* positions of the mean phasor were not as sensitive as the *g* position, but tended towards larger values, also non-monotonically, with culture time. As opposed to the other three species, the

mean phasor of *P. aeruginosa* tended to smaller values in both *g* and *s*, and no oscillations were observed in *g* as a function of growth time.

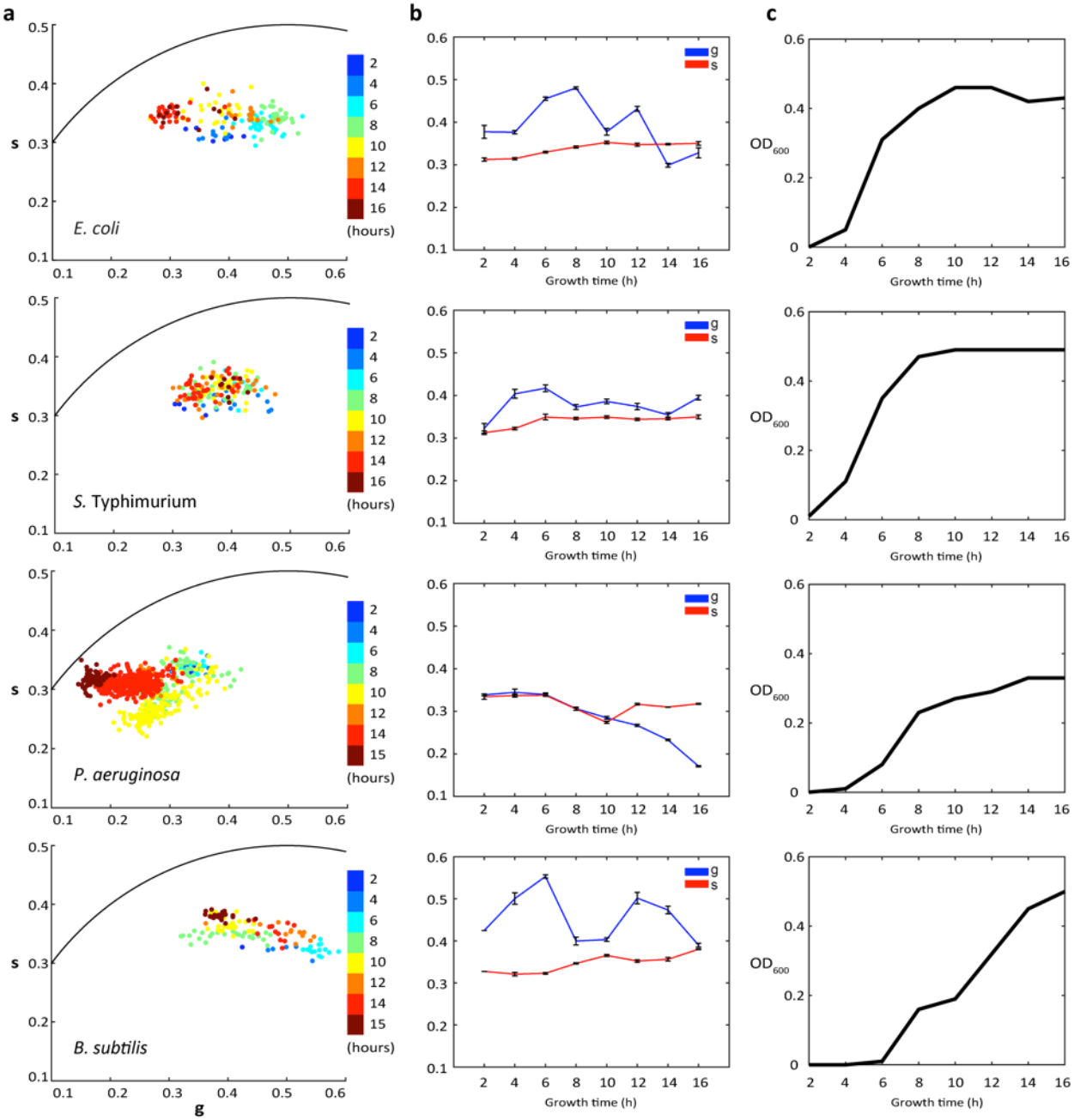

Fig. 51. The effect of growth time on the bacterial phasor. (a) Bacterial phasor fingerprint of individual *E. coli, S.* Typhimurium*, P. aeruginosa*, and *B. subtilis* cells from aliquots taken a different shaking culture growth time points. (b) Mean *g* and *s* values along the growth curve, and (c) the corresponding optical densities of the shaking cultures.

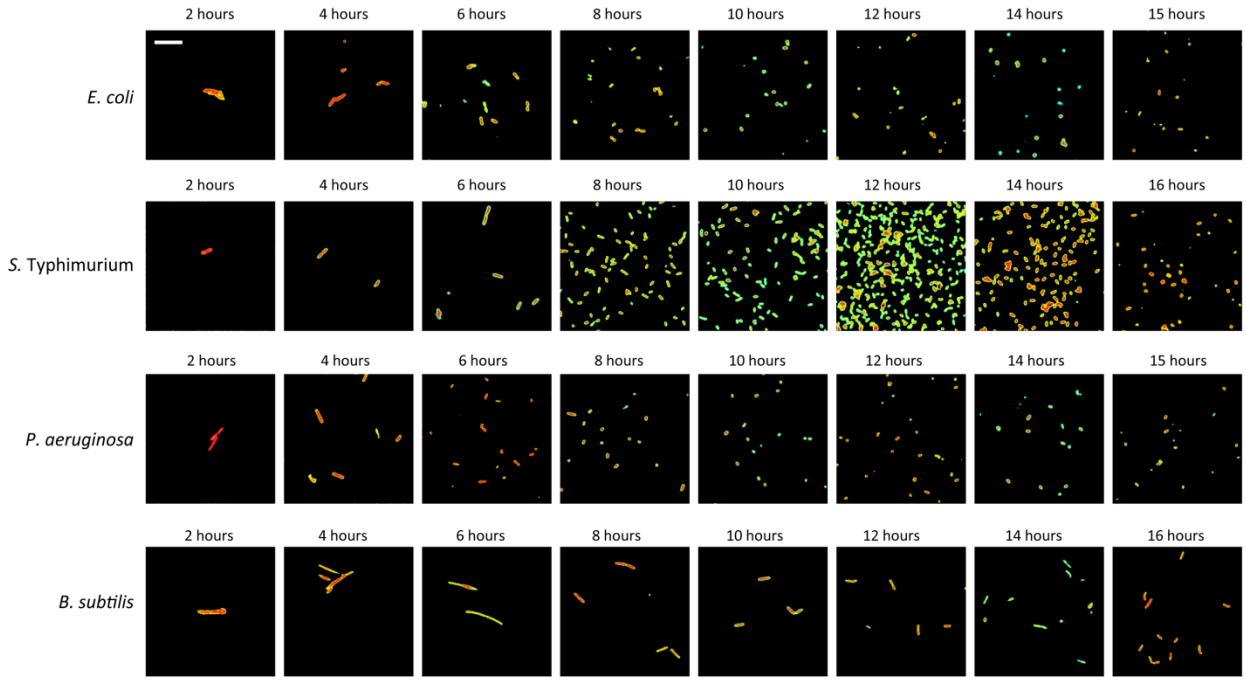

Fig. 52. Representative fluorescence intensity images of *E. coli, S.* Typhimurium*, P. aeruginosa*, *B. subtilis,* and *S. epidermidis* cells at different stages of planktonic growth. All images were obtained at the same magnification, and the scale bar is 10 μm

5.3.5. Growth recovery from extended stationary phase cultures

The FLIM phasors of *E. coli* cells grown for 15 h, 24 h, 48 h and 307 h (13 days) were compared to those grown for the same amount of time and resuspended in fresh media. Fig. 53 shows the cell phasor distribution of each of the growth time groups. I observed an increase in the ratio of free to bound NAD(P)H in the cells resuspended in fresh media when compared to their corresponding spent culture media counterparts at all time points except 13 day old cultures. The phasors of recovered cells remained at about the same position for each growth time point, but the phasors of cells taken directly from the spent culture medium shifted closer to the recovered cell phasor position with growth time. The difference in phasor position between the spent media and recovered cultures decreased with longer growth times. *E. coli* cells grown for 13 days did not show any change in their phasor position after 2 h recovery in fresh media.

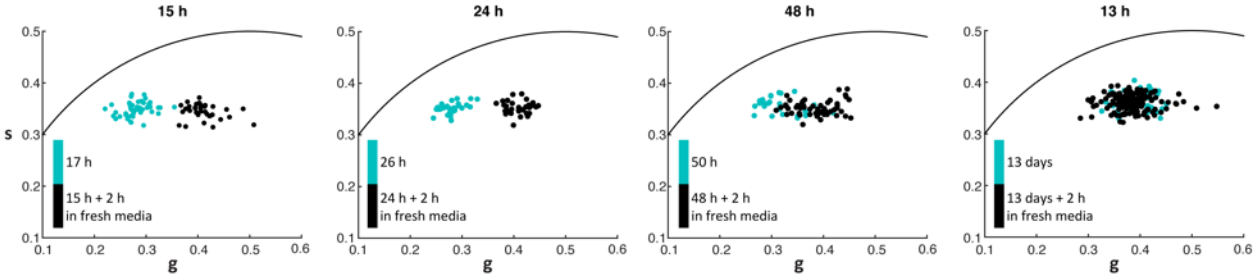

Fig. 53. Bacterial phasor recovery after late stationary phase growth. Bacterial phasor of *E. coli* cells from 15 h, 24 h, 48 h and 13 d cultures recovered for an additional 2 h in spent medium from the same culture (cyan) or fresh growth medium (black).

5.3.6. Metabolism of bacteria in biofilms on flat and post substrates.

E. coli biofilms were grown on flat and post substrates (8.1 µm) as described in chapter 4. Using the FLIM phasor technique NAD(P)H was detected in both flat and post substrates. Fig. 54 shows that biofilms on flat surface has a g value towards the center of the phasor plot and biofilms on post substrates have a g value shifted towards the left (more bound NAD(P)H). The g value of the biofilm on post substrates has a similar position as g values seen in planktonically grown cultures.

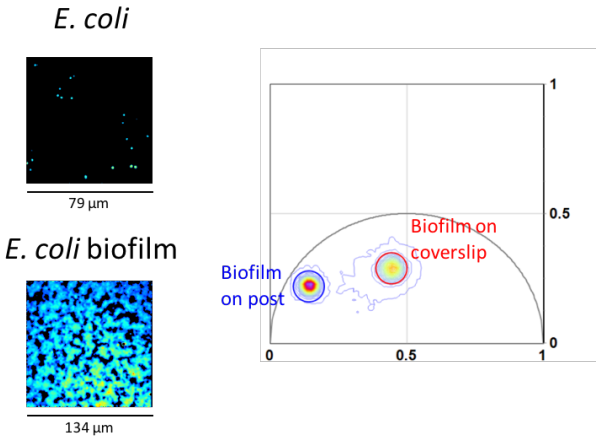

Fig. 54. Comparison of FLIM on a biofilm on post vs biofilm on flat substrates. The phasor distribution shows g values of biofilms on flat and post (8.1 µm) post substrate. On the bottom left is the intensity image of the biofilm on post and the top right shows the intensity image of E. coli cells images at 5 h growth in shaking cultures.

5.4. Discussion

In this work, I employ label-free NAD(P)H FLIM to characterize fluorescence lifetime fingerprint of bacteria with cellular resolution. The phasor approach to FLIM proves to be a powerful tool to differentiate metabolic states of bacteria via the relative quantification of free to bound NAD(P)H ratios. This ratio is expected to be related to metabolic activity, as NAD(P)+ reducing enzymes are central to catabolic pathways such as glycolysis, the citric acid cycle and the pentose phosphate pathway, which are each active in bacteria under different growth conditions. Similarly, enzymes such as NADH dehydrogenases and NAD(P)H oxidases play a central role in various anabolic pathways and show a high level of specificity in binding to NADPH or NADH [254–256].

NAD(P)H FLIM of *E. coli, P. aeruginosa, B. subtilis, S.* Typhimurium and *S. epidermidis* was used to generate the bacterial species fingerprint phasors as well as those for the antibiotic experiments. I observed small variations between phasors of control population of *E. coli* even when grown under same conditions and harvested at the same time and OD, perhaps due to normal metabolic variability (Fig. 55). The phasor fingerprint exhibits a distribution of values of individual cells within a population of same species (Fig. 42b and 42c). These differences suggest a distribution of metabolic activity within and between species populations at the same time of growth. The observed diversity of phasor positions may be a result of varying rates of NAD(P)+/NAD(P)H reduction/oxidation and shifts in NAD(P)H utilization due to catabolic and anabolic adaptations [236,237,257,258].

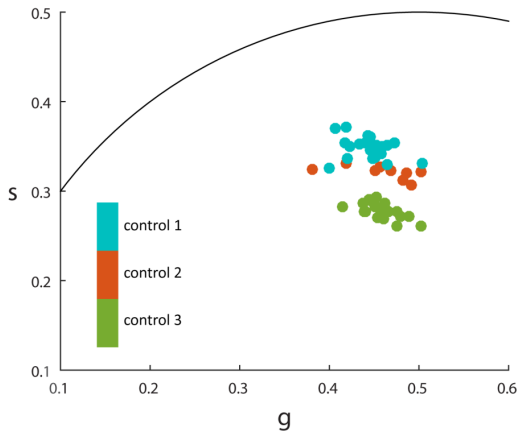

Fig. 55. Bacterial phasors of *E. coli* cells from three independent 5 h cultures grown on different days.

The shift of the NAD(P)H phasor position towards shorter lifetimes in response to antibiotic exposure suggests a decrease in enzyme binding of NAD(P)H, indicated by a larger free to bound ratio. In case of bacteriostatic antibiotics this shift tracks with lower respiration activity indicated by the resazurin assay (Fig. 48). These results are consistent with previously reported data [250,259] which suggest that bacteriostatic antibiotics induce lower oxygen consumption rates (OCR) in cultures by arresting respiration in cells. The increase in respiration activity at low ampicillin concentrations, on the other hand, is consistent with findings that OCR increases upon exposure to bactericidal antibiotics [250,259]. While the effects of higher concentrations of ampicillin on respiration have not been studied, to our knowledge, the resazurin and NAD(P)H FLIM data both show a shift to a more reducing environment and an increase in the free to bound NAD(P)H ratio in the phasor plots, respectively.

In the event of cell death, the metabolic state is irreversible; however bacterial cells are known to recover from a state of static growth and dormancy induced by bacteriostatic compounds[213,250,251,260]. The observed return of the mean phasor position to the left of the plot

when nalidixic acid was washed away from the *E. coli* cells (Fig. 49a and 49b) is consistent with these previous results. In addition to the shift in the mean phasor, the distribution of single-cell phasors about the mean in the recovered population exposed to nalidixic acid was much narrower than the control and treated populations (Fig. 49c). In the context of the above results, the decrease in phasor variance indicates a recovery to a relatively homogeneous metabolic state throughout the population, as compared to the initial and nalidixic acid-treated populations, which exhibit a greater spread in NAD(P)H lifetimes.

In contrast to the recovery results from nalidixic acid, the phasor distribution of cells treated with ampicillin and recovered in fresh medium was less pronounced and much broader (Fig. 49d). This phasor data was acquired from a population of cells that did not lyse as a result of the ampicillin treatment, so the extent of phasor recovery is of a biased population and characteristic only of cells that survived the treatment. Indeed, the density of cells that survived this treatment was 19.1 times lower than the nalidixic acid treatment (Fig. 50). In addition, the phasor of the recovered cell population was much broader than that of cells recovered from nalidixic acid treatment, indicating more metabolic heterogeneity. The response of bacteria to high-stress environments depends on a range of factors, such as the rate of cell division and initial metabolic states[55,213,261–263]. Such factors can direct the fate of part of the population towards persister or dormant states and the rest towards death. Exposure to bactericidal antibiotics also results in generation of reactive oxygen species [264,265] and broad, and ultimately toxic, changes to the activity of central metabolic pathways in *E. coli* [259,265]. Consequently, the bactericidal effects of ampicillin, in contrast to nalidixic acid, may result in a population with the diversity of metabolic states observed in the recovered populations.

The metabolism of bacterial population vary drastically over time resulting in a collection of different metabolic states that cannot be captured by optical density measurements alone[266–268]. In the case of aerobically grown bacteria, these variations depend on the type of nutrient source, temperature of growth, and rate of aeration, among others. Moreover, the bacterial growth curve extends beyond the conventional lag, exponential and stationary phases of growth[269–271]. Many interesting physiological phenomena occur during late stationary phase growth, such as the emergence of persister cells and growth advantage in stationary phase (GASP) phenotypes, changes in gene expression and cell morphology, and programmed cell death[55,271–274]. Most importantly each bacterium within the population may experience different metabolic and growth rates compared to neighboring cells, yet this information cannot be obtained by cell density measurement or CFU counts.

I employed NAD(P)H FLIM phasor to characterize the metabolic states of 4 bacterial species at different stages of growth (Fig. 51a). The earliest time point, 2 h, is already near the end of the lag phase for these cultures. The mean phasor positions of *E. coli*, *S.* Typhimurium, and *B. subtilis* all begin at relatively small *g* values. In comparison with observed phasors from the antibiotic exposure and recover experiments, these smaller *g* values suggest a greater metabolic activity. As cells enter their exponential phase, their phasors shift right to larger *g* values, consistent with a ramp down of metabolic rates as previously determined via indirect methods[267,268]. At 8-10 h growth, this phasor trend reverses for these three cultures, suggesting an additional metabolic transition commensurate with the change in growth rate as cultures enter the stationary phase. In the stationary phase, their phasor positions shift back and forth in *g* in a manner seemingly unrelated to the cell density (Fig. 51b and Fig. 56). Bacterial cultures display an oscillatory behavior of cell density in the culture with rise and fall during the stationary phase

due to GASP phenotypes[272,274,275], but these typically occur at late stationary phase growth, and the observed phasor shifts are not directly correlated with cell density. Instead, these results indicate that the NAD(P)H phasor is sensitive to metabolic changes within the cells not captured by cell density or CFU analyses.

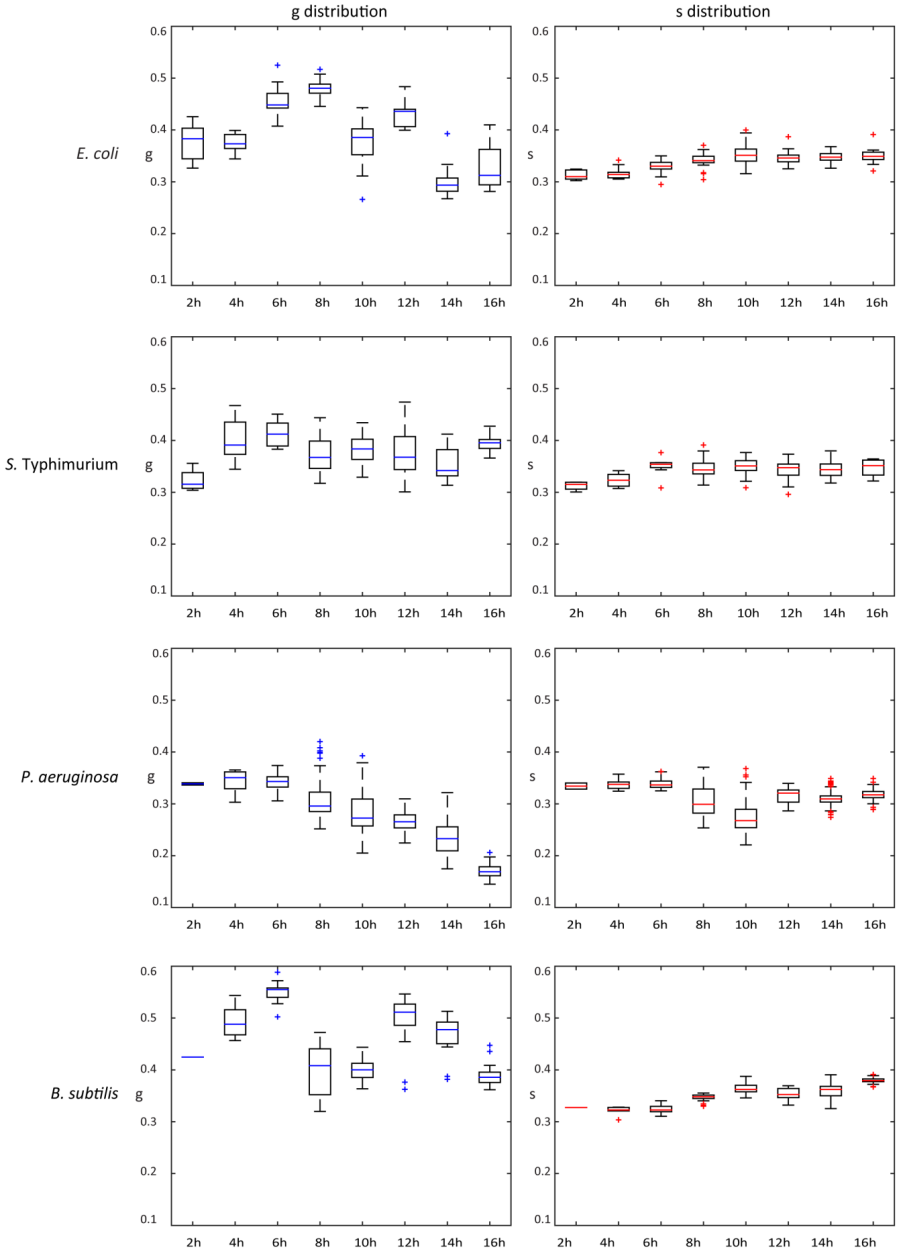

Fig. 56. *g* and *s* distributions of *E. coli, S.* Typhimurium, *P. aeruginosa*, *B. subtilis,* and *S. epidermidis* populations at different time points on the growth curve.

To look at metabolic adaptations in the stationary phase cultures, FLIM data was obtained from *E. coli* cultures grown for 15 h, 24 h, 48 h, and 13 d (Fig. 53). Interestingly, cells grown for an additional 2 h in the spent culture medium from 15, 24, and 48 h cultures had phasors at longer lifetimes than the early and mid-exponential phase cells in Figures 1-4 ($g \sim 0.4$). The NAD(P)H lifetimes in these populations were also longer than those of cells from those same cultures that recovered for an additional 2 h in fresh growth medium, which were themselves consistent with early exponential phase *E. coli* cells (Fig. 51), suggesting a growth recovery. The difference in mean phasor position between cells recovered in fresh and spent medium, however, shrinks with increasing culture time at 48 h and 13 d, indicating a diminished capacity of these bacteria to recover (Fig. 57). Indeed, cells from the 13 d culture did not show any recovery, suggesting that most cells are dead or in a phenotypic state with an extended lag time to exponential growth. Future experiments will focus on FLIM and independent metabolic rate measurement in late stationary phase cultures.

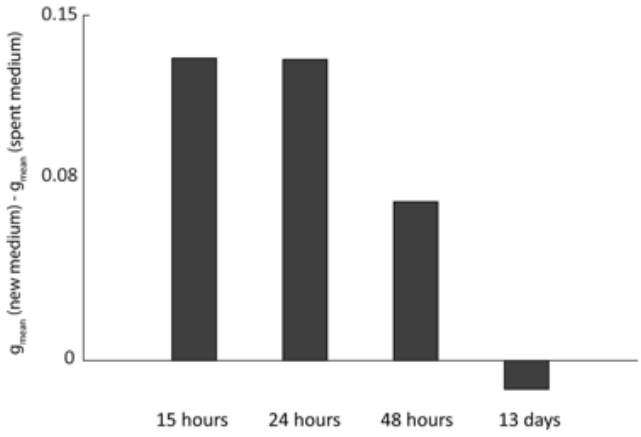

Fig. 57. Differences between mean *g* (g_{mean}) of the bacterial phasor distributions of 15 h, 24 h, 48 h, and 13 d *E. coli* cultures incubated in fresh media for 2 h compared to those incubated for a further 2 h in their spent media.

5.5. Conclusion

In conclusion, I have demonstrated a label-free, two-photon FLIM method for tracking changes in bacterial metabolism. The results in this chapter, represent the first NAD(P)H FLIM phasor fingerprinting of various bacterial species, and they indicate that the NAD(P)H fluorescence lifetime, as captured in the phasor position, is sensitive to changes in metabolic states within cell populations. The NAD(P)H phasor of cells exposed to antibiotics exhibited the expected shifts due to diminished metabolic capacity, as well as detecting the metabolic recovery of cells resistant or tolerant to ampicillin exposure. The distribution of cell phasors within a population also changes as a function of treatment conditions, providing unique insight into single-cell and community behavior. Lastly, NAD(P)H FLIM of bacteria from planktonic cultures exhibited changes in the phasors that did not track with cell density, indicating that this technique can provide additional information about cell metabolism beyond what is inferred from conventional growth rate measurements. Extending on the single cell FLIM, I use the FLIM phasor technique to show that bacteria within biofilms on post substrates have different metabolic states than bacteria in biofilms on flat substrates. This work demonstrates the power of NAD(P)H FLIM to track metabolic states of individual bacteria *in situ*, and that the bacterial phasor represents a unique and complimentary set of data to conventional metabolism and growth characterization results.

Chapter 6.

Conclusions and future work

Biofilms are problematic in medical settings because they cause chronic infections that persist for very long time and have a significantly high antibiotic resistance relative to their planktonic counterparts [1]. Treating biofilm associated infections are difficult and this has inspired a lot of research into different dispersal and prevention strategies against biofilms of infectious microorganisms [276]. Most of the current research is directed at understanding signaling processes and interaction between microorganisms living within the community, which show that interaction between bacteria drives community structure and organization. It is essential to understand these processes, to derive treatment strategies based on them. However, most anti-biofilm strategies developed to date are not permanent. In this thesis, I describe inhibition and dispersal of pathogenic bacteria and, how microstructures can be used to manipulate a signaling pathway. Finally, I also demonstrate a label free and non-invasive technique to study metabolic states of bacteria in planktonic and biofilm environment.

I first demonstrated an *in vitro* biofilm competition model of a probiotic bacterium, *E. coli* Nissle 1917 with *Salmonella* Typhimurium. Iron based interaction between EcN and STm has been demonstrated before in murine model and planktonic cultures [99]. This chapter shows that biofilm based interaction can be used to achieve the similar outcome as animal models and in much less time. Use of microfluidics technology to understand these interactions demonstrate for the first time, that microcins require to be in a constant concentration to inhibit enteric pathogen growth and microcin based inhibition of STm by EcN is not contact dependent. This information is an important contribution towards the existing siderophore-peptide inhibition

models, and has great implications for developing therapeutics against STm infections in the future. Further, we also show that microcin-based inhibition model is not limited to STm biofilm inhibition, but also applies to other gut pathogens. The *in vitro* biofilm models coupled with microfluidics technology can be used to develop screens for potential anti-biofilm compounds in gut communities by studying the interaction of bacteria living in these communities. In the case of EcN-STm cocultures, microcin mediated biofilm inhibition of STm is not contact dependent and therefore, does not require the producing microorganism to be present. Several other microcins, such as microcin V, c7, J25, E492, are used to target gut microorganisms in an iron starved environment [109,277,278]. Using microfluidics devices as demonstrated in the chapter, the efficacy of different microcins can be tested against enteric pathogens.

The second chapter in the thesis describes a novel biofilm dispersal pathway in the bacterium *E. coli* providing indirect evidence as to why *P. aeruginosa* and *E. coli* are not found in cocultures in nature. The *E. coli – P. aeruginosa* biofilm dispersal model adds to a short list of interspecies dispersal triggers and rhamnolipids represents a new mechanism of modulating interspecies signaling. We also demonstrate the ability of a biosurfactant, rhamnolipids, to permeabilize the cell membrane to other signaling compounds and metabolites. The homoserine lactone, 3oxoC12HSL has been shown to inhibit *E. coli* biofilms, and it is speculated that 3 oxoC12HSL binds the SdiA receptor in *E. coli*. However, it is not clear if binding of 3oxoC12HSL is the dispersal trigger for *E. coli*. Investigating the dispersal pathway in *E. coli* could be a topic of future research, which could potentially unravel new targets for therapies against *E. coli* infections. The dispersal solution described in chapter 2, recapitulates the full dispersal observed using *P. aeruginosa* supernatant, but the timescale of the dispersal response is longer than that of the *P. aeruginosa* supernatant. The difference in dispersal time between P.

aeruginosa supernatant and the dispersal solution begs the question if there are other compounds involved in facilitating this dispersal pathway. *E. coli* cells exposed to *P. aeruginosa* supernatant have a lower CFU count than *E. coli* cells exposed to dispersal solutions, which shows presence of other toxins in the *P. aeruginosa* supernatant that cause *E. coli* cell death. Investigating these compounds, that facilitates the dispersal process or cause cell death in *E. coli* could better our understanding of dispersal mechanisms in *E. coli* biofilms. Further, the work in this chapter opens the possibilities of existence of rhamnolipids or biosurfactant based signaling processes, which has never been investigated before. Biosurfactant producing microorganisms like *Bacillus subilis* and *Staphylococcus xylosus* are of great interest because biosurfactants like rhamnoipids exhibit antibiotic activity against microorganisms [279–282]. Certain Biosurfactants also disperse biofilms of other bacteria. In the chapter 3, I show that the biosurfactant, rhamnolipid assist in uptake of hydrophobic signaling molecules. The potential role of biosurfactants in signaling pathways and interspecies interaction can be a topic of future research.

The third chapter probes a more recent sub-field in biofilm research and engineering, which focuses on imposing spatial organization in biofilms using more permanent means rather than surface functionalization techniques. We demonstrate that physical microstructures change *E. coli* biofilm morphology, changing the microenvironment surrounding each cell by increasing the concentration of metabolites within the biofilm. An increase in indole concentration switches the dispersal pathway in *E. coli* and inhibits *P. aeruginosa* biofilm growth on post substrates with mature *E. coli* biofilms. These results also represent, the first demonstration of *P. aeruginosa* biofilm inhibition by the metabolite indole. Further, this work also demonstrates interaction between two species of bacteria that do not coexist in nature and opens the possibilities of existence of similar pathways.

Indole is considered as an interspecies signaling molecule and this study does not show how indole inhibits *P. aeruginosa* biofilm formation, which could be a topic of further research. The posts also induce changes in the biofilm morphology, which may be due to change in the quantity and chemical composition of the biofilm matrix. Further, the post substrates confer antibiotic susceptibility to biofilms, which is related to the change in metabolism of bacteria on post substrates, as demonstrated in the fifth chapter of this thesis. The change in metabolic state of *E. coli* biofilms on posts could be due to change of the microenvironment within the biofilms induced by the increase in metabolite concentration. To understand these metabolic changes in *E. coli,* we develop a new method to study bacterial metabolic states.

The final study in this thesis is to develop a new method to study metabolic states of bacteria in clinical and lab samples. We use the FLIM phasor approach to study metabolism of bacteria in planktonic growth environments and biofilms. This technique is label free and non-invasive and can be used to study bacteria in any environment *in situ* without further processing of the samples. FLIM phasor approach has never been extensively used to study metabolism of bacteria. We study metabolic states of five different species of bacteria, *E. coli*, *P. aeruginosa*, *Staphyloccocus epidermidis*, *S. Typhimurium* and *Bacillus subtilis* to show that this technique can be used to study metabolism of bacteria. We further demonstrate, that FLIM phasor approach can detect different metabolic states in bacteria using antibiotic assays and growth curves. The FLIM phasor approach is benchmarked with standard techniques, such as CFU studies and resazurin assays, which are conventionally associated with metabolism studies. Nevertheless, this technique needs to be further developed to study metabolic fluxes in bacteria exposed to different environments such as antibiotic, oxidizers, change in temperature. The metabolic flux studies can be done using isotope labelled carbon sources so that these samples can be studied

with mass spectroscopy [283,284] in conjunction with FLIM. These studies will help benchmark this new technique and the FLIM phasor technique can be used as a standalone technique to track bacteria metabolism in different environment.

Biofilms have evolved significantly increased resistance to existing therapies for biofilm associated infections, severely hampering the successful treatment of biofilm-associated infections. The increased antimicrobial resistance results from the simultaneous operation of multiple biofilm-specific mechanisms that are still not fully understood. Deeper understanding of these mechanisms will be useful for the development of new anti-biofilm agents, from which innovative therapeutic measures may be developed to eradicate persistent infections. This thesis is a step forward in facilitating the development of such anti-biofilm strategies.

Bibliography

1. Donlan, R. M. Biofilms and device-associated infections. *Emerg. Infect. Dis.* **7,** 277–281 (2001).
2. Watnick, P. I. & Kolter, R. Steps in the development of a Vibrio cholerae El Tor biofilm. *Mol. Microbiol.* **34,** 586–595 (1999).
3. Danese, P. N., Pratt, L. A. & Kolter, R. Exopolysaccharide Production Is Required for Development of Escherichia coli K-12 Biofilm Architecture. *J. Bacteriol.* **182,** 3593–3596 (2000).
4. Flemming, H.-C. & Wingender, J. The biofilm matrix. *Nat. Rev. Microbiol.* **8,** 623–633 (2010).
5. van Gestel, J., Vlamakis, H. & Kolter, R. Division of Labor in Biofilms: the Ecology of Cell Differentiation. *Microbiol. Spectr.* **3,** MB-0002-2014 (2015).
6. Gestel, J. van, Vlamakis, H. & Kolter, R. Division of Labor in Biofilms: the Ecology of Cell Differentiation. *Microbiol. Spectr.* **3,** (2015).
7. Gordon, M. A. Salmonella infections in immunocompromised adults. *J. Infect.* **56,** 413–422 (2008).
8. Hall-Stoodley, L., Costerton, J. W. & Stoodley, P. Bacterial biofilms: from the Natural environment to infectious diseases. *Nat. Rev. Microbiol.* **2,** 95–108 (2004).
9. Persat, A. *et al.* The Mechanical World of Bacteria. *Cell* **161,** 988–997 (2015).
10. Fenchel, T. Microbial behavior in a heterogeneous world. *Science* **296,** 1068–1071 (2002).
11. Kim, J., Hegde, M., Kim, S. H., Wood, T. K. & Jayaraman, A. A microfluidic device for high throughput bacterial biofilm studies. *Lab. Chip* **12,** 1157–1163 (2012).

12. Yawata, Y., Nguyen, J., Stocker, R. & Rusconi, R. Microfluidic Studies of Biofilm Formation in Dynamic Environments. *J. Bacteriol.* **198,** 2589–2595 (2016).
13. Crouzet, M. *et al.* Exploring early steps in biofilm formation: set-up of an experimental system for molecular studies. *BMC Microbiol.* **14,** 253 (2014).
14. Lambert, G., Bergman, A., Zhang, Q., Bortz, D. & Austin, R. Physics of biofilms: the initial stages of biofilm formation and dynamics. *New J. Phys.* **16,** 45005 (2014).
15. Costerton, J. W., Lewandowski, Z., Caldwell, D. E., Korber, D. R. & Lappin-Scott, H. M. Microbial biofilms. *Annu. Rev. Microbiol.* **49,** 711–745 (1995).
16. Sandt, C., Smith-Palmer, T., Pink, J., Brennan, L. & Pink, D. Confocal Raman microspectroscopy as a tool for studying the chemical heterogeneities of biofilms in situ. *J. Appl. Microbiol.* **103,** 1808–1820 (2007).
17. Worlitzsch, D. *et al.* Effects of reduced mucus oxygen concentration in airway Pseudomonas infections of cystic fibrosis patients. *J. Clin. Invest.* **109,** 317–325 (2002).
18. Walters, M. C., Roe, F., Bugnicourt, A., Franklin, M. J. & Stewart, P. S. Contributions of antibiotic penetration, oxygen limitation, and low metabolic activity to tolerance of Pseudomonas aeruginosa biofilms to ciprofloxacin and tobramycin. *Antimicrob. Agents Chemother.* **47,** 317–323 (2003).
19. Kaplan, J. B. Biofilm dispersal: mechanisms, clinical implications, and potential therapeutic uses. *J. Dent. Res.* **89,** 205–218 (2010).
20. Kaplan, J. B. Biofilm Dispersal. *J. Dent. Res.* **89,** 205–218 (2010).
21. Kostakioti, M., Hadjifrangiskou, M. & Hultgren, S. J. Bacterial Biofilms: Development, Dispersal, and Therapeutic Strategies in the Dawn of the Postantibiotic Era. *Cold Spring Harb. Perspect. Med.* **3,** (2013).

22. Klausen, M., Aaes-Jørgensen, A., Molin, S. & Tolker-Nielsen, T. Involvement of bacterial migration in the development of complex multicellular structures in Pseudomonas aeruginosa biofilms. *Mol. Microbiol.* **50,** 61–68 (2003).

23. Sauer, K., Camper, A. K., Ehrlich, G. D., Costerton, J. W. & Davies, D. G. Pseudomonas aeruginosa displays multiple phenotypes during development as a biofilm. *J. Bacteriol.* **184,** 1140–1154 (2002).

24. Rowe, M. C., Withers, H. L. & Swift, S. Uropathogenic Escherichia coli forms biofilm aggregates under iron restriction that disperse upon the supply of iron. *FEMS Microbiol. Lett.* **307,** 102–109 (2010).

25. Sauer, K. *et al.* Characterization of Nutrient-Induced Dispersion in Pseudomonas aeruginosa PAO1 Biofilm. *J. Bacteriol.* **186,** 7312–7326 (2004).

26. Manefield, M. & Turner, S. L. Quorum sensing in context: out of molecular biology and into microbial ecology. *Microbiol. Read. Engl.* **148,** 3762–3764 (2002).

27. Lerat, E. & Moran, N. A. The evolutionary history of quorum-sensing systems in bacteria. *Mol. Biol. Evol.* **21,** 903–913 (2004).

28. Elias, S. & Banin, E. Multi-species biofilms: living with friendly neighbors. *FEMS Microbiol. Rev.* **36,** 990–1004 (2012).

29. Rendueles, O. & Ghigo, J.-M. Multi-species biofilms: how to avoid unfriendly neighbors. *FEMS Microbiol. Rev.* **36,** 972–989 (2012).

30. Taga, M. E. & Bassler, B. L. Chemical communication among bacteria. *Proc. Natl. Acad. Sci. U. S. A.* **100 Suppl 2,** 14549–14554 (2003).

31. Fuqua, C., Parsek, M. R. & Greenberg, E. P. Regulation of gene expression by cell-to-cell communication: acyl-homoserine lactone quorum sensing. *Annu. Rev. Genet.* **35,** 439–468 (2001).

32. Tomasz, A. Control of the Competent State in Pneumococcus by a Hormone-Like Cell Product: An Example for a New Type of Regulatory Mechanism in Bacteria. *Nature* **208,** 155–159 (1965).

33. Lupp, C. & Ruby, E. G. Vibrio fischeri Uses Two Quorum-Sensing Systems for the Regulation of Early and Late Colonization Factors. *J. Bacteriol.* **187,** 3620–3629 (2005).

34. Ng, W.-L. & Bassler, B. L. Bacterial Quorum-Sensing Network Architectures. *Annu. Rev. Genet.* **43,** 197–222 (2009).

35. Lee, J. & Zhang, L. The hierarchy quorum sensing network in Pseudomonas aeruginosa. *Protein Cell* **6,** 26–41 (2015).

36. Lee, J. *et al.* A cell-cell communication signal integrates quorum sensing and stress response. *Nat. Chem. Biol.* **9,** 339–343 (2013).

37. Atkinson, S., Throup, J. P., Stewart, G. S. & Williams, P. A hierarchical quorum-sensing system in Yersinia pseudotuberculosis is involved in the regulation of motility and clumping. *Mol. Microbiol.* **33,** 1267–1277 (1999).

38. Federle, M. J. & Bassler, B. L. Interspecies communication in bacteria. *J. Clin. Invest.* **112,** 1291–1299 (2003).

39. Ryan, R. P. & Dow, J. M. Diffusible signals and interspecies communication in bacteria. *Microbiol. Read. Engl.* **154,** 1845–1858 (2008).

40. Nadell, C. D., Drescher, K. & Foster, K. R. Spatial structure, cooperation and competition in biofilms. *Nat. Rev. Microbiol.* **14,** 589–600 (2016).

41. Liu, W. *et al.* Interspecific Bacterial Interactions are Reflected in Multispecies Biofilm Spatial Organization. *Front. Microbiol.* **7,** (2016).

42. Miller, M. B. & Bassler, B. L. Quorum sensing in bacteria. *Annu. Rev. Microbiol.* **55,** 165–199 (2001).

43. Wimpenny, J., Manz, W. & Szewzyk, U. Heterogeneity in biofilms. *FEMS Microbiol. Rev.* **24,** 661–671 (2000).

44. Rao, D., Webb, J. S. & Kjelleberg, S. Competitive Interactions in Mixed-Species Biofilms Containing the Marine Bacterium Pseudoalteromonas tunicata. *Appl. Environ. Microbiol.* **71,** 1729–1736 (2005).

45. Nadell, C. D., Foster, K. R. & Xavier, J. B. Emergence of Spatial Structure in Cell Groups and the Evolution of Cooperation. *PLoS Comput Biol* **6,** e1000716 (2010).

46. Hong, S. H. *et al.* Synthetic quorum-sensing circuit to control consortial biofilm formation and dispersal in a microfluidic device. *Nat. Commun.* **3,** 613 (2012).

47. Römling, U. & Balsalobre, C. Biofilm infections, their resilience to therapy and innovative treatment strategies. *J. Intern. Med.* **272,** 541–561 (2012).

48. Hannan, T. J. *et al.* Host-pathogen checkpoints and population bottlenecks in persistent and intracellular uropathogenic Escherichia coli bladder infection. *FEMS Microbiol. Rev.* **36,** 616–648 (2012).

49. Costerton, J. W., Stewart, P. S. & Greenberg, E. P. Bacterial biofilms: a common cause of persistent infections. *Science* **284,** 1318–1322 (1999).

50. Høiby, N., Ciofu, O. & Bjarnsholt, T. Pseudomonas aeruginosa biofilms in cystic fibrosis. *Future Microbiol.* **5,** 1663–1674 (2010).

51. Deriu, E. *et al.* Probiotic Bacteria Reduce Salmonella Typhimurium Intestinal Colonization by Competing for Iron. *Cell Host Microbe* **14,** 26–37 (2013).

52. Mah, T.-F. *et al.* A genetic basis for Pseudomonas aeruginosa biofilm antibiotic resistance. *Nature* **426,** 306–310 (2003).

53. James, G. A. *et al.* Biofilms in chronic wounds. *Wound Repair Regen. Off. Publ. Wound Heal. Soc. Eur. Tissue Repair Soc.* **16,** 37–44 (2008).

54. Chiang, W.-C. *et al.* Extracellular DNA Shields against Aminoglycosides in Pseudomonas aeruginosa Biofilms. *Antimicrob. Agents Chemother.* **57,** 2352–2361 (2013).

55. Balaban, N. Q., Merrin, J., Chait, R., Kowalik, L. & Leibler, S. Bacterial Persistence as a Phenotypic Switch. *Science* **305,** 1622–1625 (2004).

56. García-Contreras, R., Maeda, T. & Wood, T. K. Resistance to Quorum-Quenching Compounds. *Appl. Environ. Microbiol.* **79,** 6840–6846 (2013).

57. Chan, B. K. & Abedon, S. T. Bacteriophages and their enzymes in biofilm control. *Curr. Pharm. Des.* **21,** 85–99 (2015).

58. Harper, D. R. *et al.* Bacteriophages and Biofilms. *Antibiotics* **3,** 270–284 (2014).

59. Gutiérrez, D., Rodríguez-Rubio, L., Martínez, B., Rodríguez, A. & García, P. Bacteriophages as Weapons Against Bacterial Biofilms in the Food Industry. *Front. Microbiol.* **7,** (2016).

60. Dror, N., Mandel, M., Hazan, Z. & Lavie, G. Advances in Microbial Biofilm Prevention on Indwelling Medical Devices with Emphasis on Usage of Acoustic Energy. *Sensors* **9,** 2538–2554 (2009).

61. Oppenheimer-Shaanan, Y., Steinberg, N. & Kolodkin-Gal, I. Small molecules are natural triggers for the disassembly of biofilms. *Trends Microbiol.* **21,** 594–601 (2013).

62. LaSarre, B. & Federle, M. J. Exploiting Quorum Sensing To Confuse Bacterial Pathogens. *Microbiol. Mol. Biol. Rev. MMBR* **77,** 73–111 (2013).

63. Schlafer, S. & Meyer, R. L. Confocal microscopy imaging of the biofilm matrix. *J. Microbiol. Methods* (2016). doi:10.1016/j.mimet.2016.03.002

64. Harrison, J. J. *et al.* The use of microscopy and three-dimensional visualization to evaluate the structure of microbial biofilms cultivated in the Calgary Biofilm Device. *Biol. Proced. Online* **8,** 194–215 (2006).

65. Cerca, N., Gomes, F., Pereira, S., Teixeira, P. & Oliveira, R. Confocal laser scanning microscopy analysis of S. epidermidis biofilms exposed to farnesol, vancomycin and rifampicin. *BMC Res. Notes* **5,** 244 (2012).

66. Bjarnsholt, T., Ciofu, O., Molin, S., Givskov, M. & Høiby, N. Applying insights from biofilm biology to drug development — can a new approach be developed? *Nat. Rev. Drug Discov.* **12,** 791–808 (2013).

67. Khajotia, S. S., Smart, K. H., Pilula, M. & Thompson, D. M. Concurrent Quantification of Cellular and Extracellular Components of Biofilms. *J. Vis. Exp. JoVE* (2013). doi:10.3791/50639

68. Heydorn, A. *et al.* Quantification of biofilm structures by the novel computer program COMSTAT. *Microbiol. Read. Engl.* **146 (Pt 10),** 2395–2407 (2000).

69. Watrous, J. D. & Dorrestein, P. C. Imaging mass spectrometry in microbiology. *Nat. Rev. Microbiol.* **9,** 683–694 (2011).

70. Dunham, S. J. B., Ellis, J. F., Li, B. & Sweedler, J. V. Mass Spectrometry Imaging of Complex Microbial Communities. *Acc. Chem. Res.* **50,** 96–104 (2017).

71. Brauer, J. I. *et al.* Mass spectrometric metabolomic imaging of biofilms on corroding steel surfaces using laser ablation and solvent capture by aspiration. *Biointerphases* **10,** 19003 (2015).

72. Fang, J. & Dorrestein, P. C. Emerging mass spectrometry techniques for the direct analysis of microbial colonies. *Curr. Opin. Microbiol.* **0,** 120–129 (2014).

73. Post, D. M. *et al.* Comparative analyses of proteins from Haemophilus influenzae biofilm and planktonic populations using metabolic labeling and mass spectrometry. *BMC Microbiol.* **14,** 329 (2014).

74. Favre, L. *et al.* Discrimination of Four Marine Biofilm-Forming Bacteria by LC-MS Metabolomics and Influence of Culture Parameters. *J. Proteome Res.* (2017). doi:10.1021/acs.jproteome.6b01027

75. Stîngu, C. S., Rodloff, A. C., Jentsch, H., Schaumann, R. & Eschrich, K. Rapid identification of oral anaerobic bacteria cultivated from subgingival biofilm by MALDI-TOF-MS. *Oral Microbiol. Immunol.* **23,** 372–376 (2008).

76. Lanni, E. J. *et al.* MALDI-guided SIMS: Multiscale Imaging of Metabolites in Bacterial Biofilms. *Anal. Chem.* **86,** 9139–9145 (2014).

77. Palmer, L. D. & Skaar, E. P. Transition Metals and Virulence in Bacteria. *Annu. Rev. Genet.* **50,** 67–91 (2016).

78. Cherayil, B. J. The role of iron in the immune response to bacterial infection. *Immunol. Res.* **50,** 1–9 (2011).

79. I. Holden, V. & A. Bachman, M. Diverging roles of bacterial siderophores during infection. *Metallomics* **7,** 986–995 (2015).

80. Kortman, G. A. M., Raffatellu, M., Swinkels, D. W. & Tjalsma, H. Nutritional iron turned inside out: intestinal stress from a gut microbial perspective. *FEMS Microbiol. Rev.* **38,** 1202–1234 (2014).

81. Barber, M. F. & Elde, N. C. Buried Treasure: Evolutionary Perspectives on Microbial Iron Piracy. *Trends Genet.* **31,** 627–636 (2015).

82. Valdebenito, M., Crumbliss, A. L., Winkelmann, G. & Hantke, K. Environmental factors influence the production of enterobactin, salmochelin, aerobactin, and yersiniabactin in Escherichia coli strain Nissle 1917. *Int. J. Med. Microbiol. IJMM* **296,** 513–520 (2006).

83. Behnsen, J. *et al.* The cytokine IL-22 promotes pathogen colonization by suppressing related commensal bacteria. *Immunity* **40,** 262–273 (2014).

84. Lee, W., van Baalen, M. & Jansen, V. A. A. An evolutionary mechanism for diversity in siderophore-producing bacteria. *Ecol. Lett.* **15,** 119–125 (2012).

85. Dumas, Z. & Kümmerli, R. Cost of cooperation rules selection for cheats in bacterial metapopulations. *J. Evol. Biol.* **25,** 473–484 (2012).

86. Leinweber, A., Fredrik Inglis, R. & Kümmerli, R. Cheating fosters species co-existence in well-mixed bacterial communities. *ISME J.* (2017). doi:10.1038/ismej.2016.195

87. Harrison, F. Dynamic social behaviour in a bacterium: pseudomonas aeruginosa partially compensates for siderophore loss to cheats. *J. Evol. Biol.* **26,** 1370–1378 (2013).

88. Vassiliadis, G., Destoumieux-Garzón, D., Lombard, C., Rebuffat, S. & Peduzzi, J. Isolation and Characterization of Two Members of the Siderophore-Microcin Family, Microcins M and H47. *Antimicrob. Agents Chemother.* **54,** 288–297 (2010).

89. Thomas, X. *et al.* Siderophore Peptide, a New Type of Post-translationally Modified Antibacterial Peptide with Potent Activity. *J. Biol. Chem.* **279,** 28233–28242 (2004).

90. Vassiliadis, G. *et al.* Insight into Siderophore-Carrying Peptide Biosynthesis: Enterobactin Is a Precursor for Microcin E492 Posttranslational Modification. *Antimicrob. Agents Chemother.* **51,** 3546–3553 (2007).

91. Duquesne, S., Destoumieux-Garzón, D., Peduzzi, J. & Rebuffat, S. Microcins, gene-encoded antibacterial peptides from enterobacteria. *Nat. Prod. Rep.* **24,** 708–734 (2007).

92. Duquesne, S., Petit, V., Peduzzi, J. & Rebuffat, S. Structural and functional diversity of microcins, gene-encoded antibacterial peptides from enterobacteria. *J. Mol. Microbiol. Biotechnol.* **13,** 200–209 (2007).

93. Zschüttig, A. *et al.* Identification and Characterization of Microcin S, a New Antibacterial Peptide Produced by Probiotic Escherichia coli G3/10. *PLOS ONE* **7,** e33351 (2012).

94. Rebuffat, S. Microcins in action: amazing defence strategies of Enterobacteria. *Biochem. Soc. Trans.* **40,** 1456–1462 (2012).

95. Patzer, S. I., Baquero, M. R., Bravo, D., Moreno, F. & Hantke, K. The colicin G, H and X determinants encode microcins M and H47, which might utilize the catecholate siderophore receptors FepA, Cir, Fiu and IroN. *Microbiol. Read. Engl.* **149,** 2557–2570 (2003).

96. Barman, M. *et al.* Enteric salmonellosis disrupts the microbial ecology of the murine gastrointestinal tract. *Infect. Immun.* **76,** 907–915 (2008).

97. Stecher, B. *et al.* Salmonella enterica serovar typhimurium exploits inflammation to compete with the intestinal microbiota. *PLoS Biol.* **5,** 2177–2189 (2007).

98. Lawley, T. D. *et al.* Host Transmission of Salmonella enterica Serovar Typhimurium Is Controlled by Virulence Factors and Indigenous Intestinal Microbiota. *Infect. Immun.* **76,** 403–416 (2008).

99. Sassone-Corsi, M. *et al.* Microcins mediate competition among Enterobacteriaceae in the inflamed gut. *Nature* **540,** 280–283 (2016).

100. Harrison, F. & Buckling, A. Siderophore production and biofilm formation as linked social traits. *ISME J.* **3,** 632–634 (2009).

101. Lin, M.-H., Shu, J.-C., Huang, H.-Y. & Cheng, Y.-C. Involvement of Iron in Biofilm Formation by Staphylococcus aureus. *PLOS ONE* **7,** e34388 (2012).

102. Cornelis, P. & Dingemans, J. Pseudomonas aeruginosa adapts its iron uptake strategies in function of the type of infections. *Front. Cell. Infect. Microbiol.* **3,** (2013).

103. Trejo-Hernández, A., Andrade-Domínguez, A., Hernández, M. & Encarnación, S. Interspecies competition triggers virulence and mutability in Candida albicans–Pseudomonas aeruginosa mixed biofilms. *ISME J.* **8,** 1974–1988 (2014).

104. Filkins, L. M. *et al.* Coculture of Staphylococcus aureus with Pseudomonas aeruginosa Drives S. aureus towards Fermentative Metabolism and Reduced Viability in a Cystic Fibrosis Model. *J. Bacteriol.* **197,** 2252–2264 (2015).

105. Nolan, E. M., Fischbach, M. A., Koglin, A. & Walsh, C. T. Biosynthetic Tailoring of Microcin E492m: Post-Translational Modification Affords an Antibacterial Siderophore-Peptide Conjugate. *J. Am. Chem. Soc.* **129,** 14336–14347 (2007).

106. Nolan, E. M. & Walsh, C. T. Investigations of the MceIJ-catalyzed posttranslational modification of the microcin E492 C-terminus: linkage of ribosomal and nonribosomal peptides to form ‘trojan horse’ antibiotics. *Biochemistry (Mosc.)* **47,** 9289–9299 (2008).

107. Martinez-Medina, M. & Garcia-Gil, L. J. Escherichia coli in chronic inflammatory bowel diseases: An update on adherent invasive Escherichia coli pathogenicity. *World J. Gastrointest. Pathophysiol.* **5,** 213–227 (2014).

108. García-Bustos, J. F., Pezzi, N. & Asensio, C. Microcin 7: purification and properties. *Biochem. Biophys. Res. Commun.* **119,** 779–785 (1984).

109. de Lorenzo, V. Isolation and characterization of microcin E492 from Klebsiella pneumoniae. *Arch. Microbiol.* **139,** 72–75 (1984).

110. Pons, A.-M. *et al.* Microcin E492 Is an Unmodified Peptide Related in Structure to Colicin V. *Antimicrob. Agents Chemother.* **46,** 229–230 (2002).

111. Corsini, G. *et al.* Purification and characterization of the antimicrobial peptide microcin N. *FEMS Microbiol. Lett.* **312,** 119–125 (2010).

112. Mercado, G., Tello, M., Marín, M., Monasterio, O. & Lagos, R. The Production In Vivo of Microcin E492 with Antibacterial Activity Depends on Salmochelin and EntF. *J. Bacteriol.* **190,** 5464–5471 (2008).

113. Kostakioti, M., Hadjifrangiskou, M. & Hultgren, S. J. Bacterial Biofilms: Development, Dispersal, and Therapeutic Strategies in the Dawn of the Postantibiotic Era. *Cold Spring Harb. Perspect. Med.* **3,** (2013).

114. Stewart, P. S. & Franklin, M. J. Physiological heterogeneity in biofilms. *Nat. Rev. Microbiol.* **6,** 199–210 (2008).

115. Sauer, K. *et al.* Characterization of Nutrient-Induced Dispersion in Pseudomonas aeruginosa PAO1 Biofilm. *J. Bacteriol.* **186,** 7312–7326 (2004).

116. Karatan, E. & Watnick, P. Signals, Regulatory Networks, and Materials That Build and Break Bacterial Biofilms. *Microbiol. Mol. Biol. Rev. MMBR* **73,** 310–347 (2009).

117. Boles, B. R. & Horswill, A. R. agr-Mediated Dispersal of Staphylococcus aureus Biofilms. *PLoS Pathog.* **4,** (2008).

118. Davies, D. G. & Marques, C. N. H. A Fatty Acid Messenger Is Responsible for Inducing Dispersion in Microbial Biofilms. *J. Bacteriol.* **191,** 1393–1403 (2009).

119. Marques, C. N. H., Morozov, A., Planzos, P. & Zelaya, H. M. The Fatty Acid Signaling Molecule cis-2-Decenoic Acid Increases Metabolic Activity and Reverts Persister Cells to an Antimicrobial-Susceptible State. *Appl. Environ. Microbiol.* **80,** 6976–6991 (2014).

120. Solano, C., Echeverz, M. & Lasa, I. Biofilm dispersion and quorum sensing. *Curr. Opin. Microbiol.* **18,** 96–104 (2014).

121. Irie, Y., O'Toole, G. A. & Yuk, M. H. Pseudomonas aeruginosa rhamnolipids disperse Bordetella bronchiseptica biofilms. *FEMS Microbiol. Lett.* **250,** 237–243 (2005).

122. Mireles, J. R., Toguchi, A. & Harshey, R. M. Salmonella enterica serovar typhimurium swarming mutants with altered biofilm-forming abilities: surfactin inhibits biofilm formation. *J. Bacteriol.* **183,** 5848–5854 (2001).

123. Dean, S. N., Chung, M.-C. & Hoek, M. L. van. Burkholderia Diffusible Signal Factor Signals to Francisella novicida To Disperse Biofilm and Increase Siderophore Production. *Appl. Environ. Microbiol.* **81,** 7057–7066 (2015).

124. Boyd, A. & Chakrabarty, A. M. Role of alginate lyase in cell detachment of Pseudomonas aeruginosa. *Appl. Environ. Microbiol.* **60,** 2355–2359 (1994).

125. Kaplan, J. B., Ragunath, C., Ramasubbu, N. & Fine, D. H. Detachment of Actinobacillus actinomycetemcomitans Biofilm Cells by an Endogenous β-Hexosaminidase Activity. *J. Bacteriol.* **185,** 4693–4698 (2003).

126. Purevdorj-Gage, B., Costerton, W. J. & Stoodley, P. Phenotypic differentiation and seeding dispersal in non-mucoid and mucoid Pseudomonas aeruginosa biofilms. *Microbiol. Read. Engl.* **151,** 1569–1576 (2005).

127. Dong, Y.-H., Zhang, X.-F., An, S.-W., Xu, J.-L. & Zhang, L.-H. A novel two-component system BqsS-BqsR modulates quorum sensing-dependent biofilm decay in Pseudomonas aeruginosa. *Commun. Integr. Biol.* **1,** 88–96 (2008).

128. Barraud, N. *et al.* Involvement of Nitric Oxide in Biofilm Dispersal of Pseudomonas aeruginosa. *J. Bacteriol.* **188,** 7344–7353 (2006).

129. Ma, Q., Zhang, G. & Wood, T. K. Escherichia coli BdcA controls biofilm dispersal in Pseudomonas aeruginosa and Rhizobium meliloti. *BMC Res. Notes* **4,** 447 (2011).

130. Medina, G., Juárez, K., Valderrama, B. & Soberón-Chávez, G. Mechanism of Pseudomonas aeruginosa RhlR Transcriptional Regulation of the rhlAB Promoter. *J. Bacteriol.* **185,** 5976–5983 (2003).

131. Lequette, Y. & Greenberg, E. P. Timing and Localization of Rhamnolipid Synthesis Gene Expression in Pseudomonas aeruginosa Biofilms. *J. Bacteriol.* **187,** 37–44 (2005).

132. Reis, R. S., Pereira, A. G., Neves, B. C. & Freire, D. M. G. Gene regulation of rhamnolipid production in Pseudomonas aeruginosa – A review. *Bioresour. Technol.* **102,** 6377–6384 (2011).

133. Haba, E., Abalos, A., Jáuregui, O., Espuny, M. J. & Manresa, A. Use of liquid chromatography-mass spectroscopy for studying the composition and properties of rhamnolipids produced by different strains of Pseudomonas aeruginosa. *J. Surfactants Deterg.* **6,** 155–161 (2003).

134. Caiazza, N. C., Shanks, R. M. Q. & O'Toole, G. A. Rhamnolipids Modulate Swarming Motility Patterns of Pseudomonas aeruginosa. *J. Bacteriol.* **187,** 7351–7361 (2005).

135. Davey, M. E., Caiazza, N. C. & O'Toole, G. A. Rhamnolipid Surfactant Production Affects Biofilm Architecture in Pseudomonas aeruginosa PAO1. *J. Bacteriol.* **185,** 1027–1036 (2003).

136. Boles, B. R., Thoendel, M. & Singh, P. K. Rhamnolipids mediate detachment of Pseudomonas aeruginosa from biofilms. *Mol. Microbiol.* **57,** 1210–1223 (2005).

137. Abdel-Mawgoud, A. M., Lépine, F. & Déziel, E. Rhamnolipids: diversity of structures, microbial origins and roles. *Appl. Microbiol. Biotechnol.* **86,** 1323–1336 (2010).

138. Kuchma, S. L. *et al.* Cyclic-di-GMP-Mediated Repression of Swarming Motility by Pseudomonas aeruginosa: the pilY1 Gene and Its Impact on Surface-Associated Behaviors. *J. Bacteriol.* **192,** 2950–2964 (2010).

139. Lee, C. H. & Tsai, C. M. Quantification of bacterial lipopolysaccharides by the purpald assay: measuring formaldehyde generated from 2-keto-3-deoxyoctonate and heptose at the inner core by periodate oxidation. *Anal. Biochem.* **267,** 161–168 (1999).

140. Al-Tahhan, R. A., Sandrin, T. R., Bodour, A. A. & Maier, R. M. Rhamnolipid-Induced Removal of Lipopolysaccharide from Pseudomonas aeruginosa: Effect on Cell Surface Properties and Interaction with Hydrophobic Substrates. *Appl. Environ. Microbiol.* **66,** 3262–3268 (2000).

141. Kim, S.-K. & Lee, J.-H. Biofilm dispersion in Pseudomonas aeruginosa. *J. Microbiol. Seoul Korea* **54,** 71–85 (2016).

142. Lee, J., Jayaraman, A. & Wood, T. K. Indole is an inter-species biofilm signal mediated by SdiA. *BMC Microbiol.* **7,** 42 (2007).

143. Pearson, J. P., Pesci, E. C. & Iglewski, B. H. Roles of Pseudomonas aeruginosa las and rhl quorum-sensing systems in control of elastase and rhamnolipid biosynthesis genes. *J. Bacteriol.* **179,** 5756–5767 (1997).

144. Gao, X. *et al.* Functional Characterization of Core Components of the Bacillus subtilis Cyclic-Di-GMP Signaling Pathway. *J. Bacteriol.* **195,** 4782–4792 (2013).

145. Koestler, B. J. & Waters, C. M. Exploring Environmental Control of Cyclic di-GMP Signaling in Vibrio cholerae by Using the Ex Vivo Lysate Cyclic di-GMP Assay (TELCA). *Appl. Environ. Microbiol.* **79,** 5233–5241 (2013).

146. Römling, U., Galperin, M. Y. & Gomelsky, M. Cyclic di-GMP: the first 25 years of a universal bacterial second messenger. *Microbiol. Mol. Biol. Rev. MMBR* **77,** 1–52 (2013).

147. Simm, R., Morr, M., Kader, A., Nimtz, M. & Römling, U. GGDEF and EAL domains inversely regulate cyclic di-GMP levels and transition from sessility to motility. *Mol. Microbiol.* **53,** 1123–1134 (2004).

148. Hengge, R. *et al.* Systematic nomenclature for GGDEF and EAL domain-containing c-di-GMP turnover proteins of Escherichia coli. *J. Bacteriol.* JB.00424-15 (2015). doi:10.1128/JB.00424-15

149. Høiby, N., Bjarnsholt, T., Givskov, M., Molin, S. & Ciofu, O. Antibiotic resistance of bacterial biofilms. *Int. J. Antimicrob. Agents* **35,** 322–332 (2010).

150. Lebeaux, D., Ghigo, J.-M. & Beloin, C. Biofilm-Related Infections: Bridging the Gap between Clinical Management and Fundamental Aspects of Recalcitrance toward Antibiotics. *Microbiol. Mol. Biol. Rev.* **78,** 510–543 (2014).

151. Zhao, G. *et al.* Biofilms and Inflammation in Chronic Wounds. *Adv. Wound Care* **2,** 389–399 (2013).

152. Peleg, A. Y. & Hooper, D. C. Hospital-Acquired Infections Due to Gram-Negative Bacteria. *N. Engl. J. Med.* **362,** 1804–1813 (2010).

153. Macfarlane, S. & Dillon, J. f. Microbial biofilms in the human gastrointestinal tract. *J. Appl. Microbiol.* **102,** 1187–1196 (2007).

154. Brune, K. D. & Bayer, T. S. Engineering microbial consortia to enhance biomining and bioremediation. *Front. Microbiol.* **3,** (2012).

155. Nevin, K. P. *et al.* Electrosynthesis of Organic Compounds from Carbon Dioxide Is Catalyzed by a Diversity of Acetogenic Microorganisms▽. *Appl. Environ. Microbiol.* **77,** 2882–2886 (2011).

156. Cusick, R. D., Kim, Y. & Logan, B. E. Energy Capture from Thermolytic Solutions in Microbial Reverse-Electrodialysis Cells. *Science* **335,** 1474–1477 (2012).

157. Mitri, S., Xavier, J. B. & Foster, K. R. Social evolution in multispecies biofilms. *Proc. Natl. Acad. Sci.* **108,** 10839–10846 (2011).

158. Murray, J. L., Connell, J. L., Stacy, A., Turner, K. H. & Whiteley, M. Mechanisms of synergy in polymicrobial infections. *J. Microbiol. Seoul Korea* **52,** 188–199 (2014).

159. De Roy, K., Marzorati, M., Van den Abbeele, P., Van de Wiele, T. & Boon, N. Synthetic microbial ecosystems: an exciting tool to understand and apply microbial communities. *Environ. Microbiol.* **16,** 1472–1481 (2014).

160. Agapakis, C. M., Boyle, P. M. & Silver, P. A. Natural strategies for the spatial optimization of metabolism in synthetic biology. *Nat. Chem. Biol.* **8,** 527–535 (2012).

161. Camp, J. G., Kanther, M., Semova, I. & Rawls, J. F. Patterns and scales in gastrointestinal microbial ecology. *Gastroenterology* **136,** 1989–2002 (2009).

162. Werner, G. D. A. *et al.* Evolution of microbial markets. *Proc. Natl. Acad. Sci.* **111,** 1237–1244 (2014).

163. Balaban, N. Q., Merrin, J., Chait, R., Kowalik, L. & Leibler, S. Bacterial persistence as a phenotypic switch. *Science* **305,** 1622–1625 (2004).

164. Boedicker, J. Q., Li, L., Kline, T. R. & Ismagilov, R. F. Detecting bacteria and determining their susceptibility to antibiotics by stochastic confinement in nanoliter droplets using plug-based microfluidics. *Lab. Chip* **8,** 1265–1272 (2008).

165. Boedicker, J. Q., Vincent, M. E. & Ismagilov, R. F. Microfluidic Confinement of Single Cells of Bacteria in Small Volumes Initiates High-Density Behavior of Quorum Sensing and Growth and Reveals Its Variability. *Angew. Chem. Int. Ed.* **48,** 5908–5911 (2009).

166. Carnes, E. C. *et al.* Confinement-induced quorum sensing of individual Staphylococcus aureus bacteria. *Nat. Chem. Biol.* **6,** 41–45 (2010).

167. Park, S., Hong, X., Choi, W. S. & Kim, T. Microfabricated ratchet structure integrated concentrator arrays for synthetic bacterial cell-to-cell communication assays. *Lab. Chip* **12,** 3914–3922 (2012).

168. Gonzalez, L. E. & Bashan, Y. Increased Growth of the Microalga Chlorella vulgaris when Coimmobilized and Cocultured in Alginate Beads with the Plant-Growth-Promoting Bacterium Azospirillum brasilense. *Appl. Environ. Microbiol.* **66,** 1527–1531 (2000).

169. Kim, H. J., Boedicker, J. Q., Choi, J. W. & Ismagilov, R. F. Defined spatial structure stabilizes a synthetic multispecies bacterial community. *Proc. Natl. Acad. Sci.* **105,** 18188–18193 (2008).

170. Connell, J. L., Ritschdorff, E. T., Whiteley, M. & Shear, J. B. 3D printing of microscopic bacterial communities. *Proc. Natl. Acad. Sci.* **110,** 18380–18385 (2013).

171. Brenner, K. & Arnold, F. H. Self-Organization, Layered Structure, and Aggregation Enhance Persistence of a Synthetic Biofilm Consortium. *PLOS ONE* **6,** e16791 (2011).

172. Kim, H. J., Du, W. & Ismagilov, R. F. Complex function by design using spatially pre-structured synthetic microbial communities: degradation of pentachlorophenol in the presence of Hg(ii). *Integr. Biol. Quant. Biosci. Nano Macro* **3,** 126–133 (2011).

173. Bhattacharjee, A., Nusca, T. D. & Hochbaum, A. I. Rhamnolipids Mediate an Interspecies Biofilm Dispersal Signaling Pathway. *ACS Chem. Biol.* **11,** 3068–3076 (2016).

174. Datsenko, K. A. & Wanner, B. L. One-step inactivation of chromosomal genes in Escherichia coli K-12 using PCR products. *Proc. Natl. Acad. Sci. U. S. A.* **97,** 6640–6645 (2000).

175. Kim, P., Adorno-Martinez, W. E., Khan, M. & Aizenberg, J. Enriching libraries of high-aspect-ratio micro- or nanostructures by rapid, low-cost, benchtop nanofabrication. *Nat. Protoc.* **7,** 311–327 (2012).

176. Maluf, N. & Williams, K. *Introduction to Microelectromechanical Systems Engineering*. (Artech House, 2004).

177. Pokroy, B., Epstein, A. K., Persson-Gulda, M. C. M. & Aizenberg, J. Fabrication of Bioinspired Actuated Nanostructures with Arbitrary Geometry and Stiffness. *Adv. Mater.* **21,** 463–469 (2009).

178. Davey, H. M. & Hexley, P. Red but not dead? Membranes of stressed Saccharomyces cerevisiae are permeable to propidium iodide. *Environ. Microbiol.* **13,** 163–171 (2011).

179. Joshi, G. C., Bhatnagar, R., Doraiswamy, S. & Periasamy, N. Diffusion-controlled reactions: transient effects in the fluorescence quenching of indole and N-acetyltryptophanamide in water. *J. Phys. Chem.* **94,** 2908–2914 (1990).

180. Beyenal, H., Şleker, Ş., Tanyolaç, A. & Salih, B. Diffusion coefficients of phenol and oxygen in a biofilm of pseudomonas putida. *AIChE J.* **43,** 243–250 (1997).

181. Bansal, T., Alaniz, R. C., Wood, T. K. & Jayaraman, A. The bacterial signal indole increases epithelial-cell tight-junction resistance and attenuates indicators of inflammation. *Proc. Natl. Acad. Sci. U. S. A.* **107,** 228–233 (2010).

182. Piñero-Fernandez, S., Chimerel, C., Keyser, U. F. & Summers, D. K. Indole Transport across Escherichia coli Membranes. *J. Bacteriol.* **193,** 1793–1798 (2011).

183. Lee, J., Maeda, T., Hong, S. H. & Wood, T. K. Reconfiguring the Quorum-Sensing Regulator SdiA of Escherichia coli To Control Biofilm Formation via Indole and N-Acylhomoserine Lactones. *Appl. Environ. Microbiol.* **75,** 1703–1716 (2009).

184. Vlachopoulou, M.-E. *et al.* A low temperature surface modification assisted method for bonding plastic substrates. *J. Micromech. Microeng.* **19,** 15007 (2009).

185. Chinga, G., Johnsen, P. O., Dougherty, R., Berli, E. L. & Walter, J. Quantification of the 3D microstructure of SC surfaces. *J. Microsc.* **227,** 254–265 (2007).

186. Sasaki-Imamura, T., Yano, A. & Yoshida, Y. Production of Indole from l-Tryptophan and Effects of These Compounds on Biofilm Formation by Fusobacterium nucleatum ATCC 25586. *Appl. Environ. Microbiol.* **76,** 4260–4268 (2010).

187. Li, G. & Young, K. D. Indole production by the tryptophanase TnaA in Escherichia coli is determined by the amount of exogenous tryptophan. *Microbiol. Read. Engl.* **159,** 402–410 (2013).

188. Lee, J.-H. & Lee, J. Indole as an intercellular signal in microbial communities. *FEMS Microbiol. Rev.* **34,** 426–444 (2010).

189. Chu, W. *et al.* Indole Production Promotes Escherichia coli Mixed-Culture Growth with Pseudomonas aeruginosa by Inhibiting Quorum Signaling. *Appl. Environ. Microbiol.* **78,** 411–419 (2012).

190. Lee, J., Attila, C., Cirillo, S. L. G., Cirillo, J. D. & Wood, T. K. Indole and 7-hydroxyindole diminish Pseudomonas aeruginosa virulence. *Microb. Biotechnol.* **2,** 75–90 (2009).

191. Hirsch, E. B. & Tam, V. H. Impact of multidrug-resistant Pseudomonas aeruginosa infection on patient outcomes. *Expert Rev. Pharmacoecon. Outcomes Res.* **10,** 441–451 (2010).

192. Yayan, J., Ghebremedhin, B. & Rasche, K. Antibiotic Resistance of Pseudomonas aeruginosa in Pneumonia at a Single University Hospital Center in Germany over a 10-Year Period. *PLOS ONE* **10,** e0139836 (2015).

193. Aloush, V., Navon-Venezia, S., Seigman-Igra, Y., Cabili, S. & Carmeli, Y. Multidrug-Resistant Pseudomonas aeruginosa: Risk Factors and Clinical Impact. *Antimicrob. Agents Chemother.* **50,** 43–48 (2006).

194. Andrews, J. M. Determination of minimum inhibitory concentrations. *J. Antimicrob. Chemother.* **48,** 5–16 (2001).

195. Lee, J. *et al.* Indole cell signaling occurs primarily at low temperatures in Escherichia coli. *ISME J.* **2,** 1007–1023 (2008).

196. Mueller, R. S., Beyhan, S., Saini, S. G., Yildiz, F. H. & Bartlett, D. H. Indole Acts as an Extracellular Cue Regulating Gene Expression in Vibrio cholerae. *J. Bacteriol.* **191,** 3504–3516 (2009).

197. Lee, J., Jayaraman, A. & Wood, T. K. Indole is an inter-species biofilm signal mediated by SdiA. *BMC Microbiol.* **7,** 42 (2007).

198. Culotti, A. & Packman, A. I. Pseudomonas aeruginosa Promotes Escherichia coli Biofilm Formation in Nutrient-Limited Medium. *PloS One* **9,** e107186

199. Hidalgo-Romano, B. *et al.* Indole inhibition of N-acylated homoserine lactone-mediated quorum signalling is widespread in Gram-negative bacteria. *Microbiol. Read. Engl.* **160,** 2464–2473 (2014).

200. Raad, I. *et al.* Ultrastructural Analysis of Indwelling Vascular Catheters: A Quantitative Relationship between Luminal Colonization and Duration of Placement. *J. Infect. Dis.* **168,** 400–407 (1993).

201. Anderson, E. S. Viability of, and transfer of a plasmid from, E. coli K12 in the human intestine. *Nature* **255,** 502–504 (1975).

202. Smith, H. W. Survival of orally administered E. coli K12 in alimentary tract of man. *Nature* **255,** 500–502 (1975).

203. Ito, A., Taniuchi, A., May, T., Kawata, K. & Okabe, S. Increased Antibiotic Resistance of Escherichia coli in Mature Biofilms. *Appl. Environ. Microbiol.* **75,** 4093–4100 (2009).

204. Vega, N. M. & Gore, J. Collective antibiotic resistance: mechanisms and implications. *Curr. Opin. Microbiol.* **21,** 28–34 (2014).

205. Stewart, P. S. Mechanisms of antibiotic resistance in bacterial biofilms. *Int. J. Med. Microbiol. IJMM* **292,** 107–113 (2002).

206. Stasulli, N. M., Shank, E. A. & Gibbs, K. Profiling the metabolic signals involved in chemical communication between microbes using imaging mass spectrometry. *FEMS Microbiol. Rev.* **40,** 807–813 (2016).

207. Kaltenpoth, M., Strupat, K. & Svatoš, A. Linking metabolite production to taxonomic identity in environmental samples by (MA)LDI-FISH. *ISME J.* **10,** 527–531 (2016).

208. Louie, K. B. *et al.* 'Replica-Extraction-Transfer' Nanostructure-Initiator Mass Spectrometry Imaging of Acoustically Printed Bacteria. *Anal. Chem.* **85,** 10856–10862 (2013).

209. Nikaido, H. Multidrug Resistance in Bacteria. *Annu. Rev. Biochem.* **78,** 119–146 (2009).

210. Worthington, R. J. & Melander, C. Combination approaches to combat multidrug-resistant bacteria. *Trends Biotechnol.* **31,** 177–184 (2013).

211. Smith, P. A. & Romesberg, F. E. Combating bacteria and drug resistance by inhibiting mechanisms of persistence and adaptation. *Nat. Chem. Biol.* **3,** 549–556 (2007).

212. Shah, D. *et al.* Persisters: a distinct physiological state of E. coli. *BMC Microbiol.* **6,** 53 (2006).

213. Dhar, N. & McKinney, J. D. Microbial phenotypic heterogeneity and antibiotic tolerance. *Curr. Opin. Microbiol.* **10,** 30–38 (2007).

214. Berezin, M. Y. & Achilefu, S. Fluorescence Lifetime Measurements and Biological Imaging. *Chem. Rev.* **110,** 2641–2684 (2010).

215. Bird, D. K. *et al.* Metabolic mapping of MCF10A human breast cells via multiphoton fluorescence lifetime imaging of the coenzyme NADH. *Cancer Res.* **65,** 8766–8773 (2005).

216. Skala, M. C. *et al.* In vivo multiphoton fluorescence lifetime imaging of protein-bound and free nicotinamide adenine dinucleotide in normal and precancerous epithelia. *J. Biomed. Opt.* **12,** 24014 (2007).

217. Walsh, A. J. *et al.* Optical metabolic imaging identifies glycolytic levels, subtypes, and early-treatment response in breast cancer. *Cancer Res.* **73,** 6164–6174 (2013).

218. Quinn, K. P. *et al.* Quantitative metabolic imaging using endogenous fluorescence to detect stem cell differentiation. *Sci. Rep.* **3,** 3432 (2013).

219. Stringari, C., Sierra, R., Donovan, P. J. & Gratton, E. Label-free separation of human embryonic stem cells and their differentiating progenies by phasor fluorescence lifetime microscopy. *J. Biomed. Opt.* **17,** 46012 (2012).

220. Datta, R., Heylman, C., George, S. C. & Gratton, E. Label-free imaging of metabolism and oxidative stress in human induced pluripotent stem cell-derived cardiomyocytes. *Biomed. Opt. Express* **7,** 1690–1701 (2016).

221. Sobrino, A. *et al.* 3D microtumors in vitro supported by perfused vascular networks. *Sci. Rep.* **6,** 31589 (2016).

222. Lakowicz, J. R., Szmacinski, H., Nowaczyk, K. & Johnson, M. L. Fluorescence lifetime imaging of free and protein-bound NADH. *Proc. Natl. Acad. Sci.* **89,** 1271–1275 (1992).

223. Ammor, M. S. Recent Advances in the Use of Intrinsic Fluorescence for Bacterial Identification and Characterization. *J. Fluoresc.* **17,** 455–459 (2007).

224. Estes, C. *et al.* Reagentless detection of microorganisms by intrinsic fluorescence. *Biosens. Bioelectron.* **18,** 511–519 (2003).

225. Sullivan, N. L., Tzeranis, D. S., Wang, Y., So, P. T. C. & Newman, D. Quantifying the Dynamics of Bacterial Secondary Metabolites by Spectral Multiphoton Microscopy. *ACS Chem. Biol.* **6,** 893–899 (2011).

226. Alimova, A. *et al.* Native fluorescence and excitation spectroscopic changes in Bacillus subtilis and Staphylococcus aureus bacteria subjected to conditions of starvation. *Appl. Opt.* **42,** 4080–4087 (2003).

227. Dartnell, L. R., Roberts, T. A., Moore, G., Ward, J. M. & Muller, J.-P. Fluorescence Characterization of Clinically-Important Bacteria. *PLOS ONE* **8,** e75270 (2013).

228. Ammor, S., Yaakoubi, K., Chevallier, I. & Dufour, E. Identification by fluorescence spectroscopy of lactic acid bacteria isolated from a small-scale facility producing traditional dry sausages. *J. Microbiol. Methods* **59,** 271–281 (2004).

229. Leblanc, L. & Dufour, É. Monitoring the identity of bacteria using their intrinsic fluorescence. *FEMS Microbiol. Lett.* **211,** 147–153 (2002).

230. Giana, H. E., Silveira, L., Zângaro, R. A. & Pacheco, M. T. T. Rapid Identification of Bacterial Species by Fluorescence Spectroscopy and Classification Through Principal Components Analysis. *J. Fluoresc.* **13,** 489–493 (2003).

231. Bailey, K. F. R. J. . Metabolic Pathway Rates and Culture Fluorescence in Batch Fermentations of Clostridium Acetobutylicum. **3,** 153–167 (1987).

232. Harrison, D. E. & Loveless, J. E. The effect of growth conditions on respiratory activity and growth efficiency in facultative anaerobes grown in chemostat culture. *J. Gen. Microbiol.* **68,** 35–43 (1971).

233. ARMIGER, W. B., FORRO, J. F., MONTALVO, L. M., LEE, J. F. & ZABRISKIE, D. W. The Interpretation of on-Line Process Measurements of Intracellular Nadh in Fermentation Processes. *Chem. Eng. Commun.* **45,** 197–206 (1986).

234. Rao, G. & Mutharasan, R. NADH levels and solventogenesis in Clostridium acetobutylicum: New insights through culture fluorescence. *Appl. Microbiol. Biotechnol.* **30,** 59–66 (1989).

235. Wos, M. & Pollard, P. Sensitive and meaningful measures of bacterial metabolic activity using NADH fluorescence. *Water Res.* **40,** 2084–2092 (2006).

236. Harrison, D. E. Undamped oscillations of pyridine nucleotide and oxygen tension in chemostat cultures of Klebsiella aerogenes. *J. Cell Biol.* **45,** 514–521 (1970).

237. Wimpenny, J. W. T. & Firth, A. Levels of Nicotinamide Adenine Dinucleotide and Reduced Nicotinamide Adenine Dinucleotide in Facultative Bacteria and the Effect of Oxygen. *J. Bacteriol.* **111,** 24–32 (1972).

238. Dalterio, R. A. *et al.* The Steady-State and Decay Characteristics of Primary Fluorescence from Live Bacteria. *Appl. Spectrosc.* **41,** 234–241 (1987).

239. Wos, M. L. & Pollard, P. C. Cellular nicotinamide adenine dinucleotide (NADH) as an indicator of bacterial metabolic activity dynamics in activated sludge. *Water Sci. Technol. J. Int. Assoc. Water Pollut. Res.* **60,** 783–791 (2009).

240. Brahma, S. K. *et al.* The Rapid Identification of Bacteria Using Time-Resolved Fluorescence and Fluorescence Excitation Spectral Methods. *Appl. Spectrosc.* **39,** 869–872 (1985).

241. Awad, F. *et al.* Optical Fiber-Based Steady State and Fluorescence Lifetime Spectroscopy for Rapid Identification and Classification of Bacterial Pathogens Directly from Colonies on Agar Plates, Optical Fiber-Based Steady State and Fluorescence Lifetime Spectroscopy for Rapid Identification and Classification of Bacterial Pathogens Directly from Colonies on Agar Plates. *Int. Sch. Res. Not. Int. Sch. Res. Not.* **2014, 2014,** e430412 (2014).

242. Szaszák, M. *et al.* Fluorescence Lifetime Imaging Unravels C. trachomatis Metabolism and Its Crosstalk with the Host Cell. *PLOS Pathog* **7,** e1002108 (2011).

243. Digman, M. & Gratton, E. The phasor approach to fluorescence lifetime imaging: Exploiting phasor linear properties. in *Fluorescence Lifetime Spectroscopy and Imaging* 235–248 (CRC Press, 2014).

244. Stringari, C. *et al.* Phasor approach to fluorescence lifetime microscopy distinguishes different metabolic states of germ cells in a live tissue. *Proc. Natl. Acad. Sci. U. S. A.* **108,** 13582–13587 (2011).

245. Datta, R., Alfonso-García, A., Cinco, R. & Gratton, E. Fluorescence lifetime imaging of endogenous biomarker of oxidative stress. *Sci. Rep.* **5,** 9848 (2015).

246. Aguilar-Arnal, L. *et al.* Spatial dynamics of SIRT1 and the subnuclear distribution of NADH species. *Proc. Natl. Acad. Sci.* **113,** 12715–12720 (2016).

247. Stringari, C., Pate, K. T., Edwards, R. A., Waterman, M. L. & Gratton, E. Metabolic Imaging of Colon Cancer Tumors In Vivo by Phasor Fluorescence Lifetime Microscopy of NADH. *Biophys. J.* **104,** 342a–343a (2013).

248. Alfonso-García, A. *et al.* Label-free identification of macrophage phenotype by fluorescence lifetime imaging microscopy. *J. Biomed. Opt.* **21,** 46005 (2016).

249. Torno, K. *et al.* Real-time Analysis of Metabolic Activity Within Lactobacillus acidophilus by Phasor Fluorescence Lifetime Imaging Microscopy of NADH. *Curr. Microbiol.* **66,** 365–367 (2012).

250. Lobritz, M. A. *et al.* Antibiotic efficacy is linked to bacterial cellular respiration. *Proc. Natl. Acad. Sci.* **112,** 8173–8180 (2015).

251. Poole, K. Bacterial stress responses as determinants of antimicrobial resistance. *J. Antimicrob. Chemother.* dks196 (2012). doi:10.1093/jac/dks196

252. Zotta, T. *et al.* Assessment of Aerobic and Respiratory Growth in the Lactobacillus casei Group. *PLoS ONE* **9,** (2014).

253. González-Pinzón, R., Haggerty, R. & Myrold, D. D. Measuring aerobic respiration in stream ecosystems using the resazurin-resorufin system. *J. Geophys. Res. Biogeosciences* **117,** G00N06 (2012).

254. Spaans, S. K., Weusthuis, R. A., van der Oost, J. & Kengen, S. W. M. NADPH-generating systems in bacteria and archaea. *Front. Microbiol.* **6,** (2015).

255. Abrahams, G. L. & Abratt, V. R. The NADH-dependent glutamate dehydrogenase enzyme of Bacteroides fragilis Bf1 is induced by peptides in the growth medium. *Microbiol. Read. Engl.* **144 (Pt 6),** 1659–1667 (1998).

256. Heikal, A. *et al.* Structure of the bacterial type II NADH dehydrogenase: a monotopic membrane protein with an essential role in energy generation. *Mol. Microbiol.* **91,** 950–964 (2014).

257. LONDON, J. & KNIGHT, M. Concentrations of Nicotinamide Nucleotide Coenzymes in Micro-Organisms. *Microbiology* **44,** 241–254 (1966).

258. Graef, M. R. de, Alexeeva, S., Snoep, J. L. & Mattos, M. J. T. de. The Steady-State Internal Redox State (NADH/NAD) Reflects the External Redox State and Is Correlated with Catabolic Adaptation in Escherichia coli. *J. Bacteriol.* **181,** 2351–2357 (1999).

259. Dwyer, D. J. *et al.* Antibiotics induce redox-related physiological alterations as part of their lethality. *Proc. Natl. Acad. Sci.* **111,** E2100–E2109 (2014).

260. Blair, J. M. A., Webber, M. A., Baylay, A. J., Ogbolu, D. O. & Piddock, L. J. V. Molecular mechanisms of antibiotic resistance. *Nat. Rev. Microbiol.* **13,** 42–51 (2015).

261. Torres-Barceló, C., Kojadinovic, M., Moxon, R. & MacLean, R. C. The SOS response increases bacterial fitness, but not evolvability, under a sublethal dose of antibiotic. *Proc R Soc B* **282,** 20150885 (2015).

262. Meouche, I. E., Siu, Y. & Dunlop, M. J. Stochastic expression of a multiple antibiotic resistance activator confers transient resistance in single cells. *Sci. Rep.* **6,** 19538 (2016).

263. Fridman, O., Goldberg, A., Ronin, I., Shoresh, N. & Balaban, N. Q. Optimization of lag time underlies antibiotic tolerance in evolved bacterial populations. *Nature* **513,** 418–421 (2014).

264. Cabiscol, E., Tamarit, J. & Ros, J. Oxidative stress in bacteria and protein damage by reactive oxygen species. *Int. Microbiol. Off. J. Span. Soc. Microbiol.* **3,** 3–8 (2000).

265. Belenky, P. *et al.* Bactericidal Antibiotics Induce Toxic Metabolic Perturbations that Lead to Cellular Damage. *Cell Rep.* **13,** 968–980 (2015).

266. Rolfe, M. D. *et al.* Lag Phase Is a Distinct Growth Phase That Prepares Bacteria for Exponential Growth and Involves Transient Metal Accumulation. *J. Bacteriol.* **194,** 686–701 (2012).

267. Martin, D. S. THE OXYGEN CONSUMPTION OF ESCHERICHIA COLI DURING THE LAG AND LOGARITHMIC PHASES OF GROWTH. *J. Gen. Physiol.* **15,** 691–708 (1932).

268. Greig, M. E. & Hoogerheide, J. C. The Correlation of Bacterial Growth with Oxygen Consumption. *J. Bacteriol.* **41,** 549–556 (1941).

269. Llorens, N., María, J., Tormo, A. & Martínez-García, E. Stationary phase in gram-negative bacteria. *FEMS Microbiol. Rev.* **34,** 476–495 (2010).

270. Kolter, R. The Stationary Phase of The Bacterial Life Cycle. *Annu. Rev. Microbiol.* **47,** 855–874 (1993).

271. Finkel, S. E. Long-term survival during stationary phase: evolution and the GASP phenotype. *Nat. Rev. Microbiol.* **4,** 113–120 (2006).

272. Zambrano, M. M. & Kolter, R. GASPing for Life in Stationary Phase. *Cell* **86,** 181–184 (1996).

273. Bacun-Druzina, V., Cagalj, Z. & Gjuracic, K. The growth advantage in stationary-phase (GASP) phenomenon in mixed cultures of enterobacteria. *FEMS Microbiol. Lett.* **266,** 119–127 (2007).

274. Pletnev, P., Osterman, I., Sergiev, P., Bogdanov, A. & Dontsova, O. Survival guide: Escherichia coli in the stationary phase. *Acta Naturae* **7,** 22–33 (2015).

275. Farrell, M. J. & Finkel, S. E. The Growth Advantage in Stationary-Phase Phenotype Conferred by rpoS Mutations Is Dependent on the pH and Nutrient Environment. *J. Bacteriol.* **185,** 7044–7052 (2003).

276. Wu, H., Moser, C., Wang, H.-Z., Høiby, N. & Song, Z.-J. Strategies for combating bacterial biofilm infections. *Int. J. Oral Sci.* **7,** 1–7 (2015).

277. Wilson, K.-A. *et al.* Structure of microcin J25, a peptide inhibitor of bacterial RNA polymerase, is a lassoed tail. *J. Am. Chem. Soc.* **125,** 12475–12483 (2003).

278. Severinov, K. & Nair, S. K. Microcin C: biosynthesis and mechanisms of bacterial resistance. *Future Microbiol.* **7,** 281–289 (2012).

279. Joshi-Navare, K. & Prabhune, A. A Biosurfactant-Sophorolipid Acts in Synergy with Antibiotics to Enhance Their Efficiency. *BioMed Res. Int.* **2013,** e512495 (2013).

280. Haddad, N. I. A., Wang, J. & Mu, B. Identification of a biosurfactant producing strain: Bacillus subtilis HOB2. *Protein Pept. Lett.* **16,** 7–13 (2009).

281. San Keskin, N. O. *et al.* Production and structural characterization of biosurfactant produced by newly isolated staphylococcus xylosus STF1 from petroleum contaminated soil. *J. Pet. Sci. Eng.* **133,** 689–694 (2015).

282. Eddouaouda, K. *et al.* Characterization of a novel biosurfactant produced by Staphylococcus sp. strain 1E with potential application on hydrocarbon bioremediation. *J. Basic Microbiol.* **52,** 408–418 (2012).

283. Wang, Z.-J. *et al.* Metabolic flux analysis of the central carbon metabolism of the industrial vitamin B12 producing strain Pseudomonas denitrificans using 13C-labeled glucose. *J. Taiwan Inst. Chem. Eng.* **43,** 181–187 (2012).

284. Zamboni, N., Fendt, S.-M., Rühl, M. & Sauer, U. 13C-based metabolic flux analysis. *Nat. Protoc.* **4,** 878–892 (2009).

285. Eaves-Pyles, T. *et al.* Escherichia coli isolated from a Crohn's disease patient adheres, invades, and induces inflammatory responses in polarized intestinal epithelial cells. *Int. J. Med. Microbiol. IJMM* **298,** 397–409 (2008).

286. Stojiljkovic, I., Bäumler, A. J. & Heffron, F. Ethanolamine utilization in Salmonella typhimurium: nucleotide sequence, protein expression, and mutational analysis of the cchA cchB eutE eutJ eutG eutH gene cluster. *J. Bacteriol.* **177,** 1357–1366 (1995).

287. Casadaban, M. J. Transposition and fusion of the lac genes to selected promoters in Escherichia coli using bacteriophage lambda and Mu. *J. Mol. Biol.* **104,** 541–555 (1976).

288. Hegreness, M., Shoresh, N., Hartl, D. & Kishony, R. An Equivalence Principle for the Incorporation of Favorable Mutations in Asexual Populations. *Science* **311,** 1615–1617 (2006).

289. Guyer, M. S., Reed, R. R., Steitz, J. A. & Low, K. B. Identification of a sex-factor-affinity site in E. coli as gamma delta. *Cold Spring Harb. Symp. Quant. Biol.* **45 Pt 1,** 135–140 (1981).

290. Bachmann, B. J. Pedigrees of some mutant strains of Escherichia coli K-12. *Bacteriol. Rev.* **36,** 525–557 (1972).

291. Welch, R. A. *et al.* Extensive mosaic structure revealed by the complete genome sequence of uropathogenic Escherichia coli. *Proc. Natl. Acad. Sci. U. S. A.* **99,** 17020–17024 (2002).

292. Rahme, L. G. *et al.* Common virulence factors for bacterial pathogenicity in plants and animals. *Science* **268,** 1899–1902 (1995).

293. Dietrich, L. E. P., Price-Whelan, A., Petersen, A., Whiteley, M. & Newman, D. K. The phenazine pyocyanin is a terminal signalling factor in the quorum sensing network of Pseudomonas aeruginosa. *Mol. Microbiol.* **61,** 1308–1321 (2006).

294. Dietrich, L. E. P., Teal, T. K., Price-Whelan, A. & Newman, D. K. Redox-active antibiotics control gene expression and community behavior in divergent bacteria. *Science* **321,** 1203–1206 (2008).

295. Branda, S. S., González-Pastor, J. E., Ben-Yehuda, S., Losick, R. & Kolter, R. Fruiting body formation by Bacillus subtilis. *Proc. Natl. Acad. Sci. U. S. A.* **98,** 11621–11626 (2001).

Appendix A.

A.1 Bacterial strains used in this study

Designation	Genotype	Source of reference
EcN	*Escherichia coli* Nissle 1917, wild-type	Ardeypharm, Germany
MSC30	EcN Δ*mchDEF*::kan (KanR)	[99]
MSC66	EcN Δ*mchB*::scar Δ*mcmA*::kan (KanR)	[99]
MSC147	EcN Δ*entC*::kan (KanR)	This Study
MSC148	EcN Δ*iroBC*::kan (KanR)	This Study
AIEC	Adherent invasive *E. coli* isolate (NRG857c, O83:H1) $Carb^R$ Cm^R	[285]
IR715	*Salmonella enterica* servovar Typhimurium ATCC 14028, Nal^R	[286]
MSC168	IR715 pWKS30::*mchDEFmcmI* (Ap^R)	[99]
MSC170	IR715 pWKS30::*mchDEFmchI* (Ap^R)	[99]
MC4100	*E. coli* K-12, F^- *araD139*Δ(*argF-lac*)*U169 rspL150 relA1 flbB5301 fruA25 deoC1 ptsF25*	[287]
E. coli yfp	*E. coli* K12; MC4100, *galK::Plac-YFP, (ampR)Δlac*	[288]
MG1655	*E. coli* K12 $F^- \lambda^-$ *ilvG*$^-$ *rfb-50 rph-1*	[289]
BW25113	*E. coli* K-12, rrnB3ΔlacZ4787hsdR514Δ(araBAD)567ΔrhaBAD)568rph-1	[174]
W3110	*E. coli* K-12, $F^- \lambda^-$ rph-1 INV(rrnD, rrnE)	[290]
ZK2686	*E. coli* K12; W3110 D(argF-lac)U169	[3]
CFT073	Uropathogenic strain of *E. coli*; CFT073 PDG-4 (Amp R)	[291]
MC4100	*E. coli* K12: MC4100; *waaR::kan*	Thomas Silhavy Lab

Δ*waaR*		
MC4100 Δ*waaG*	*E. coli* K12: MC4100; *waaG::kan*	Thomas Silhavy Lab
PA14 WT	*Pseudomonas aeruginosa* wild type	[292]
Δ*lasI*	*P. aeruginosa* PA14 Δ*lasI*	George O'Toole Lab
Δ*rhlI*	*P. aeruginosa* PA14 Δ*rhlI*	George O'Toole Lab
Δ*lasI*Δ*rhlI*	*P. aeruginosa* PA14 Δ*lasI*Δ*rhlI*	George O'Toole Lab
Δ*rhlA*	*P. aeruginosa* PA14 Δ*rhlA*::gm	George O'Toole Lab
Δ*pqsA*	*P. aeruginosa* PA14 Δ*pqsA*	George O'Toole Lab
Δ*pqsH*	*P. aeruginosa* PA14 Δ*pqsH*	George O'Toole Lab
Δ*phz*1/2	*P. aeruginosa* PA14 with deletions of operons *phzA1-G1* and *phzA2-G2;*	[293]
2x*phz*	*P. aeruginosa* strain that has an extra copy of *phzM*,	[294]
E. coli ΔtnaA	MC4100 background Δ*tnaA* ::kan	this study
B. subtillis	*Bacilus subtillis* wild type isolate	[295]
S. epidermidis	*Staphylococcus epidermidis*	ATCC 14990

A.2. Plasmids used in this study

Designation	Genotype	Reference or Source
pJK611	Ap^R, temperature-sensitive, Lambda Red recombinase system	Kelly T. Hughes
pKD4	Ap^R, Kan^R	[174]
pGFPuv	Ap^R	Clonetech
pFPV-mCherry	Ap^R m-Cherry pFPU -Cherry	Addgene (plasmid #20956)

A.3. Primers used in generation of mutants this study

Designation	Purpose	Sequence
H1P1 *entC*	Flanking region 1 deletion of *entC*	5'_ATGGATACGTCACTGGCTGAGGAAGTACAGC AGACCATGGGTGTAGGCTGGAGCTGCTTC _3'
H2P2 *entC*	Flanking region 2 deletion of *entC*	5'_TAATGCAATCCAAAAACGTTCAACATGGTAG AAAGTTTGACATATGAATATCCTCCTTA_3'
Check *entC*	Check for *entC* deletion (K1)	5'_ GGGTACTGTATCCGGCGC_3'
Check *entC*	Check for *entC* deletion (K2)	5'_TGGATTTCCTTCGGCATCGG_3′
H1P1 *iroBC*	Flanking region 1 deletion of *iroBC*	5'_ACTATCCCGGGGTTTCCTCCTTCATGTTGTG CTGGCGATGGTGTAGGCTGGAGCTGCTTC_3'
H2P2 *iroBC*	Flanking region 2 deletion of *iroBC*	5'_TGCGTATTTTGTTTGTAGGCCCGCCTCTCTA TGGGCTGTTCATATGAATATCCTCCTTA _3'
Check *iroBC*	Check for *iroBC* deletion (K1)	5'_GTTCTTTCTGGCGTCCACCA_3'
Check *iroBC*	Check for *iroBC* deletion (K2)	5'_TGAATACCTGACGCTGCCAA_3'
K1_#2	pKD4 Kanamycin cassette for PCR confirmation	5'_ CAGTCATAGCCGAATAGCCT_3'
K2	pKD4 Kanamycin cassette for PCR confirmation	5'_CGGTGCCCTGAATGAACTGC_3'